

INFORMATION TO USERS

This manuscript has been reproduced from the microfilm master. UMI films the text directly from the original or copy submitted. Thus, some thesis and dissertation copies are in typewriter face, while others may be from any type of computer printer.

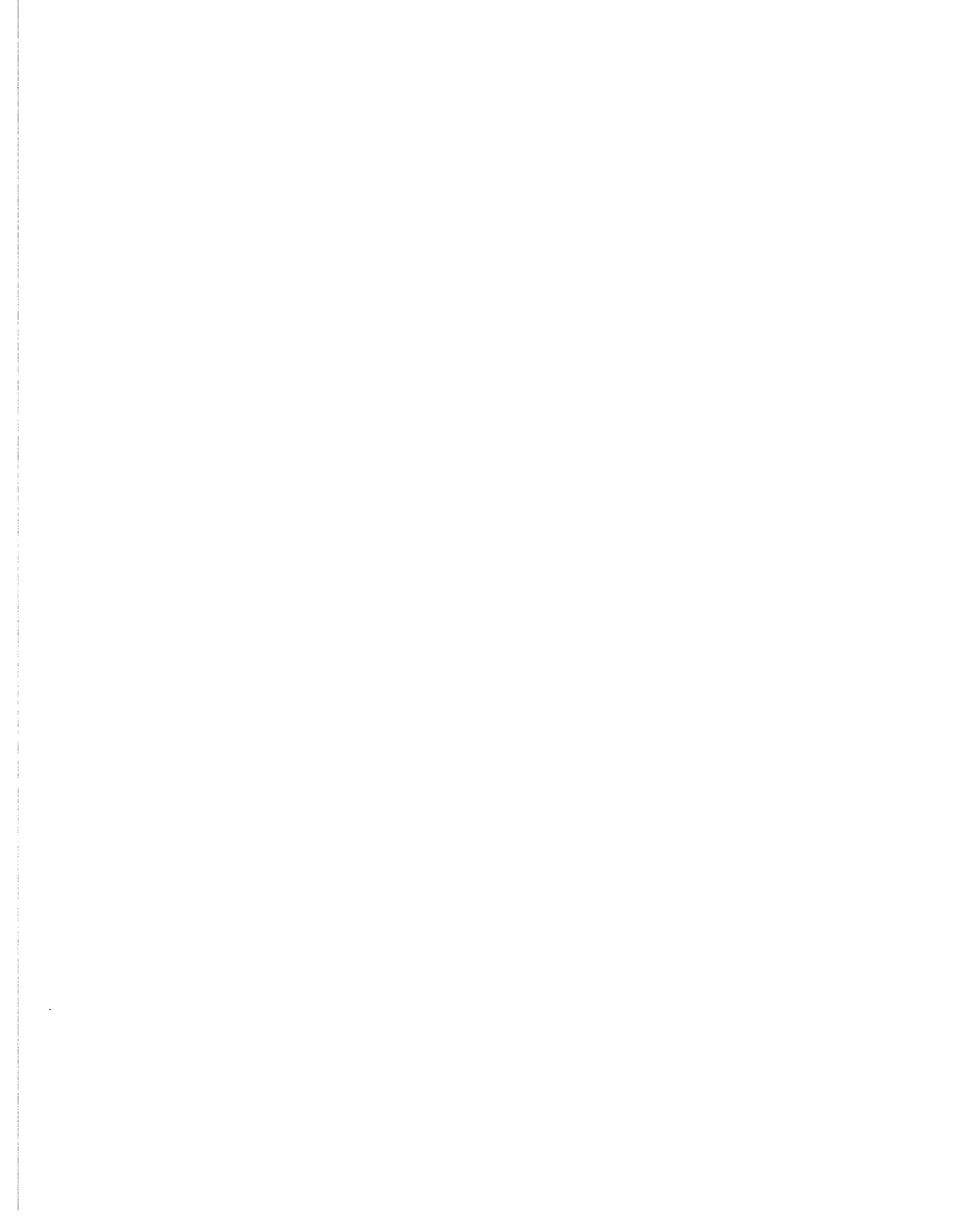
The quality of this reproduction is dependent upon the quality of the copy submitted. Broken or indistinct print, colored or poor quality illustrations and photographs, print bleedthrough, substandard margins, and improper alignment can adversely affect reproduction.

In the unlikely event that the author did not send UMI a complete manuscript and there are missing pages, these will be noted. Also, if unauthorized copyright material had to be removed, a note will indicate the deletion.

Oversize materials (e.g., maps, drawings, charts) are reproduced by sectioning the original, beginning at the upper left-hand corner and continuing from left to right in equal sections with small overlaps.

ProQuest Information and Learning
300 North Zeeb Road, Ann Arbor, MI 48106-1346 USA
800-521-0600

UMI[®]





**DEACTIVATION OF DEHYDRATION
ADSORBENTS**

BY

Ifadat Ali Khan

A Dissertation Presented to the
DEANSHIP OF GRADUATE STUDIES

KING FAHD UNIVERSITY OF PETROLEUM & MINERALS

DHAHRAN, SAUDI ARABIA

In Partial Fulfillment of the
Requirements for the Degree of

DOCTOR OF PHILOSOPHY

In

CHEMICAL ENGINEERING

December, 2002

UMI Number: 3081000

UMI[®]

UMI Microform 3081000

Copyright 2003 by ProQuest Information and Learning Company.
All rights reserved. This microform edition is protected against
unauthorized copying under Title 17, United States Code.

ProQuest Information and Learning Company
300 North Zeeb Road
P.O. Box 1346
Ann Arbor, MI 48106-1346

King Fahd University of Petroleum & Minerals
DHAHRAN 31261, SAUDI ARABIA

DEANSHIP OF GRADUATE STUDIES

This dissertation, written by Ifadat Ali Khan under the direction of his dissertation advisor and approved by his dissertation committee, has been presented to and accepted by the Dean of Graduate Studies, in partial fulfillment of the requirements for the degree of DOCTOR OF PHILOSOPHY IN CHEMICAL ENGINEERING.

Dissertation Committee



Dr. Kevin F. Loughlin
(Dissertation Advisor)



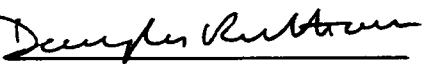
Dr. Habib Al-Ali (Member)



Dr. Ibrahim M. Abu-Reesh
(Member)



Prof. M. I. M. Wazeer
(Member)



Prof. D. M. Ruthven Nov 18/02
(External Examiner)



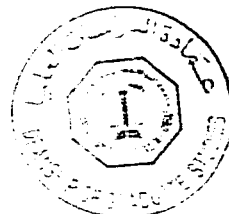
Prof. Mohammed B. Amin
(Department Chairman)



Prof. Osama Ahmed Jannadi
(Dean of Graduate Studies)

19/12/2002

Date



DEDICATION

*This work is dedicated to my father,
to the loving memory of my mother.
Rafīa and Jasim.*

ACKNOWLEDGMENT

In the name of Allah, the Most Beneficent, the Most Merciful.

“Read, In the name of thy Lord and Cherisher, Who Created. Created man from a [Leech-like] clot. Read, and thy Lord is most Bountiful, He who taught [the use of] pen. Taught man which he knew not. Nay, but man doth transgress all bounds. In that he looketh upon himself as self-sufficient. Verily, to thy Lord is the return [of all].” (The Holy Quran. Chapter # 196, Verses 1-5)

All praises are due to Allah, subhaanahu wa ta'aala, for his blessings on me and members of my family. I feel privileged to glorify his name in the sincerest way through this small accomplishment. I seek his mercy, favor, and forgiveness. I ask him to accept this little effort as an act of worship. May the peace and blessings of Allah be upon his prophet, Muhammad (Salla Allahu 'Alaehi was-sallam).

The support provided by King Fahd University of Petroleum & Minerals (KFUPM) is gratefully acknowledged.

With deep sense of gratitude and appreciation, I would like to express my sincere thanks to my dissertation advisor, Dr. K. F. Loughlin for his inspiring guidance, help and cooperation in supervising this research work. His single minded dedication to his work has been a source of motivation for me.

I would like to offer my sincere thanks to my learned thesis committee, Dr. Habib Al-Ali, Dr. Ibrahim Abu-Reesh, Prof. M. I. M. Wazeer, and Prof. D. M. Ruthven for their review and comments.

I would also like to thank the laboratory staff and technicians especially Mr. Romeo, Mr. Mahdi, Mr. Ibrahim, Mr. Bashir, and Mr. Kamal for their help during the experimental work. Thanks are also due to Mr. Riasat Khan for giving valuable comments on the formatting of this document.

I would also like to thank Saudi Aramco company for their assistance in performing the porosimetry studies on my two adsorbents.

Special thanks are due to my friends Sohail, Mazhar, Saif, Rizwan, and Faiz who are brothers to me. I am also thankful to all the inhabitants of Graduate PC lab whose cooperation during the theoretical part of this work is highly appreciated. Thanks are also due to Nabeel and Adam Giri who translated the abstract in Arabic.

I am thankful to chairman of chemical engineering department, Dr. Mohammed B. Amin, for his help and cooperation. I am also thankful to all faculty and Staff members for their kind and cheerful cooperation.

Finally and humbly, I offer my sincere thanks to my father, my mother who is sorely missed, Rafia, Jasim and other family members for their encouragement, cooperation, support, and prayers during this work.

(Ifadat Ali Khan)

CONTENTS

CONTENTS	iv
LIST OF TABLES	vi
LIST OF FIGURES	vii
ABSTRACT	xi
ABSTRACT (Arabic)	xiii
1 Introduction, Objectives & Literature Review	1
1.1 Structure of Zeolites	1
1.2 Pelletization of 4A Zeolites	3
1.3 Objectives of the Study	5
1.4 Literature Review	5
1.5 Kinetic Models for Adsorption Columns	7
1.5.1 <i>Isothermal Kinetic Models</i>	7
1.5.2 <i>Nonisothermal Kinetic Models</i>	9
1.5.3 <i>Zero Length Column Technique</i>	13
1.6 Deactivation of Zeolite Adsorbents.....	14
1.7 Layout of Dissertation	17
2 Kinetics of Sorption in Deactivated Zeolite Crystal Adsorbents	18
2.1 Theoretical Model for a Crystalline Particle	19
2.1.1 <i>Proof of Integral Boundary Condition</i>	20
2.2 Numerical technique	24
2.3 Results and Discussion.....	28
2.4 Conclusions	34
3 Modeling of Breakthrough Curves for Dual Site Isotherms of 4A Molecular Sieve Pellets at Intermediate Temperatures	35
3.1 Mathematical Model	37
3.2 Experimental Apparatus	42
3.3 Experimental Procedure	44
3.3.1 <i>Equilibrium Sorption Studies</i>	45
3.3.2 <i>Breakthrough Curve Measurement</i>	48
3.4 Results and Discussion.....	49
3.4.1 <i>Equilibrium Sorption Studies</i>	49
3.4.2 <i>Breakthrough Curve Measurement</i>	52
3.4.2.1 <i>Pore Size Distribution</i>	55

3.4.2.2	<i>Particle Size Distribution</i>	55
3.4.2.3	<i>Parameter Estimation</i>	55
3.4.2.4	<i>Effect of Dead Volume</i>	58
3.5	Conclusions	62
4	Deactivation Modeling of 4A Zeolite Adsorbents.....	64
4.1	NMR for Deactivation Studies.....	65
4.2	Nuclear Microscopy for Dealumination Studies.....	66
4.3	Experimental Apparatus.....	68
4.4	Experimental Procedure	69
4.5	Results and Discussion.....	71
4.5.1	<i>Deactivation Mechanism</i>	85
4.6	Conclusions	96
5	Conclusions and Recommendations	98
5.1	Conclusions	98
5.2	Recommendations	99
APPENDIX A	Numerical Calculation of Breakthrough Curves.....	101
APPENDIX B	List of Files on CD	106
LIST OF SYMBOLS		107
REFERENCES		112
VITA		120

LIST OF TABLES

TABLE 1-1	Some commonly used adsorbents and their properties.....	2
TABLE 1-2	Properties of 4A zeolite crystals.	4
TABLE 1-3	Summary of analytic solutions for breakthrough curve for linear. isothermal trace component systems	8
TABLE 1-4	Summary of solutions for breakthrough curve for systems with irreversible isotherm	9
TABLE 1-5	Summary of numerical solutions for adiabatic adsorption columns with finite mass transfer resistance.	11
TABLE 1-6	Experimental data used by various authors for modeling adiabatic adsorption columns.	11
TABLE 2-1	Values of parameters used in Eq. (2-25). obtained by fitting the equation to the numerical values.....	30
TABLE 3-1	Details of adsorption column.....	44
TABLE 3-2	Isotherm parameters obtained by fitting experimental data for Uetikon pellets to the theoretical isotherm equation.....	52
TABLE 3-3	Intrusion data obtained by mercury porosimetry.....	55
TABLE 3-4	Values of fitting parameters for the fresh 4A zeolite pellets.	59
TABLE 3-5	Values of parameters used to calculate theoretical breakthrough curves.	59
TABLE 4-1	Six letter coding system for the experimental breakthrough curves.....	70
TABLE 4-2	Values of fitting parameters obtained by fitting the experimental adsorption curves to theoretical ones.....	75
TABLE 4-3	Deactivation time constant and ratio of limiting pore mouth mass transfer coefficient obtained by fitting the experimental data to model equation.....	88
TABLE 4-4	Values of fitting parameters for limiting pore mouth mass transfer coefficient.	94
TABLE 4-5	Values of fitting parameters for deactivation time.	94
TABLE B-1	List of all the files on the cd.....	106

LIST OF FIGURES

FIGURE 1-1	Schematic representation of the structure of zeolite A ¹ . The unit cell has cubic symmetry with unit cell size of 12.3 Å. Each unit cell has two cages (α and β) where adsorption can take place. β cage is small in size. Only small and highly polar molecules like water can access β cage in sodium form of zeolite A.	3
FIGURE 2-1	Illustration of the distribution of blocked area on the surface. Solid line corresponds to the blocked region and the dashed line corresponds to the exposed region.	23
FIGURE 2-2	A symmetric sector of angle $1/2n_p$. Dashed line corresponds to the exposed region and solid line corresponds to the blocked region. The area of exposed region is $(1-A_b)/2n_p$ and that of the blocked region is $A_b/2n_p$. The θ -fluxes at the two boundaries are zero due to symmetry.	24
FIGURE 2-3	Adsorbed phase concentration profiles in the crystal at $t^* = 0.10$. Profiles have been obtained for various values of A_b as specified in the figures, $n_p = 1$, $ \lambda_s - \lambda_i = 0$, and during adsorption. Only half of the cylindrical cross section has been shown due to symmetry. $A_b = 0.0$ for (a), $A_b = 0.30$ for (b), $A_b = 0.60$ for (c), $A_b = 0.90$ for (d).....	29
FIGURE 2-4	Uptake curves for various values of A_b as specified in the figure. All the curves are obtained for a linear isotherm i.e. $ \lambda_s - \lambda_i \rightarrow 0$ and for $n_p = 1$	32
FIGURE 2-5	Effect of varying n_p on the uptake curves. Uptake curves have been obtained for a linear isotherm with $A_b = 0.99$	32
FIGURE 2-6	Ratio of time required for 99 % adsorption at a given A_b to that at $A_b = 0$. Curves are obtained for various values of n_p as shown in the figure. Symbols correspond to the actual values obtained from numerical solution and the solid lines correspond to the data fitted to a function of A_b	32
FIGURE 2-7	Adsorption and desorption rate curves for nonlinear isotherms. The curves have been obtained for $A_b = 0.5$ and $n_p = 1$. Solid lines correspond to adsorption and dashed lines to desorption rate curves. $\lambda = \lambda_s - \lambda_i $	32

FIGURE 3-1	Schematic diagram of the constant volume apparatus used for generating isotherm data.....	43
FIGURE 3-2	Schematic diagram of the experimental setup for the determination of the breakthrough curve.....	45
FIGURE 3-3	Experimental (symbols) and fitted (smooth lines) isotherms at 175 °C (●) and 200 °C (▲). Dashed lines are predictions in 95 % confidence interval for the corresponding theoretical isotherm. Open circles correspond to the experimental isotherm points for TOSOH pellets at 175 °C.....	50
FIGURE 3-4	Experimental (symbols) and fitted (smooth lines) isotherms at 175 °C (●) and 200 °C (▲) on log-log scale. Dashed lines are predictions in 95 % confidence interval for the corresponding theoretical isotherm. Open circles correspond to the experimental isotherm points for TOSOH pellets at 175 °C.	51
FIGURE 3-5	Adsorption and desorption breakthrough curves for Uetikon pellets at 175 °C and 200 °C. Symbols correspond to the experimental adsorption data at 175 °C (Δ), 200 °C (∇) and desorption data at 175 °C (○), and 200 °C (□). Solid and dashed lines correspond to the fitted adsorption and predicted desorption breakthrough curves respectively.	53
FIGURE 3-6	Adsorption and desorption breakthrough curves for TOSOH pellets at 175 °C and 200 °C. Symbols correspond to the experimental adsorption data at 175 °C (Δ), 200 °C (∇) and desorption data at 175 °C (○), and 200 °C (□). Solid and dashed lines correspond to the fitted adsorption and predicted desorption breakthrough curves respectively.	53
FIGURE 3-7	Cumulative pore size distribution of TOSOH (solid line) and Uetikon (dashed line) pellets.	54
FIGURE 3-8	Particle size distribution of TOSOH (solid line) and Uetikon (dashed line) pellets. f is the number fraction of particles and d_p is the pellet diameter. Dotted line corresponds to particle size distribution of a sample of TOSOH pellets as supplied by the manufacturer. Solid and dashed lines are obtained after sieving the original TOSOH and Uetikon samples.	56
FIGURE 3-9	Graphical procedure for the estimation of p_w . Material balance line is given by Eq. 3-28. Dashed lines correspond to 95 % confidence interval for equilibrium isotherm predictions.	59
FIGURE 4-1	Schematic diagram of the apparatus used for deactivating the zeolite samples.....	69

FIGURE 4-2	Experimental (symbols) and fitted adsorption (solid line) and desorption (dashed line) breakthrough curves for HHUFL (○), HHU1L (□), HHU2L (△), and HHU3L (▽).....	76
FIGURE 4-3	Experimental (symbols) and fitted adsorption (solid line) and desorption (dashed line) breakthrough curves for HHUFH (○), HHU1H (□), HHU2H (△), and HHU3H (▽).....	76
FIGURE 4-4	Experimental (symbols) and fitted adsorption (solid line) and desorption (dashed line) breakthrough curves for HLUFL (○), HLU1L (□), HLU2L (△), and HLU3L (▽).....	77
FIGURE 4-5	Experimental (symbols) and fitted adsorption (solid line) and desorption (dashed line) breakthrough curves for HLUFH (○), HLU1H (□), HLU2H (△), and HLU3H (▽).....	77
FIGURE 4-6	Experimental (symbols) and fitted adsorption (solid line) and desorption (dashed line) breakthrough curves for LHUFL (○), LHU1L (□), LHU2L (△), and LHU3L (▽).....	78
FIGURE 4-7	Experimental (symbols) and fitted adsorption (solid line) and desorption (dashed line) breakthrough curves for LHUFH (○), LHU1H (□), LHU2H (△), and LHU3H (▽).....	78
FIGURE 4-8	Experimental (symbols) and fitted adsorption (solid line) and desorption (dashed line) breakthrough curves for LLUFL (○), LLU1L (□), LLU2L (△), and LLU3L (▽).....	79
FIGURE 4-9	Experimental (symbols) and fitted adsorption (solid line) and desorption (dashed line) breakthrough curves for LLUFH (○), LLU1H (□), LLU2H (△), and LLU3H (▽).....	79
FIGURE 4-10	Experimental (symbols) and fitted adsorption (solid line) and desorption (dashed line) breakthrough curves for HHTFL (○), HHT1L (□), HHT2L (△), and HHT3L (▽).....	80
FIGURE 4-11	Experimental (symbols) and fitted adsorption (solid line) and desorption (dashed line) breakthrough curves for HHTFH (○), HHT1H (□), HHT2H (△), and HHT3H (▽).....	80
FIGURE 4-12	Experimental (symbols) and fitted adsorption (solid line) and desorption (dashed line) breakthrough curves for HLTFL (○), HLT1L (□), HLT2L (△), and HLT3L (▽).....	81
FIGURE 4-13	Experimental (symbols) and fitted adsorption (solid line) and desorption (dashed line) breakthrough curves for HLTFH (○), HLT1H (□), HLT2H (△), and HLT3H (▽).....	81
FIGURE 4-14	Experimental (symbols) and fitted adsorption (solid line) and	

	desorption (dashed line) breakthrough curves for LHTFL (○), LHT1L (□), LHT2L (△), and LHT3L (▽).....	82
FIGURE 4-15	Experimental (symbols) and fitted adsorption (solid line) and desorption (dashed line) breakthrough curves for LHTFH (○), LHT1H (□), LHT2H (△), and LHT3H (▽).	82
FIGURE 4-16	Experimental (symbols) and fitted adsorption (solid line) and desorption (dashed line) breakthrough curves for LLTFL (○), LLT1L (□), LLT2L (△), and LLT3L (▽).....	83
FIGURE 4-17	Experimental (symbols) and fitted adsorption (solid line) and desorption (dashed line) breakthrough curves for LLTFH (○), LLT1H (□), LLT2H (△), and LLT3H (▽).....	83
FIGURE 4-18	Ratio of pore mouth mass transfer coefficients for Uetikon pellets obtained at 175 °C and plotted as a function of deactivation time. Deactivation conditions: HH (○), LH (●), HL (□), LL (■). Smooth lines are fitted deactivation curves.....	89
FIGURE 4-19	Ratio of pore mouth mass transfer coefficients for Uetikon pellets obtained at 200 °C and plotted as a function of deactivation time. Deactivation conditions: HH (○), LH (●), HL (□), LL (■). Smooth lines are fitted deactivation curves.....	89
FIGURE 4-20	Ratio of pore mouth mass transfer coefficients for TOSOH pellets obtained at 175 °C and plotted as a function of deactivation time. Deactivation conditions: HH (○), LH (●), HL (□), LL (■). Smooth lines are fitted deactivation curves.....	89
FIGURE 4-21	Ratio of pore mouth mass transfer coefficients for TOSOH pellets obtained at 200 °C and plotted as a function of deactivation time. Deactivation conditions: HH (○), LH (●), HL (□), LL (■). Smooth lines are fitted deactivation curves.....	89
FIGURE 4-22	Effect of deactivation on activation energy for jump across pore mouths of Uetikon pellets. Deactivation conditions: HH (○), LH (●), HL (□), LL (■). Solid line is the average activation energy.	92
FIGURE 4-23	Effect of deactivation on activation energy for jump across pore mouths of TOSOH pellets. Deactivation conditions: HH (○), LH (●), HL (□), LL (■). Solid line is the average activation energy.	92

ABSTRACT

Name: IFADAT ALI KHAN
Title: DEACTIVATION OF DEHYDRATION ADSORBENTS
Degree: DOCTOR OF PHILOSOPHY
Major Field: CHEMICAL ENGINEERING
Date of Degree: December 2002

The deactivation of 4A zeolite molecular sieves under severe hydrothermal conditions is studied. Accelerated deactivation runs are performed on Uetikon and TOSOH 4A zeolite pellets, and the results are interpreted considering their equilibrium and kinetic data.

A mathematical model for predicting the uptake rates for crystal particles partially blocked either due to coking or pore mouth closure is developed and numerical results obtained. Concentrated blockage of the crystal surface greatly reduces the mass transfer rate in comparison to uniformly distributed surface blockage.

Equilibrium data for fresh water on 4A zeolite pellets is obtained at 175 °C and 200 °C, and fitted to a dual site Freundlich-Langmuir isotherm. The theoretical breakthrough curves are calculated using a dispersed plug flow model with mass transfer controlled by macropore and pore mouth resistances. The experimental breakthrough curves show a high degree of asymmetry between adsorption and desorption even at low equilibrium loading (less than 15 % of saturation loading). This asymmetry can be satisfactorily accounted for by the dual site Freundlich-Langmuir isotherm.

Accelerated deactivated 4A zeolite samples are prepared at two temperatures, 350 °C and 400 °C, and two water vapor loadings, 0.05 gm/gm and 0.16 gm/gm for time periods of 100, 200, and 300 hrs. Breakthrough curves are obtained at 175 °C and 200 °C, at approximately 9.3 mbar inlet water vapor pressure, and the pore mouth time constant is obtained by fitting the experimental breakthrough curves to the theoretical ones. The pore

mouth time constant increases with duration of deactivation, approaching a constant value as deactivation increases. The degree of deactivation is highest for the most severe and lowest for the least severe hydrothermal conditions. Uetikon pellets exhibit less deactivation than the TOSOH pellets.

A simple reversible deactivation mechanism is proposed. The rate of change of mass transfer coefficient across the pore mouth to deactivation temperature and moisture loading is derived and fitted to the experimental data. The activation energy of jump across the pore mouth is invariant with deactivation; however, the pre-exponential factor decreases indicating an increase in entropy due to a loss of crystallinity at the pore mouth.

Doctor of Philosophy Degree

King Fahd University of Petroleum & Minerals

Dhahran, Saudi Arabia

December 2002

ملخص بحث

درجة الدكتوراة في الفلسفة

الاسم :	أفادت علي خان
عنوان الرسالة :	الخمول الكيميائي للمواص الجافة
التخصص :	الهندسة الكيميائية
تاريخ للتخرج :	ديسمبر ٢٠٠٢ م

هذه الرسالة ناقشت الخمول الكيميائي للزيوليت من النوع (4A) تحت تأثير درجات الحرارة العالية. اعتمدت تجارب هذه الدراسة على استخدام حبات الزيوليت (4A) للمصنعة في شركتي يتكن و توسو ، وقد تم تفسير النتائج بالإعتماد على توازن تلك الحبيبات وديناميكيته.

خلال هذه الدراسة تم الحصول على صيغة رياضية لمعرفة معدل الامتصاص لبلورات هذه الحبيبات التي تم سد مسامها كنتيجة لعمليات التتحم وإيجاد الحل الرياضي لهذه الصيغة الرياضية وتنتج أخرى عديدة. عند مقارنة سطوح البلورات التي تم سد مسامها بشكل مكثف بتلك التي تم سد مسامها بشكل منظم وموزع وجدنا أن معدل انتقال المادة يكون أقل في السطوح الأولى مقارنة بالثانية.

من النتائج التي تم الحصول عليها أيضاً علاقة توازن الماء العذب في حبيبات الزيوليت (4A) عند درجات الحرارة 175°C و 200°C حيث تم مطابقتها بمعادلة فرنديش- لانغيمير ثنائية المواقع . وقد تم حساب نقاط الاختراق للمنحنيات النظرية باستخدام (dispersed plug flow model) وذلك عندما يكون معدل انتقال المادة هو المتحكم في العملية ككل . أما بالنسبة لنقاط الاختراق العملية (التجريبية) فقد أظهرت درجة عالية من عدم التناسق والتطابق بين الامتزاز والانفكاك حتى عند انخفاض كمية التوازن (أقل من ١٥%) ، وتعتبر هذه الدرجة من اللاتناسق كافية لدعم إمكانية استخدام معادلة فرنديش- لانغيمير ثنائية المواقع .

تم تحضير عمليات الزيوليت (4A) عند درجات حرارة 350°C و 400°C ، بينما كانت كمية البخار ٠,٠٥ ملجم/ملجم، ٠,١٦ ملجم/ملجم لفترة ٢٠٠، ١٠٠، ٢٠٠ ساعة . أما بالنسبة لنقاط الاختراق فقد تم الحصول عليها عند درجات الحرارة 175°C و 300°C وكان ضغط بخار الماء المُدخل تقريباً ٩,٣ مليبار، وتم الحصول على معامل الوقت لفتحة المسام من خلال مطابقة المنحنيات النظرية بالمنحنيات العملية. هذا المعامل يزيد بزيادة مدة الخمول الكيميائي إلى أن يصل إلى قيمة ثابتة لا تتغير بتغير مدة الخمول الكميائي ، وتكون درجة الخمول الكيميائي عالية عند درجات الحرارة العالية ومنخفضة عند درجات الحرارة المنخفضة. وتعتبر درجة الخمول الكيميائي في حبات الزيوليت المصنعة في شركة يتكن أقل من نظيرتها المنتجة من شركة توسو.

بالإضافة إلى ذلك فإنه قد تم إقتراح لميكانيكية الخمول الكيميائي، كما تم إيجاد معدل تغير معامل انتقال المادة خلال فتحة المسام بالنسبة لدرجة الحرارة وكمية الرطوبة وقورن بالنتائج العملية. طاقة التنشيط عند فتحة المسام لا تتغير بتغير الخمول الكيميائي بينما معامل الدالة الأسية يقل لزيادة درجة الأنظمة وهذا في حد ذاته إشارة لخسارة التنظيم للكرستالي عند فتحة المسام

درجة الدكتوراة في الفلسفة

جامعة الملك فهد للبترول و المعادن

الظهران، العربية السعودية

ديسمبر ٢٠٠٢ م

1

INTRODUCTION, OBJECTIVES & LITERATURE REVIEW

The ability of porous solids like alumina, silica gel, activated carbon and zeolites to adsorb large volumes of vapors and liquids was recognized as early as the eighteenth century. However, the commercial exploitation of the adsorptive property of porous materials started much later in nineteenth century. Perhaps, the most important application of an adsorbent is in an adsorption column, packed with a suitable hydrophilic adsorbent as a drier for the removal of moisture from either gas or liquid streams.

Some of the commonly used adsorbents and their properties are shown in Table 1-1. Alumina is suitable for drying warm gases as it has high capacity even at elevated temperatures. 4A zeolite has a high affinity for moisture even at low water vapor partial pressures. Therefore, 4A zeolite is suitable to remove *traces* of moisture from gas streams.

1.1 Structure of Zeolites

Zeolites are porous crystalline aluminosilicates. The basic building units of zeolite crystal lattice are SiO_4 and AlO_4 tetrahedra. SiO_4 and AlO_4 tetrahedra are three

TABLE 1-1 Some commonly used adsorbents and their properties.

Adsorbent	Nature	Remarks
Silica gel	Hydrophilic	Low capacity at elevated temperature
Alumina	Hydrophilic	High capacity at elevated temperature
4A zeolite	Hydrophilic	High affinity even at low partial pressure
Activated carbon	Hydrophobic	Cannot be used for drying

dimensional structures in which Si and Al atoms are at the center of a tetrahedron respectively, and O atoms are arranged at the four vertices of the tetrahedron^{1, 2}. In the zeolite crystal lattice or framework, the O atoms at the tetrahedron vertices are shared between two adjacent tetrahedra. The sharing of vertex O atoms gives rise to a virtually endless sequence of AlO_4 and SiO_4 tetrahedra covalently bonded together to form the zeolite crystal. The tetrahedra can be joined together in various ways leading to a wide variety of zeolite structures.

An aluminum atom with only three valence electrons cannot fully neutralize the four negative charges in its tetrahedron resulting from each of the four O atoms. Thus, in the aluminosilicate structure there is one net negative charge for each aluminum atom. These negative charges are balanced by the presence of the appropriate number of exchangeable monovalent or divalent cations held inside the crystal lattice by ionic bonds².

The aluminosilicate framework of a zeolite is a fairly open structure containing a regular arrangement of cavities joined by windows of a few Angstroms in diameter. The effect is a one, two or three-dimensional network of uniform interconnected pores of diameters comparable with the molecular dimensions. Small molecules, which can penetrate the pores, are adsorbed by the zeolite but larger molecules are excluded.

The A type zeolites are characterized by a framework of polyhedral cages of cubic symmetry as shown in Figure 1-1. 4A zeolite is the sodium form of an A type zeolite. The idealized structural formula of a unit cell of 4A zeolite is $\text{Na}_{12}[\text{Al}_{12}\text{Si}_{12}\text{O}_{48}]\cdot 27\text{H}_2\text{O}$ and the effective diameter of the pores is 4 Angstrom². Some common properties of 4A zeolite are listed in Table 1-2.

1.2 Pelletization of 4A Zeolites

Industrial applications of 4A zeolite require the zeolite crystals compacted in the form of pellets having high physical strength and attrition resistance. Methods for forming the crystalline powders into pellets include the addition of an inorganic binder, generally a

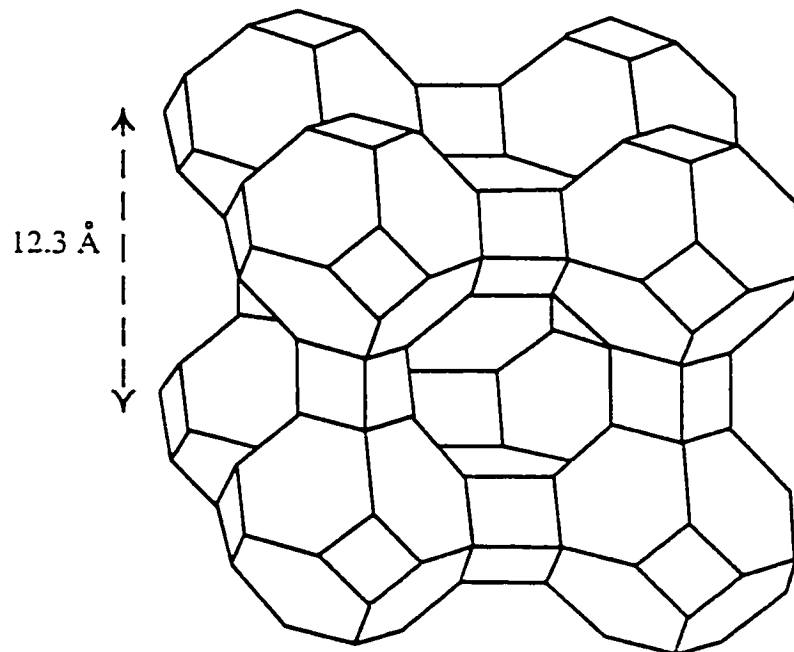


FIGURE 1-1 Schematic representation of the structure of zeolite A¹. The unit cell has cubic symmetry with unit cell size of 12.3 Å. Each unit cell has two cages (α and β) where adsorption can take place. β cage is small in size. Only small and highly polar molecules like water can access β cage in sodium form of zeolite A.

TABLE 1-2 Properties of 4A zeolite crystals.

Property	Value
Unit cell size	12.32 Å
Density (fully hydrated)	1.99 g/cc
H ₂ O molecules in one unit cell	27
Na ⁺ ions in one unit cell	12
Cages available for adsorption	2 (α and β)
α cage aperture	4 Å
β cage aperture	2.2 Å
α cage volume	775 Å ³
β cage volume	155 Å ³

clay, to the high purity zeolite powder. The blended clay zeolite mixture is extruded into cylindrical type pellets or formed into beads. These pellets are then calcined or activated in steam at around 650 °C in order to convert the clay to an amorphous binder of high mechanical strength. As binders, clays of the kaolin or metal powders are used. The typical binder content of a zeolite pellet is 20 wt%, however, it may vary from manufacturer to manufacturer. The pellets or beads from different manufacturers have different properties e.g. macropore diffusivity, micropore diffusivity, adsorption capacity, and pore mouth resistance etc. as a result of differences in severity of hydrothermal treatment during the pelletization process.

Application of 4A zeolite pellets for drying involves the use of a cyclic batch system in which the adsorbent bed is alternately saturated and regenerated in a cyclic manner. The most common examples of such systems are pressure swing adsorption and thermal swing adsorption. These systems differ in the methods by which the adsorbent is regenerated during the desorption cycle. In thermal swing operation the bed is

regenerated by heating, usually with a stream of hot gas, to a temperature at which the adsorbed species are desorbed and removed from the bed in the fluid stream. In a pressure swing process, the same task is achieved by reducing the pressure at essentially constant temperature.

Thermal swing adsorption is probably the most common system for drying of gases. Since, temperature is a more effective variable than pressure for changing the thermodynamic potential¹, thermal swing processes are generally preferred for strongly adsorbed species such as water on 4A or alumina. However, repeated thermal cycling in presence of moisture can lead to deactivation of the zeolite adsorbent due to dealumination and exposure to elevated temperature in presence of reactive hydrocarbons during the desorption cycle can lead to coke formation in the adsorbent.

1.3 Objectives of the Study

The main objective of this study is to identify the mechanism of deactivation of 4A zeolite adsorbent and develop a model to predict the extent of deactivation as a function of temperature, steam concentration and the time exposed to the steam. Deactivation runs and analysis of deactivated samples by studying the kinetics will be carried out on 4A zeolite samples obtained from two different manufacturers namely TOSOH and Uetikon.

1.4 Literature Review

The most widely used technique for studying the kinetics of mass transfer in molecular sieve adsorbent pellets is by following the transient adsorption or desorption curves. Such

experiments can be carried out either gravimetrically or volumetrically. As an alternative to these conventional methods, several column techniques have also been developed. Column techniques offer the advantage of speed; however, the analysis of data is somewhat more complex due to the presence of dispersion, which must be taken into account. In the present study column technique has been used to analyze the deactivated samples.

In this section we analyze the models available in literature for the breakthrough curves for adsorption columns, both under isothermal and nonisothermal conditions followed by the section on review of literature on deactivation of adsorbents. The available literature on some recent advances for studying the kinetics in zeolites is also discussed. The following two paragraphs discuss some basic terms, which are frequently used in our discussion of the literature.

In general, the breakthrough curve measurements are carried out by making an initial step change in concentration of the fluid stream flowing through a column packed with adsorbent pellets. If the magnitude of initial step change in concentration is small or differential then the equilibrium isotherm can be approximated by a straight line and we have a linear isotherm. However, if the magnitude of the step change is large then we must take into account the actual shape of equilibrium isotherm, which is nonlinear. An irreversible or rectangular isotherm is the extreme case of nonlinearity, which is an idealization for strongly adsorbed species. The Langmuir isotherm approaches the irreversible isotherm for a concentration step change such that the equilibrium adsorbed phase concentration approaches the monolayer saturation concentration.

1.5 Kinetic Models for Adsorption Columns

In this section, the kinetic models available for adsorption columns are reviewed. The discussion is restricted to trace systems, i.e., systems in which only traces of adsorbable component are present in an inert carrier. The available models can be classified on the basis of the type of flow, which can be either plug flow or axially dispersed flow. The models can be further classified on the basis of the kinetic model for a single pellet. In the following section we discuss the isothermal kinetic models for adsorption columns.

1.5.1 Isothermal Kinetic Models

For a linear equilibrium isotherm, analytic expressions can be obtained for the breakthrough curve. The references to various models that are available for such systems are tabulated in Table 1-3. Since, these models are for linear isotherm, the adsorption and desorption breakthrough curves are mirror images.

When the equilibrium relationship is nonlinear it is generally not possible to determine a general analytic solution for the breakthrough curve. Theoretical breakthrough curves for nonlinear systems may be calculated by numerical solution of the model equations using standard finite difference or collocation methods. Such solutions have been obtained by many authors. In most of these studies plug flow is assumed and the equilibrium isotherm is either Langmuir or Freundlich.

Antonson and Dranoff³ have solved the model for micropore diffusion control with the Langmuir isotherm. They have considered the micropore diffusivity to be constant.

TABLE 1-3 Summary of analytic solutions for breakthrough curve for linear, isothermal trace component systems

Flow Model	Kinetic Model for Pellet	Author
Plug flow	No resistance to mass transfer, pellets in equilibrium with the local bed concentration	DeVault ¹⁰
Plug flow	Linearized rate expression : $\frac{\partial \bar{q}}{\partial t} = k(q^* - q)$	Anzelius ¹¹ , Walter ^{12, 13} , Furnas ¹⁴ , Nusselt ¹⁵ , Klinkenberg ¹⁶
Dispersed plug flow	Linearized rate expression	Lapidus and Amundson ¹⁷ , Levenspiel and Bischoff ¹⁸
Plug flow	Macropore resistance controlling	Rosen ^{19, 20}
Dispersed plug flow	Macropore resistance controlling	Rasmuson and Neretnieks ²¹
Plug flow	Macropore and micropore with external film resistance	Kawazoe and Takeuchi ²²
Dispersed plug flow	Macropore and micropore with external film resistance	Rasmuson ²³

Kyte⁴ solved the same problem for Freundlich isotherm. Garg and Ruthven^{5, 6, 7} have considered the same problem but taken into account the variation of micropore diffusivity. The model for macropore diffusion control has been solved by Carter and Husain⁸ and by Garg and Ruthven⁹.

Numerical results for nonlinear isotherm models suggest that the adsorption and desorption curves are mirror images when the isotherm approaches the limit of linearity. However, the asymmetry between the two increases with increasing nonlinearity.

The earliest solution for the breakthrough curve for an irreversible system appears to be due to Bohart and Adams²⁴ who used a quasi-chemical rate expression. The cases of micropore diffusion control and macropore diffusion control were solved by Cooper²⁵ and by Cooper and Libermann²⁶. A summary of the models for breakthrough curves for

an irreversible system is given in Table 1-4. All solutions assume plug flow.

TABLE 1-4 Summary of solutions for breakthrough curve for systems with irreversible isotherm

Rate Equation	Author
Quasichemical	Bohart and Adams ²⁴
Linear rate and solid film	Cooper ²⁵
Linear rate and external film resistance	Ruthven ¹
Micropore diffusion	Cooper ²⁵
Macropore diffusion	Cooper and Libermann ²⁶
Macropore diffusion and external film resistance	Weber and Chakravorti ²⁷

1.5.2 Nonisothermal Kinetic Models

A general solution to the nonisothermal adsorption in an adsorption column requires the simultaneous solution of the appropriate mass transfer rate equation and the energy balance, subject to the appropriate boundary conditions and equilibrium relationship. Due to the complex nature of such a general nonisothermal problem, solutions have generally been restricted to the limiting cases of either isothermal operation for which the energy equation can be eliminated, or adiabatic operation for which the energy balance attains a simplified form. The discussion on isothermal kinetic models for adsorption columns has been presented in the previous section. The nonisothermal kinetic models for adsorption columns are discussed in the present section.

For sorption studies in a fixed bed under mass transfer equilibrium, the case of adiabatic sorption has been considered by Leavitt²⁸, Amundson et al.²⁹ and Pan and Basmadjian^{30, 31}. Pan and Basmadjian have also verified their model with an experimental study of the adsorption of CO₂ on 5A molecular sieve.

When mass transfer resistance is important the dynamic behavior of an adsorption column can generally be predicted only by numerical solution of the coupled differential heat and mass balance equations which describe the system. The earliest general numerical solutions for a nonisothermal adsorption column with a nonlinear adsorption isotherm appear to have been given by Carter^{32, 33, 34}, by Meyer and Weber³⁵ and by Lee and Weber³⁶. A summary of these and other similar studies is given in Table 1-5. The models developed in all of these studies have been tested by one or more experimental studies which are also listed in the Table. The data used for modeling the adiabatic adsorption columns is shown in Table 1-6.

These studies indicate that for the isothermal system with a linear isotherm the adsorption and desorption curves are mirror images. As the nonisothermality of the system increases a pronounced asymmetry develops between the adsorption and desorption breakthrough curves. It is seen that the effect of increasing nonisothermality on the shape of breakthrough curve is much more for the case of desorption than for adsorption.

For the case of an irreversible isotherm the differential mass balance and mass transfer rate equations become, to a first approximation, independent of temperature and therefore independent of heat balance. Under these conditions a formal analytic solution may be derived for temperature and concentration breakthrough curves. Such solutions have been obtained by Ozil and Bonnetain³⁷ and by Yoshida and Ruthven³⁸.

TABLE 1-5 Summary of numerical solutions for adiabatic adsorption columns with finite mass transfer resistance.

Author	Equilibrium Isotherm	Mass transfer Resistance	Heat transfer Resistance	Experimental System	Remarks
Carter ^{32, 34, 33}	Freundlich	External film + Macropore	External film	H ₂ O-Al ₂ O ₃ , Silica, 4A sieve	Finite difference
Weber ^{35, 36} and coworkers	Empirical, nonlinear	External film + Macropore	External film	CH ₄ -Act. Carbon	Wall heat loss included
Cooney ³⁹	Langmuir	Linear rate	External film	—	Finite difference
Ikeda ⁴⁰	Langmuir	Macropore	Thermal Equilibrium	CO ₂ -5A sieve	Finite difference
Marcussen ⁴¹	Freundlich	Macropore	External film + Internal conduction	H ₂ O-Alumina	Collocation
Raghavan, Duncan and Ruthven ⁴²	Langmuir	External film + Macropore	External film	H ₂ O-4A sieve	Axial dispersion included, Collocation

TABLE 1-6 Experimental data used by various authors for modeling adiabatic adsorption columns.

Author	Model Data
Carter ^{32, 34, 33}	$(-\Delta H) = 1250$ Btu/lb (water-alumina), experimentally determined values of KD/R_p^2 at various temperatures. KD independent of temperature for water-4A zeolite
Weber and coworkers ^{35, 36}	D_c independent of temperature. $(-\Delta H)$ related to the derivatives of empirical isotherm.
Cooney ³⁹	Hypothetical values of $(-\Delta H)$. Linear rate model with the overall resistance independent of temperature.
Raghavan and Ruthven ⁴²	$(-\Delta H)c_o/C_f T_o = 0.068$ for water-4A zeolite system.

1.5.3 Zero Length Column Technique

A comprehensive review of the measurement of diffusion in porous solids by ZLC methods is provided by Ruthven and Brandani⁴³ in a recent article. Principles of the ZLC technique covered in the literature involve analytical solutions for biporous particles^{44, 45}, nonlinear equilibrium effects⁴⁷, heat effects⁴⁸, a 'zero length criterion' for ZLC⁴⁹ and diffusion in the liquid phase⁵⁰. Among the diffusivities reported by this technique are benzene in NaX⁵¹, linear paraffins and benzene in silicalite⁵², benzene in NaX and CaX⁴⁵, n-pentane in pellets of 5A⁵³, p-xylene and o-xylene in aluminophosphate AlPO₄-11⁵⁴, cyclohexane in ZSM-5⁴⁹, propane and propylene in pellets and crystals of 5A zeolite⁵⁵, benzene and p-xylene in silicalite⁵⁶ and counterdiffusion of p-xylene/benzene and p-xylene/o-xylene in silicalite⁵⁷.

1.6 Deactivation of Zeolite Adsorbents

Deactivation of an adsorbent like that of a catalyst, involving either a loss of adsorption capacity or an increase in mass transfer resistance, commonly occurs as a result of coke formation, partial pore closure or slow loss of crystallinity. Such problems are very common in thermal swing cycles where the zeolite adsorbent is used for drying of gases or vapors. During thermal regeneration the zeolite adsorbent is exposed to severe hydrothermal conditions, i.e. a combination of high temperature and high moisture concentration. Zeolite X tends to lose its crystal structure under such severe conditions. Under similar conditions, zeolite A may deactivate by partial closure of micropore openings termed as partial pore closure or pore mouth closure. Partial pore closure leads

to an additional resistance to mass transfer. When reactive hydrocarbons such as olefins are present, slow formation of polymeric species may occur within and outside the zeolite crystals. On thermal regeneration these species are converted to coke, leading to a decline in adsorbent capacity and micropore and/or macropore diffusivity.

As discussed above, under actual hydrothermal conditions in thermal regeneration zeolite 4A does not lose its crystal structure. Therefore, in the present section we restrict our discussion to deactivation caused by partial pore closure or coke formation.

Unlike catalysis, the literature on deactivation of adsorbents is rather limited. There have been a number of experimental studies, which demonstrate that the adsorbents do tend to deactivate under severe hydrothermal conditions. Kondis and Dranoff⁵⁸ showed that the uptake rate of ethane on severely hydrothermally pretreated zeolite 4A crystals was much lower than in crystals which had been carefully pretreated. Ruthven¹ has reported a set of accelerated aging tests on zeolite 13X and 4A. The results show that even under the relatively milder conditions of experiments these two zeolites tend to lose their adsorption capacity as a result of deactivation.

There are, in principle, two distinct ways in which the sorption kinetics may be retarded by hydrothermal pretreatment: either the pore entrances at the crystal surface may be obstructed or the windows in the interior of the pores may be blocked. The former is equivalent to a *surface barrier* or pore mouth resistance while the latter leads to a decrease in micropore diffusivity. Mass transfer across the pore mouth is a rate process and window blocking leads to a decrease in micropore diffusivity without significantly

altering the activation energy for diffusion⁵⁹. Thus, the two mechanisms are, at least in principle, kinetically distinguishable.

Kinetic uptake rate measurements of *n*-decane in various hydrothermally pretreated samples of 5A zeolite show that the pore mouth resistance increases with increasing severity of hydrothermal treatment^{60,61}. However, the extensive uptake rate data reported by Kondis and Dranoff^{58,62} for ethane in hydrothermally treated samples of 4A zeolite as well as the data of Ruthven and coworkers^{63,64,65} for linear paraffins in commercial samples of zeolite 5A indicate that the micropore diffusivity decreases with increasing hydrothermal severity and that pore mouth resistance is not present.

The effect of hydrothermal treatment has also been studied by NMR methods. Micropore diffusivity and the pore mouth resistance can be directly determined by NMR methods. NMR studies on severe hydrothermal dehydration of 5A zeolite, with methane as the probe molecule, give a clear evidence of the development of a pore mouth resistance^{66,67,68}. The magnitude of the pore mouth resistance increases with increasing severity of hydrothermal treatment whereas the micropore diffusivity remains almost a constant⁶⁹. This effect has been confirmed using several different probe molecules⁷⁰. The NMR results are supplemented by X-ray photoelectron spectroscopy studies which reveal a decrease in the Al/Si ratio at the crystal surface resulting in a narrowing of the pore mouth⁷¹.

The kinetic behavior of CaNaA-type zeolites is deteriorated by hydrothermal treatment but the adsorption isotherm remains unchanged⁷². The diffusion of adsorbed

molecules is drastically hindered due to the development of surface barrier. Thermal frequency response method and pulsed field gradient NMR have been used to study water diffusion in zeolite NaX⁷³. A significant change in the diffusion behavior of water molecules is observed in severely hydrothermally treated samples.

The mass transfer properties of a commercial 5A adsorbent, used in a petroleum refinery, have been investigated, as a function of the time on stream, using the NMR technique^{69, 74}. The results indicate a continuous increase in pore mouth resistance with very little change in micropore diffusivity. It seems clear that the slow buildup of carbonaceous deposits leads to the observed increase in pore mouth resistance.

Therefore, both uptake rate measurements and NMR results show a loss in adsorbent activity when exposed to severe hydrothermal conditions. However, the results of sorption rate and NMR measurements are somewhat in conflict as the former suggests that the primary mechanism of deactivation is that of window blocking leading to a decrease in micropore diffusivity while the latter suggests that pore mouth resistance is the dominating effect.

Diffusion of water molecules has been studied in NaCaA zeolites using quasi-elastic neutron scattering (QENS) and PFG-NMR⁷⁵. It is found that both techniques exhibit similar trends of increasing water diffusivity with increasing loading and with decreasing calcium content. Mass transfer of alkanes in zeolites has been studied using positron-emission profiling^{76, 77}.

1.7 Layout of Dissertation

This dissertation is arranged as follows:

1. A pore blockage model is proposed in chapter two to predict the kinetic behavior of a deactivated 4A zeolite crystal.
2. In chapter three, modeling for breakthrough curves for a dual site isotherm is presented and experimental data is fitted to the model.
3. Experimental study on deactivation of 4A zeolite pellets is presented and discussed in chapter four.
4. Conclusions and recommendations are presented in chapter five.

2

KINETICS OF SORPTION IN DEACTIVATED ZEOLITE CRYSTAL ADSORBENTS

Zeolites are widely used for catalytic and adsorptive applications. Adsorptive applications include drying, hydrocarbon separation, separation and purification of industrial streams. One of the main industrial adsorption processes, based on 4A zeolite, is the drying of process streams. One major problem encountered in using 4A zeolite for drying is that it deactivates with time. Deactivation of 4A zeolite involves either a loss of adsorption capacity or an increase in mass transfer resistance, commonly occurring as a result of coke formation, or partial pore closure. Coke formation in zeolites results due to the presence of hydrocarbon gases or vapors⁷⁸. Partial pore closure results due to preferential closure of micropore openings in presence of water at high temperature such as 350 °C^{58 . 61 . 60 . 68 . 67 . 66 . 71 . 74 . 69 . 70}. In general, both of these mechanisms may lead to the blockage of a fraction of the crystal surface, thereby decreasing the surface area available for mass transfer.

There is qualitative evidence available in the literature, which indicates that one or both of these two mechanisms is responsible for the deactivation of 4A zeolite. However, no attempt has yet been made to quantitatively model the phenomenon of deactivation or

the impact of deactivation on sorption characteristics of 4A zeolite. Present work deals with the second part of the problem. A mathematical model has been developed to investigate the effect of partial surface blockage of a crystal particle of cylindrical shape in lieu of the cubic crystal for simplicity. The mathematical model is solved numerically using the orthogonal collocation technique.

2.1 Theoretical Model for a Crystalline Particle

Consider a zeolite crystal particle, of cylindrical morphology, having radius r_c . At time $t = 0$ a large step change is applied in surface concentration. Further, assume that a fraction A_b of the surface is blocked and hence the radial flux in this region of the surface is zero. The mathematical statement of this problem is

$$\frac{\partial q}{\partial t} = \frac{1}{r} \frac{\partial}{\partial r} \left(r D_c \frac{\partial q}{\partial r} \right) + \frac{1}{r^2} \frac{\partial}{\partial \theta} \left(D_c \frac{\partial q}{\partial \theta} \right) \quad (2-1)$$

with the initial condition

$$q(r, \theta, 0) = q_i \quad (2-2)$$

and boundary conditions

$$\begin{aligned}
q(r,0,t) &= q(r,2\pi,t) \\
\frac{\partial q}{\partial \theta}(r,0,t) &= \frac{\partial q}{\partial \theta}(r,2\pi,t) \\
\lim_{r \rightarrow 0} \int_0^{2\pi} \frac{\partial q}{\partial r}(r,\theta,t) d\theta &= 0 \tag{2-3} \\
q(r_c, \theta, t) &= q_s \quad \text{in the exposed region of the surface } (1 - A_b) \text{ and} \\
\frac{\partial q}{\partial r}(r_c, \theta, t) &= 0 \quad \text{in the blocked region of the surface } (A_b)
\end{aligned}$$

where D_c is the intracrystalline diffusivity, q is the adsorbate concentration, q_s is the adsorbate concentration at the outside surface of the crystal, and r , θ , and t are the radial, polar, and time coordinates, respectively. The proof of integral boundary condition in Eq. 2-3 is presented in the following section.

2.1.1 Proof of Integral Boundary Condition

Assume a solid cylinder of radius $r_s \leq r_c$. An unsteady state material balance over this cylinder gives us

$$\frac{\partial(\pi r_s^2 L \bar{q})}{\partial t} = - \int_0^{2\pi} L r_s \left(D_c \frac{\partial q}{\partial r} \right)_r d\theta \tag{2-4}$$

where \bar{q} is the concentration averaged over the solid cylinder, all other variables have their usual meaning defined earlier. Simplification of Equation 2-4 gives

$$\frac{\partial \bar{q}}{\partial t} = - \frac{D_c}{\pi r_s} \int_0^{2\pi} \left(\frac{1}{1 - q/q_{sat}} \frac{\partial q}{\partial r} \right)_r d\theta \tag{2-5}$$

In the limit $r_s \rightarrow 0$, we will have $\bar{q} = q$, and q independent of θ . Therefore, we get

$$\frac{\partial q}{\partial t} = -\lim_{r_s \rightarrow 0} \frac{D_o}{(1 - q/q_{sat})^n r_s} \int_0^{2\pi} \left. \frac{\partial q}{\partial r} \right|_{r_s} d\theta \quad (2-6)$$

Thus, for the concentration to be finite at the center the integral term must approach zero at least as fast as the denominator, i.e. r_s or

$$\lim_{r_s \rightarrow 0} \int_0^{2\pi} \left. \frac{\partial q}{\partial r} \right|_{r_s} d\theta = 0 \quad (2-7)$$

This is the general boundary condition required at the center of a cylinder. The symmetry boundary condition is a special case of Eq. 2-7 for a case where for physical reasons the flux or $\partial q/\partial r$ can be expected to be independent of θ . Since, in the present study, the flux is not independent of θ at the crystal surface, it is likely that it will be so even at the center of the cylinder. For example, consider a cylinder with 359° insulated, and only 1° exposed to the adsorbate.

If the step change in concentration is large then the concentration dependence of the intracrystalline diffusivity must be taken into account¹. For 4A zeolite this relationship is given as

$$D_c = D_o \frac{d \ln q}{d \ln c} \quad (2-8)$$

where D_o is an intrinsic diffusivity. Therefore, for Langmuir isotherm the dependence of D_c on concentration becomes

$$D_c = D_o \left(1 - \frac{q}{q_{sat}} \right)^{-1} \quad (2-9)$$

where q_{sat} is the adsorbate concentration at monolayer saturation^{79.5.1}. Thus, it can be seen that the intracrystalline diffusivity becomes very large as $q \rightarrow q_{sat}$. In such cases other mass transfer mechanisms like pore mouth resistance or mass transfer at the surface may become the limiting factor.

The normalized form of Eq. (2-9) is

$$D_c = D_o \left[1 - \lambda_i - (\lambda_s - \lambda_i) q^* \right]^{-1} \quad (2-10)$$

The normalized form of the model equations given above is

$$\frac{\partial q^*}{\partial t^*} = \frac{1}{r^*} \frac{\partial}{\partial r^*} \left(\frac{r^*}{1 - \lambda_i - (\lambda_s - \lambda_i) q^*} \frac{\partial q^*}{\partial r^*} \right) + \frac{1}{4\pi^2 r^{*2}} \frac{\partial}{\partial \theta^*} \left(\frac{1}{1 - \lambda_i - (\lambda_s - \lambda_i) q^*} \frac{\partial q^*}{\partial \theta^*} \right) \quad (2-11)$$

with the initial condition

$$q^*(r^*, \theta^*, 0) = 0 \quad (2-12)$$

and the boundary conditions

$$q^*(r^*, 0, t^*) = q^*(r^*, 1, t^*) \quad (2-13)$$

$$\frac{\partial q^*}{\partial \theta^*}(r^*, 0, t^*) = \frac{\partial q^*}{\partial \theta^*}(r^*, 1, t^*) \quad (2-14)$$

$$\lim_{r^* \rightarrow 0} \int_0^1 \frac{\partial q^*}{\partial r^*} (r^*, \theta^*, t^*) d\theta^* = 0 \quad (2-15)$$

$$\begin{aligned} q^*(1, \theta^*, t^*) &= 1 && \text{in the exposed region of the surface } (1 - A_b) \text{ and} \\ \frac{\partial q^*}{\partial r^*}(1, \theta^*, t^*) &= 0 && \text{in the blocked region of the surface } (A_b) \end{aligned} \quad (2-16)$$

where $q^* = (q - q_i)/(q_s - q_i)$, $r^* = r/r_c$, $\theta^* = \theta/2\pi$, and $t^* = tD_s/r_c^2$ are dimensionless adsorbed phase concentration, radial, polar, and time coordinates, respectively. Parameters λ_i and λ_s in Eq. (2-11) are defined as $\lambda_i = q_i/q_{sat}$, and $\lambda_s = q_s/q_{sat}$, respectively. The difference between these parameters is a measure of the nonlinearity of the Langmuir isotherm. $|\lambda_s - \lambda_i| \rightarrow 0$ corresponds to the case of a linear isotherm and $|\lambda_s - \lambda_i| \rightarrow 1$ corresponds to the case of an irreversible or rectangular isotherm.

Two key parameters in solving the above model equations are the total fraction of crystal surface blocked, A_b , and its distribution. For a fixed value of A_b the blocked surface can be distributed as infinitely long strips or patches on the surface of the cylinder. The blocked area may be distributed equally among these patches or may be governed by some kind of distribution. In the present study we assume that the blocked area is distributed equally in n_p patches. We may, therefore, describe the distribution of blockage in terms of the number of patches, n_p . Thus, for a given value of A_b the blocked surface may be distributed uniformly in one, two or more equal patches as illustrated in Figure 2-1. $n_p = 1$ corresponds to the case when blockage is concentrated in one part of the cylinder surface and $n_p \rightarrow \infty$ corresponds to a completely uniform distribution of blockage.

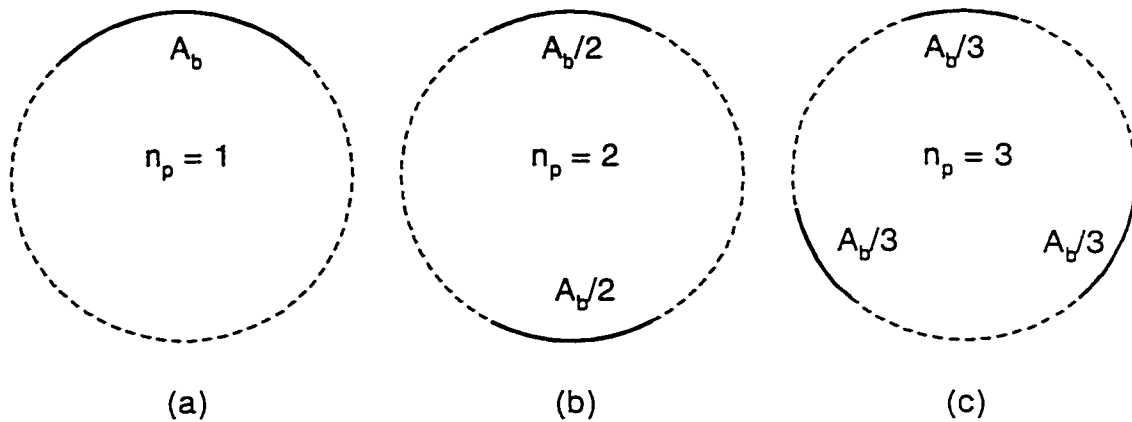


FIGURE 2-1 Illustration of the distribution of blocked area on the surface. Solid line corresponds to the blocked region and the dashed line corresponds to the exposed region.

2.2 Numerical technique

The model equations 2-11, through 2-16 for sorption in the crystal are solved using the orthogonal collocation technique⁸⁰. To solve the model equations for the crystal, a sector of surface with angle $\Delta\theta^* = 1/2n_p$ was considered. The sector was chosen in such a way that it included half of one patch of the blocked area and half of one patch of adjacent exposed area with areas $A_b/2n_p$ and $(1-A_b)/2n_p$, respectively. In this way the solution over the selected sector will represent that over the entire cylindrical crystal due to symmetry. An illustration of this is shown in Figure 2-2. The boundary conditions at $\theta = 0$ and 2π are replaced by the symmetry conditions at $\theta = 0$ and $\theta = 1/2n_p$, as shown in the figure.

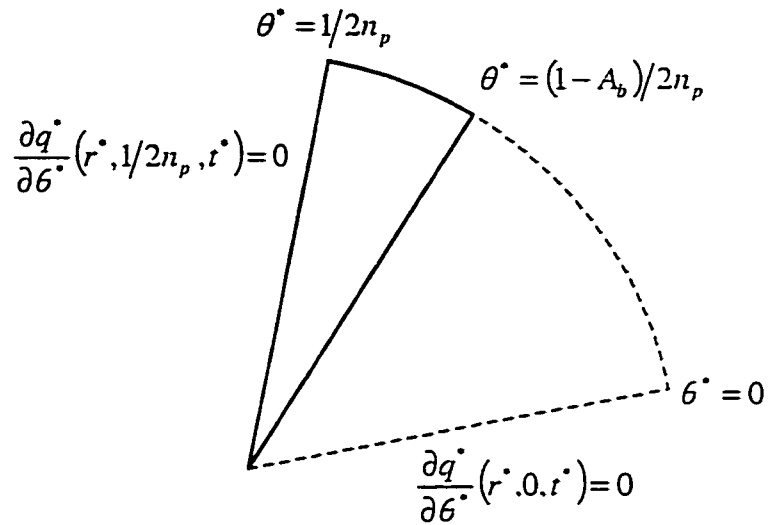


FIGURE 2-2 A symmetric sector of angle $1/2n_p$. Dashed line corresponds to the exposed region and solid line corresponds to the blocked region. The area of exposed region is $(1-A_b)/2n_p$ and that of the blocked region is $A_b/2n_p$. The θ -fluxes at the two boundaries are zero due to symmetry.

The model Eqs. 2-11, 2-12, and 2-16 are rewritten and renormalized separately for both blocked and unblocked elements of the representative sector. The resulting partial differential equations for each element are

$$\begin{aligned}
 \frac{\partial q_1^*}{\partial t^*} &= \frac{1}{r^*} \frac{\partial}{\partial r^*} \left(\frac{r^*}{1 - \lambda_i - (\lambda_s - \lambda_i) q_1^*} \frac{\partial q_1^*}{\partial r^*} \right) \\
 &\quad + \left(\frac{n_p}{\pi(1 - A_b)} \right)^2 \frac{1}{r^{*2}} \frac{\partial}{\partial \theta_1^*} \left(\frac{1}{1 - \lambda_i - (\lambda_s - \lambda_i) q_1^*} \frac{\partial q_1^*}{\partial \theta_1^*} \right) \\
 \frac{\partial q_2^*}{\partial t^*} &= \frac{1}{r^*} \frac{\partial}{\partial r^*} \left(\frac{r^*}{1 - \lambda_i - (\lambda_s - \lambda_i) q_2^*} \frac{\partial q_2^*}{\partial r^*} \right) \\
 &\quad + \left(\frac{n_p}{\pi A_b} \right)^2 \frac{1}{r^{*2}} \frac{\partial}{\partial \theta_2^*} \left(\frac{1}{1 - \lambda_i - (\lambda_s - \lambda_i) q_2^*} \frac{\partial q_2^*}{\partial \theta_2^*} \right)
 \end{aligned} \tag{2-17}$$

with the initial conditions

$$\begin{aligned}
q_1^*(r^*, \theta_1^*, 0) &= 0 \\
q_2^*(r^*, \theta_2^*, 0) &= 0
\end{aligned}
\tag{2-18}$$

and the boundary conditions

$$\begin{aligned}
\frac{\partial q_1^*}{\partial \theta_1^*}(r^*, 0, r^*) &= 0 \\
q_1^*(r^*, 1, r^*) &= q_2^*(r^*, 0, r^*) \\
\frac{\partial q_1^*}{\partial \theta_1^*}(r^*, 1, r^*) &= \frac{\partial q_2^*}{\partial \theta_2^*}(r^*, 0, r^*) \\
\frac{\partial q_2^*}{\partial \theta_2^*}(r^*, 1, r^*) &= 0 \\
q_1^*(1, \theta_1^*, r^*) &= 1 \\
\frac{\partial q_2^*}{\partial r^*}(1, \theta_2^*, r^*) &= 0 \\
(1 - A_b) \int_0^1 \frac{\partial q_1^*}{\partial r^*}(0, \theta_1^*, r^*) dr^* + (A_b) \int_0^1 \frac{\partial q_2^*}{\partial r^*}(0, \theta_2^*, r^*) dr^* &= 0
\end{aligned}
\tag{2-19}$$

where all the symbols with a subscript 1 are the corresponding properties calculated in the element 1, and those with a subscript 2 are the corresponding properties calculated in the element 2 of the sub sector. Polar coordinates θ_1^* , and θ_2^* are defined as

$$\begin{aligned}
\theta_1^* &= \frac{2n_p}{1 - A_b} \theta^* \\
\theta_2^* &= \frac{2n_p}{A_b} \theta^* + 1 - \frac{1}{A_b}
\end{aligned}
\tag{2-20}$$

In principle, the above model equations can be solved numerically to obtain the uptake curves in the crystal. However, as $|\lambda_s - \lambda_i|$ becomes large i.e. approaches 1, the model equations become increasingly stiff and the computation time increases rapidly.

Therefore, a transformation of the model Eqs. 2-17, 2-18, and 2-19 is made by introducing a transformation variable u , defined as

$$u = \ln[1 - \lambda_i - (\lambda_s - \lambda_i)A^*] \quad (2-21)$$

The transformed model equations are

$$\begin{aligned} \frac{\partial u_1}{\partial t^*} &= e^{-u_1} \left[\frac{1}{r^*} \frac{\partial}{\partial r^*} \left(r^* \frac{\partial u_1}{\partial r^*} \right) + \left(\frac{n_p}{\pi(1-A_b)} \right)^2 \frac{1}{r^{*2}} \frac{\partial^2 u_1}{\partial \theta_1^{*2}} \right] \\ \frac{\partial u_2}{\partial t^*} &= e^{-u_2} \left[\frac{1}{r^*} \frac{\partial}{\partial r^*} \left(r^* \frac{\partial u_2}{\partial r^*} \right) + \left(\frac{n_p}{\pi A_b} \right)^2 \frac{1}{r^{*2}} \frac{\partial^2 u_2}{\partial \theta_2^{*2}} \right] \end{aligned} \quad (2-22)$$

with the transformed initial conditions

$$u_1(r^*, \theta_1^*, 0) = u_2(r^*, \theta_2^*, 0) = \ln(1 - \lambda_i) \quad (2-23)$$

and the transformed boundary conditions

$$\begin{aligned} \frac{\partial u_1}{\partial \theta_1^*}(r^*, 0, t^*) &= 0 \\ u_1(r^*, 1, t^*) &= u_2(r^*, 0, t^*) \\ \frac{\partial u_1}{\partial \theta_1^*}(r^*, 1, t^*) &= \frac{\partial u_2}{\partial \theta_2^*}(r^*, 0, t^*) \\ \frac{\partial u_2}{\partial \theta_2^*}(r^*, 1, t^*) &= 0 \\ u_1(1, \theta_1^*, t^*) &= \ln(1 - \lambda_s) \\ \frac{\partial u_2}{\partial r^*}(1, \theta_2^*, t^*) &= 0 \\ (1 - A_b) \int_0^1 \frac{\partial u_1}{\partial r^*}(0, \theta_1^*, t^*) d\theta_1^* + A_b \int_0^1 \frac{\partial u_2}{\partial r^*}(0, \theta_2^*, t^*) d\theta_2^* &= 0 \end{aligned} \quad (2-24)$$

In order to solve the transformed model Eqs. 2-22, 2-23, and 2-24, it is necessary to select the collocation points both in radial and polar coordinates of both the elements of the sector. Collocation points in the polar coordinates are chosen to be the roots of Legendre polynomials. Collocation points in the radial direction are chosen to be the roots of Jacobi polynomials⁸¹ $G_n(p,q,x)$ with $p = q = 2$.

Grid independent results are obtained for sixteen collocation points in radial direction and eight collocation points in polar direction in each of the subsectors. Further increase in collocation points did not improve the solution. Collocation scheme leads to approximately 256 coupled ODEs which were solved using `ode15s` in Matlab on a PIII IBM with 128 Mb RAM. The differential equations become increasingly stiff as the nonlinearity of isotherm i.e. $|\lambda_i - \lambda_s|$ is increased. The differential equations for adsorption took considerably longer time to solve than for desorption for a nonlinear isotherm. The computation time for adsorption varied from 10 to 30 min depending upon the value of n_p and nonlinearity of isotherm taking longer for large values of n_p . The computation time for desorption was approximately 5 min for all cases and had little effect of either the value of n_p or the nonlinearity of isotherm.

2.3 Results and Discussion

The dimensionless adsorbed phase concentration profiles, q^* , are plotted in Figure 2-3. As the fractional blockage, A_b , increases diffusion to the inner core of the cylinder gets slower resulting in a low uptake rate. The uptake curves for adsorption and for a linear

isotherm i.e. $|\lambda_r - \lambda_i| \rightarrow 0$, are plotted in Figure 2-4. In the figure m_t is the mass of adsorbate adsorbed at any time t^* and m_∞ is that at $t^* \rightarrow \infty$. It can be seen from the figure that as the blocked area A_b increases the uptake rate decreases. All the uptake curves show a linear long time behavior on a semilog plot. The uptake curves for desorption, for a linear isotherm are identical to the uptake curves when m_t and m_∞ are defined as the mass desorbed at time t^* and $t^* \rightarrow \infty$, respectively.

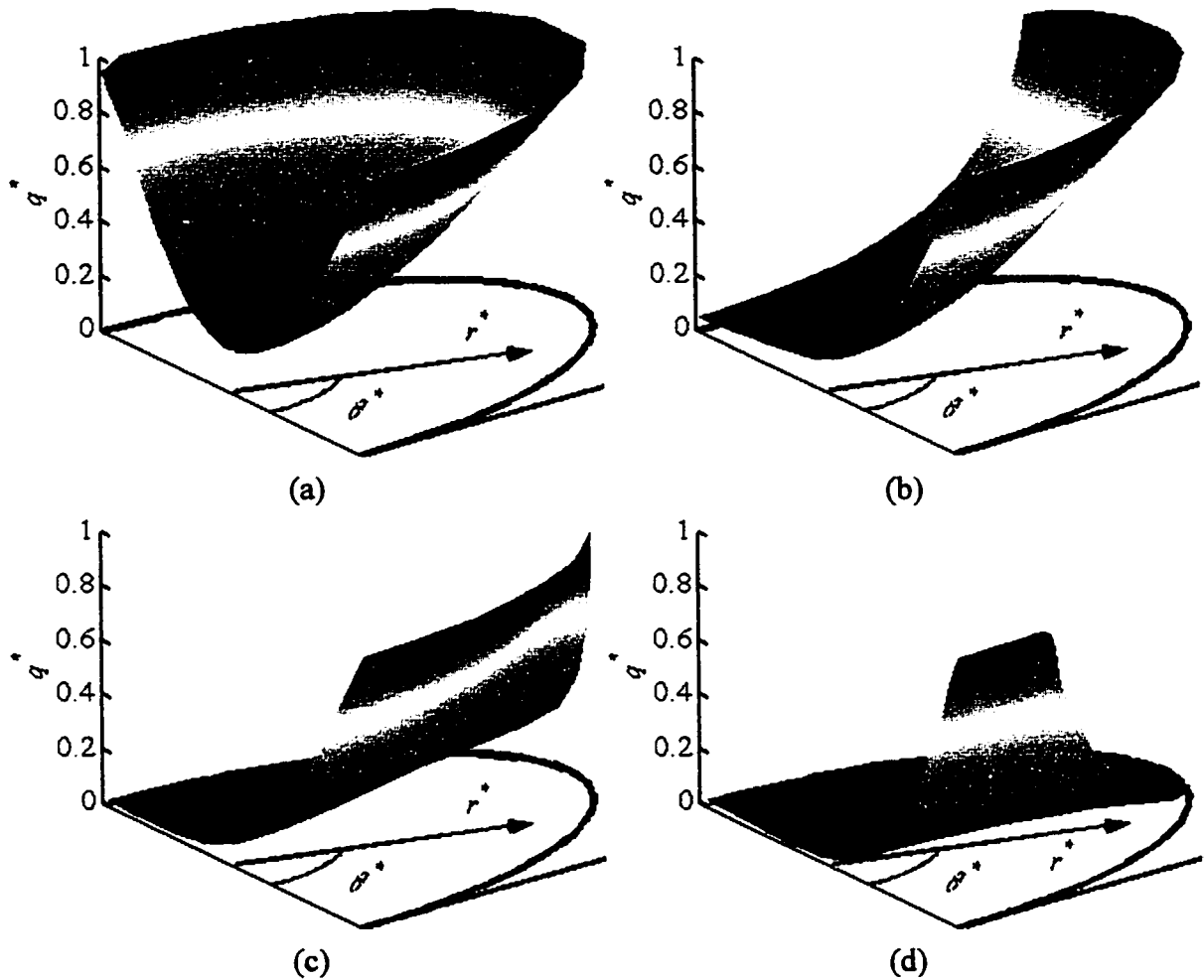


FIGURE 2-3 Adsorbed phase concentration profiles in the crystal at $t^* = 0.10$. Profiles have been obtained for various values of A_b as specified in the figures, $n_p = 1$, $|\lambda_s - \lambda_l| = 0$, and during adsorption. Only half of the cylindrical cross section has been shown due to symmetry. $A_b = 0.0$ for (a), $A_b = 0.30$ for (b), $A_b = 0.60$ for (c), $A_b = 0.90$ for (d).

Effect of varying n_p on the uptake rate is illustrated in Figure 2-5, obtained for $A_b = 0.99$. It can be seen from the figure that an increase in n_p significantly increases the uptake rate. This is due to a decrease in diffusion length in θ direction with an increase in n_p or the uniformity of blockage distribution. As n_p is increased to a very high value an

asymptotic behavior is obtained which corresponds to the completely uniform blockage distribution. This asymptotic behavior is obtained for $n_p > 32$ as is evident from the figure.

Ratio of time required for 99% adsorption at a given A_b to that at $A_b = 0$ are plotted in Figure 2-6. The curves are obtained for a linear isotherm and for various values of n_p as indicated in the figure. As can be seen from the figure, the ratio of adsorption times increases rapidly as A_b is increased beyond 0.8. However, as A_b is distributed more uniformly i.e. n_p is increased, the adsorption time decreases very rapidly. For a given A_b , the lowest adsorption time will be attained when the blockage is completely uniformly distributed i.e. $n_p \rightarrow \infty$. Numerically, this limit is approached for $n_p > 32$. All the curves in Figure 2-6 could be fitted to an equation of the form

$$\frac{t_{99}}{(t_{99})_{A_b=0}} = 1 + aA_b + bA_b^2 + cA_b^3 + d \frac{A_b}{1-A_b} + e \left(\frac{A_b}{1-A_b} \right)^2 \quad (2-25)$$

The parameters a , b , c , d , and e for each curve are listed in Table 2-1.

TABLE 2-1 Values of parameters used in Eq. (2-25), obtained by fitting the equation to the numerical values.

n_p	a	b	c	d	e	Max. Rel. Error
1	0.2289	6.7462	4.1717	0.4002	-2.3626e-3	2.88 %
2	0.1297	1.6149	3.7869	0.1967	-1.1321e-3	2.02 %
4	0.1686	-6.6711e-3	2.5193	0.0997	-5.2333e-4	1.21 %
512	0.0330	-0.0782	0.0534	0.0210	3.4153e-5	0.39 %

The uptake curves both for adsorption and desorption for a nonlinear isotherm i.e.

$|\lambda_s - \lambda_i| > 0$ are plotted in Figure 2-7. It can be seen that as nonlinearity is increased both adsorption and desorption rates increase. This is because intracrystalline diffusivity for a nonlinear isotherm is always greater than that for a linear isotherm wherein $D_c = D_o$. However, for a given value of $|\lambda_s - \lambda_i|$, adsorption is always faster than desorption and adsorption increases much more rapidly than desorption. This is because during desorption there is low concentration in the outer shell which slows down the mass transfer due to low intracrystalline diffusivity. Furthermore, it can be seen from the figure that for large values of $|\lambda_s - \lambda_i|$ adsorption uptake curves show two regions of linearity on a semilog plot corresponding to the intermediate and long range of t^* . For an anti-Langmuir isotherm where $D_c = D_o (1 - q/q_{sat})$ the rate of desorption will be faster than the adsorption.

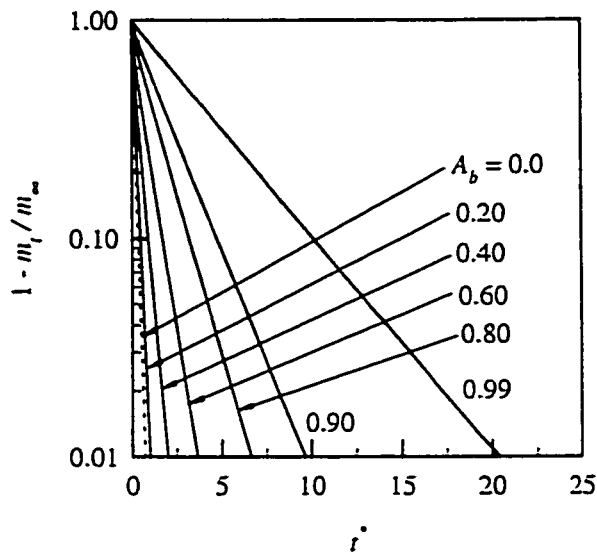


FIGURE 2-4 Uptake curves for various values of A_b as specified in the figure. All the curves are obtained for a linear isotherm i.e. $|\lambda_s - \lambda_l| \rightarrow 0$ and for $n_p = 1$.

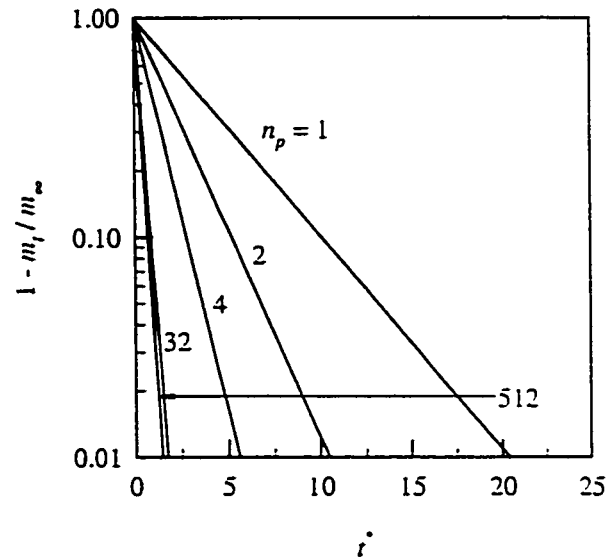


FIGURE 2-5 Effect of varying n_p on the uptake curves. Uptake curves have been obtained for a linear isotherm with $A_b = 0.99$.

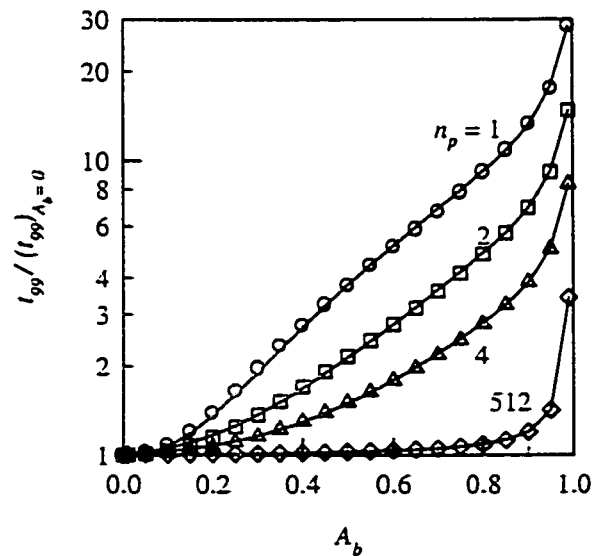


FIGURE 2-6 Ratio of time required for 99 % adsorption at a given A_b to that at $A_b = 0$. Curves are obtained for various values of n_p as shown in the figure. Symbols correspond to the actual values obtained from numerical solution and the solid lines correspond to the data fitted to a function of A_b .

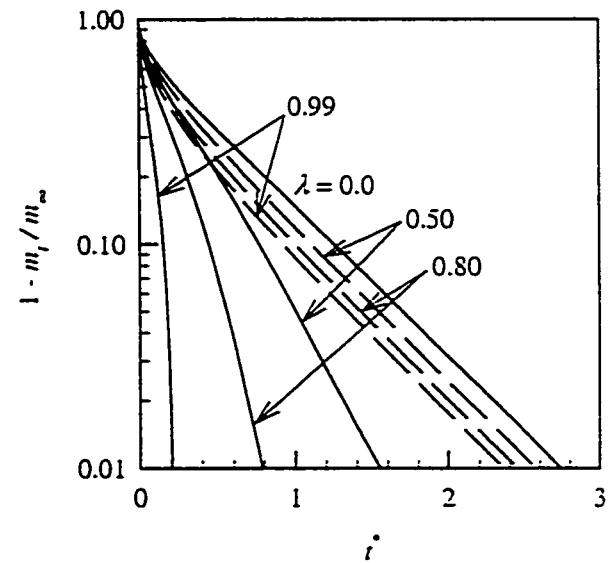


FIGURE 2-7 Adsorption and desorption rate curves for nonlinear isotherms. The curves have been obtained for $A_b = 0.5$ and $n_p = 1$. Solid lines correspond to adsorption and dashed lines to desorption rate curves. $\lambda = |\lambda_s - \lambda_l|$

2.4 Conclusions

Pore mouth closure is modeled as complete blockage of a fraction of the crystal surface. This model can also be used for modeling the sorption in a crystal deactivated due to coking. A concentrated blockage of a fraction of a cylindrical crystal can significantly reduce the rate of mass transfer in a crystal.

3

MODELING OF BREAKTHROUGH CURVES FOR DUAL SITE ISOTHERMS OF 4A MOLECULAR SIEVE PELLETS AT INTERMEDIATE TEMPERATURES

Experimental kinetic data for zeolitic systems obtained by gravimetric, volumetric, or breakthrough curve measurement technique is fitted to theoretical curves to derive the kinetic parameters like macropore/micropore diffusion coefficients or mass transfer coefficient for diffusion across micropore pore openings (also called pore mouth resistance). The speed and simplicity of experimentation offered by the breakthrough curve measurement technique makes it especially suitable for the present work. However, the analysis of experimental data may be complicated by intrusion of dispersion and external fluid film resistance effects. The analysis of experimental kinetic data obtained by the techniques mentioned above may be further complicated by the nonlinearity of adsorption isotherm.

Analytic expressions can be obtained for breakthrough curve when the adsorption isotherm is linear^{10 - 23} and under isothermal conditions. Theoretical breakthrough curves for nonlinear systems have been calculated by numerical solution of the model equations

using standard finite difference or collocation methods. In most of these studies plug flow is assumed and the equilibrium isotherm is either Langmuir or Freundlich^{3 - 9}. The earliest solution for the breakthrough curve for an irreversible system is due to Bohart and Adams²⁴ who used a quasi-chemical rate expression. The cases of micropore diffusion control and macropore diffusion control were solved by Cooper²⁵ and by Cooper and Libermann²⁶. All the literature available on water-4A zeolite system assumes the adsorption isotherm to be single site Langmuir⁴², Freundlich^{34, 32, 33} or irreversible⁸²⁻⁴ isotherm. This is generally true only at high surface coverage. The water-4A zeolite isotherm data sheets published by Linde and Zeochem cannot be fitted to these single site adsorption isotherms especially at low to intermediate surface coverage.

In water-4A zeolite systems micropore diffusion is very rapid in comparison to other mass transfer mechanisms and is not significant, especially in commercially available 4A zeolite pellets. Macropore resistance is generally the controlling mass transfer resistance in fresh 4A zeolite pellets. However, with the passage of time the mass transfer regime shifts from a single resistance to a dual resistance regime due to deactivation where mass transfer is controlled by both macropore diffusion and the pore mouth resistance.

In order to analyze the experimental kinetic data, equilibrium effects must be separated from the kinetic effects. Equilibrium behavior of any adsorption system is represented in terms of an isotherm which basically relates the concentration or partial pressure of the sorbate in fluid stream to its concentration in the sorbed phase. Separate experiments need to be performed to determine adsorption isotherm, especially if the isotherm is of a complex nature as in water-4A zeolite systems. The mathematical model

to calculate the theoretical breakthrough curves is presented in the next section followed by sections on experimental details for determining equilibrium isotherm, pore size distribution, particle size distribution and breakthrough curve measurements.

3.1 Mathematical Model

Consider a column packed with spherical adsorbent pellets. The adsorbent consists of 4A zeolite crystals compacted together with binder to give a biporous adsorbent pellet. Assume that the intraparticle resistance to mass transfer is due to diffusion in the macropores and due to diffusion across the micropore pore openings. We also assume that the adsorption takes place under isothermal conditions. Flow through a packed bed may generally be adequately represented by the axial dispersed plug flow model:

$$-D_L \frac{\partial^2 c_b}{\partial z^2} + \frac{\partial}{\partial z}(vc_b) + \frac{\partial c_b}{\partial t} + \frac{1-\varepsilon_b}{\varepsilon_b} \frac{\partial \bar{q}}{\partial t} = 0 \quad (3-1)$$

For a single component trace system such as involving dehydration, v is approximately a constant so that the model simplifies to

$$-D_L \frac{\partial^2 c_b}{\partial z^2} + v \frac{\partial c_b}{\partial z} + \frac{\partial c_b}{\partial t} + \frac{1-\varepsilon_b}{\varepsilon_b} \frac{\partial \bar{q}}{\partial t} = 0 \quad (3-2)$$

Diffusion in the macropores of a spherical pellet can be described by the Fickian diffusion equation:

$$\frac{\partial c_m}{\partial t} + \frac{1-\varepsilon_p}{\varepsilon_p} \frac{\partial q}{\partial t} = \frac{1}{R^2} \frac{\partial}{\partial R} \left(D_p R^2 \frac{\partial c_m}{\partial R} \right) \quad (3-3)$$

where D_p is the macropore diffusivity and is approximately independent of the macropore concentration. Therefore, the macropore diffusion equation simplifies to

$$\frac{\partial c_m}{\partial t} + \frac{1 - \varepsilon_p}{\varepsilon_p} \frac{\partial q}{\partial t} = \frac{D_p}{R^2} \frac{\partial}{\partial R} \left(R^2 \frac{\partial c_m}{\partial R} \right) \quad (3-4)$$

Diffusion across the micropore pore openings can be described in terms of a rate equation:

$$\frac{\partial q}{\partial t} = \frac{3k_s}{r_c} (q_e - q) \quad (3-5)$$

Initial and boundary conditions for these differential equations are:

$$c_b(z, t = 0) = c_i \quad c_m(z, R, t = 0) = c_i \quad q(z, R, t = 0) = q_i \quad (3-6)$$

$$-D_L \frac{\partial c_b}{\partial z}(z = 0, t) = v[c_o - c_b(z = 0, t)] \quad (3-7)$$

$$\frac{\partial c_b}{\partial z}(z = L, t) = 0 \quad (3-8)$$

$$\frac{\partial c_m}{\partial R}(z, R = 0, t) = 0 \quad (3-9)$$

$$c_m(z, R = R_p, t) = c_b(z, t) \quad (3-10)$$

The model equations 3-2, 3-4, and 3-5 can be normalized to give the following dimensionless differential equations:

$$-\frac{\alpha_{mac-con}}{Pe} \frac{\partial^2 c_b^*}{\partial z^{*2}} + \alpha_{mac-con} \frac{\partial c_b^*}{\partial z^*} + \beta_b \frac{\partial c_b^*}{\partial t^*} + \frac{\partial \bar{q}^*}{\partial t^*} = 0 \quad (3-11)$$

$$\beta_p \frac{\partial c_m^*}{\partial t^*} + \frac{\partial q^*}{\partial t^*} = \frac{1}{R^{*2}} \frac{\partial}{\partial R^*} \left(R^{*2} \frac{\partial c_m^*}{\partial R^*} \right) \quad (3-12)$$

$$\frac{\partial q^*}{\partial t^*} = \alpha_{mac-pm} (q_e^* - q^*) \quad (3-13)$$

The corresponding dimensionless initial and boundary conditions are:

$$c_b^*(z^*, t^* = 0) = c_i^*, \quad c_m^*(z^*, R^*, t^* = 0) = c_i^*, \quad q^*(z^*, R^*, t^* = 0) = q_i^* \quad (3-14)$$

$$-\frac{1}{Pe} \frac{\partial c_b^*}{\partial z^*} (z^* = 0, t^*) = c_o^* - c_b^*(z^* = 0, t^*) \quad (3-15)$$

$$\frac{\partial c_b^*}{\partial z^*} (z^* = 1, t^*) = 0 \quad (3-16)$$

$$\frac{\partial c_m^*}{\partial R^*} (z^*, R^* = 0, t^*) = 0 \quad (3-17)$$

$$c_m^*(z^*, R^* = 1, t^*) = c_b^*(z^*, t^*) \quad (3-18)$$

$\alpha_{mac-con}$ in Eq. 3-11 is the ratio of macropore time constant to convection time constant. It is an indication of the significance of mass transfer limitations due to macropore resistance relative to that due to convection. Mass transfer limitation due to convection is not significant when $\alpha_{mac-con} > 10$ and macropore resistance is not significant when

$\alpha_{mac-con} < 1$. Similarly, α_{mac-pm} in equation 3-13 is the ratio of macropore time constant to pore mouth time constant β_b in Eq. 3-11 is the ratio of sorbate capacity of the fluid phase in the bed to the sorbate capacity of adsorbent calculated at equilibrium i.e. at $t = 0$ for desorption and at $t \rightarrow \infty$ for adsorption. Similarly, β_p in Eq. 3-12 is ratio of sorbate capacity of the macropores to the sorbate capacity of the solid phase in the pellet. The parameters β_b and β_p , in equations 3-11 and 3-12 respectively, are of the order of 10^{-3} making the corresponding fluid phase concentration transient terms in these equations negligible. q_e in equation 3-5 is in equilibrium with the local fluid phase concentration and is given by the adsorption isotherm equation of the form

$$q_e = f(c) \quad (3-19)$$

The exact relationship between q_e and c needs to be determined experimentally. Experimental determination of the adsorption isotherm is discussed in the following section.

Model equations 3-11 through 3-18 are solved numerically using the method of lines by finite differencing in both radial direction of the pellet and axial direction of the adsorption column. Resulting ordinary differential equations are solved using ode45 subroutine in matlab. Grid independent results are obtained for ten points in the pellet and eighty points in the axial direction of the bed. Average computation time for adsorption breakthrough curve was fifteen minutes and that for desorption breakthrough curve was 10 minutes on a Compaq P4 (2GHz) PC.

Initially, orthogonal collocation was attempted to solve the model equations but it invariably makes the differential equations stiff especially close to initial condition for the case of adsorption breakthrough curve. This requires use of stiff ode solver like ode15s which involves calculation of the jacobian. Some terms of the jacobian will involve derivative of q_e with respect to p . As discussed later in this chapter dq_e/dp has negative power dependence on p . Therefore, close to initial condition the jacobian blows up and integration fails. Setting the corresponding terms of jacobian to a large value also did not solve the problem.

Macropore diffusivity D_p in Eq. 3-4 is calculated as

$$\frac{1}{D_p} = \tau \left(\frac{1}{D_m} + \frac{1}{D_K} \right) \quad (3-20)$$

where D_m is the molecular diffusivity which, for gaseous systems, may be estimated with confidence from Chapman-Enskog⁸³ equation. For a binary gas mixture

$$D_m = \frac{0.00158T^{3/2}(1/M_1 + 1/M_2)^{1/2}}{P\sigma_{12}^2\Omega(\epsilon/kT)} \quad (\text{cm}^2\text{s}^{-1}) \quad (3-21)$$

D_K the Knudsen diffusivity may be estimated from the expression⁸⁴

$$D_K = 9700r \left(\frac{T}{M} \right)^{0.5} \quad (\text{cm}^2\text{s}^{-1}) \quad (3-22)$$

Tortuosity factor τ is treated as an empirical constant which is determined experimentally for any particular adsorbent¹.

Dispersion in gaseous systems has been reviewed by Langer et. al⁸⁵ . Ignoring the effects due to nonuniformity of packing there are two main mechanisms which contribute to axial dispersion: molecular diffusion and and turbulent mixing arising from the splitting and recombination of flows around the adsorbent particle¹ . To a first approximation these effects are additive so that the dispersion coefficient may be represented by

$$D_L = \gamma_1 D_m + \gamma_2 2R_p v \quad (3-23)$$

where γ_1 and γ_2 are constants which normally have values of about 0.7 and 0.5. More detailed investigation reveals that γ_1 is related to bed voidage as¹

$$\gamma_1 = 0.45 + 0.55\epsilon_b \quad (3-24)$$

A simple model of the bed as a series of mixing chambers, separated on average by the mean particle diameter⁸⁶ leads to $\gamma_2 = 0.5$.

3.2 Experimental Apparatus

The equilibrium sorption data for water-4A zeolite system was obtained using a constant volume apparatus operating under vacuum and the kinetic data was obtained using a breakthrough curve measurement apparatus.

A schematic diagram of the constant volume apparatus is shown in Fig 3-1. A stainless steel cell, VC, of 710.00 cc volume is connected to a high vacuum line and a flask, DW, filled with distilled water. The cell can be opened to vacuum or to water vapor

line by opening and closing valve A and control valve C. A small sample of 4A zeolite pellets is kept inside a stainless steel tube and placed in a furnace with a temperature controller. Sample tube volume is approximately 0.5 % of the volumetric cell. The sample tube is connected to the volumetric cell VC across valve D. The lower end of the sample tube is connected to the high pressure end (P1) of a Datametrics barocell across valve E. Volumetric cell, VC, is also connected to the barocell through a valve F. Pressure inside the volumetric cell alone can be measured by closing valves E and D and opening valve F. Pressure inside the sample tube alone can be measured by closing valve F and opening valve E. Valve D is used to either evacuate the sample tube or let the flow of water vapor into the sample tube. Low pressure (P2) end of the barocell is evacuated and sealed to allow us to read the absolute pressure. All the lines of the constant volume apparatus are insulated but not heated. Volumetric cell, VC, is placed inside an insulated chamber. Insulation is provided to minimize the effect of ambient temperature fluctuations. Effect of ambient pressure fluctuations is minimized by reading absolute pressure instead of relative pressure. A dual stage vacuum pump is used to obtain a vacuum of better than 10^{-6} mbar.

A schematic diagram of the breakthrough curve measurement apparatus is shown in Figure 3-2. Helium is used as carrier gas. Dry helium first passes through the reference side of a thermal conductivity detector cell. The carrier gas is saturated to a known moisture concentration by passing it through a bubbler maintained at a constant temperature. The gas is then passed through a column of glass beads to remove any entrainment. The saturated gas then passes through a column packed with the 4A zeolite

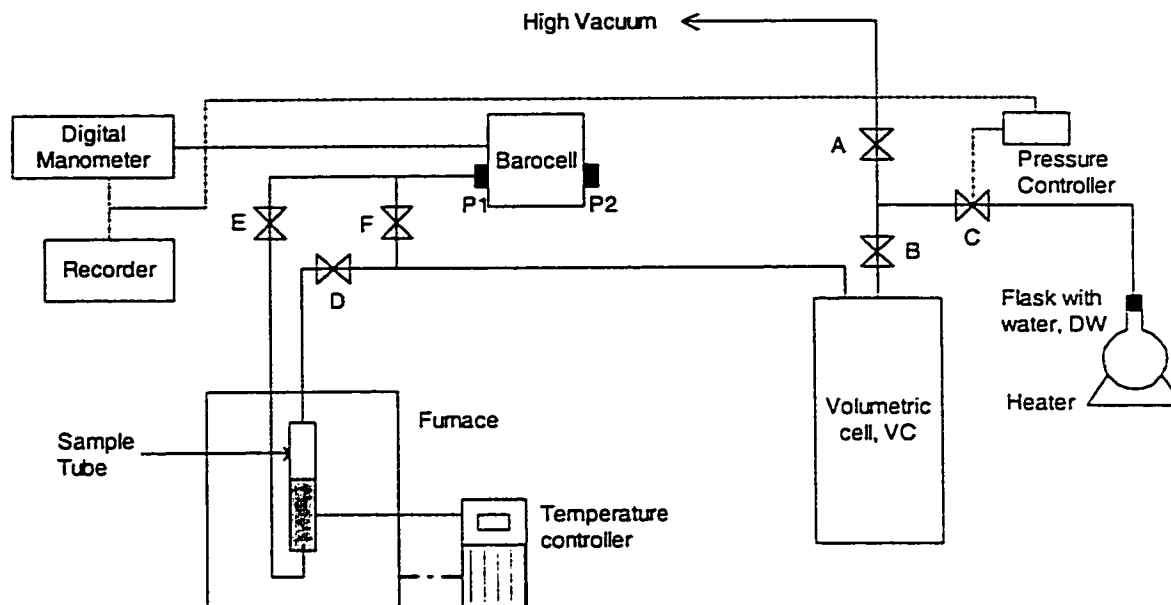


FIGURE 3-1 Schematic diagram of the constant volume apparatus used for generating isotherm data.

adsorbent pellets. The adsorption column is kept inside a furnace maintained at a constant temperature. The bubbler can be bypassed to let the dry helium pass through the column. The values of various experimental parameters is listed in Table 3-1.

3.3 Experimental Procedure

In this section we first discuss the experimental procedure for generating equilibrium sorption data and then the breakthrough curve measurement.

3.3.1 Equilibrium Sorption Studies

Initially, constant volume apparatus is at atmospheric pressure and isolated by closing valves E and F. Distilled water in flask DW is first deaerated for 4 hrs at 60 °C by opening valves A and C and closing valve B. After deaeration flask DW is isolated by closing valve C. Volumetric cell is then evacuated by slowly opening valve B. This

TABLE 3-1 Details of adsorption column

Parameter		Uetikon	TOSOH
A (cm ²)		0.8992	0.8992
L (cm)		15.9	14.1
ϵ_b (%)		0.5571	0.5530
ϵ_p (%)		35.7395	27.9773
\dot{V} (cc/min at NTP)		120	120
ρ_b (gm/cc)		0.5910	0.6665
m_{ads} (gm)		8.45	8.45
R_p (cm)		0.2125	0.2115
D_L (cm ² /sec)	175 °C	75.887	77.190
	200 °C	79.395	80.516
D_p (cm ² /sec)	175 °C	0.076	0.091
	200 °C	0.073	0.095

evacuation step continues until a constant base line is obtained on the recorder. A small sample (1.00 gm) of fresh 4A zeolite pellets is placed in a stainless steel tube and connected across valves E and D. Valve E is opened and valve F is closed in order to allow the measurement of pressure inside the sample tube. The sample tube is evacuated by slowly opening valve D to prevent the zeolite pellets from flying off. The sample temperature is slowly increased from ambient temperature to 350 °C in 2 hrs. The sample is regenerated at this temperature for 12 hrs at the end of which a constant base line is obtained.

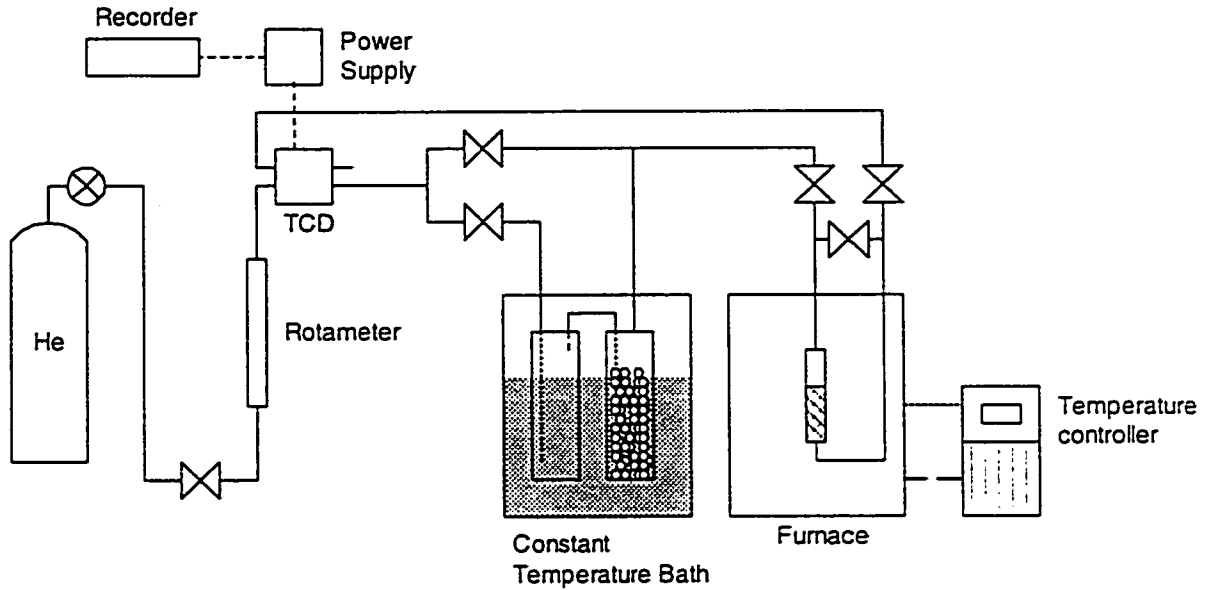


FIGURE 3-2 Schematic diagram of the experimental setup for the determination of the breakthrough curve.

At the end of regeneration step the sample is cooled to the desired temperature and isolated by closing valves E and D. Volumetric cell VC is also isolated by closing valve A and filled to a known pressure P_1^i of water vapor by setting the desired pressure on pressure controller. Control valve C is set to closed position after the pressure in volumetric cell has reached its steady state value. Water vapor is now adsorbed on the zeolite sample by opening valves E and D and closing valve F. The system is allowed to reach the steady state pressure P_1^f . The amount of water adsorbed, m_1 , on the zeolite sample in equilibrium with water vapor pressure P_1^f is calculated as:

$$m_1 = M_w \frac{(P_1^i - P_1^f) V_{cell}}{RT_a} \quad (3-25)$$

Here sample tube volume is neglected in comparison to cell volume, V_{cell} . Volumetric cell

is similarly filled to pressures $P_2^i, P_3^i, P_4^i \dots$ and the corresponding equilibrium pressures $P_2^f, P_3^f, P_4^f \dots$ are recorded. Mass of water adsorbed, m_{r+1} , in each step can be calculated as

$$m_{r+1} = \sum_1^r m_j + M_w \frac{(P_{r+1}^i - P_{r+1}^f) V_{cell}}{RT_a} \quad r = 1 \dots n \quad (3-26)$$

Experimental isotherm data is generated at 175 °C and 200 °C for Uetikon and TOSOH adsorbent pellets. Dry weight of zeolite sample is approximately 0.85 gm. The range of water vapor pressure that could be covered is limited by the vapor pressure of water at ambient temperature which is 30 mbar at 25 °C. Therefore, isotherm data is generated for water vapor pressure ranging from 0 to 20 mbar to avoid condensation in the system.

3.3.2 Breakthrough Curve Measurement

8.5 gm of fresh 4A zeolite adsorbent pellets is placed in a stainless steel tube of 1.07 cm diameter. Dry helium is passed through the adsorption column at around 120 cc/min. The column temperature is slowly raised from ambient temperature to 350 °C in 2 hrs. The sample is regenerated at this temperature for 12 hrs. A constant baseline is obtained at the end of the regeneration step. Cooling the column to ambient temperature and waiting for 6 hrs does not alter the baseline. Reheating the column to 350 °C also does not affect the baseline. This indicates that the moisture content present in the helium from the cylinder is negligible within the sensitivity level of the thermal conductivity detector used.

Adsorption is carried out at a constant temperature and constant inlet moisture concentration obtained by passing the dry helium through the bubbler maintained at 10 °C. Breakthrough curves were recorded at 175 °C, and 200 °C. The temperature of the two ends of the adsorption column differed by less than 2 °C. The carrier gas flow rate was approximately 120 cc/min. Carrier gas flow rate was manually controlled using metering valves. For a few runs in the beginning the flow rate was frequently monitored using the soap bubble flow meter. It was found that the flow fluctuations were less than 2 %. For subsequent runs flow rate was measured only in the beginning and end of the adsorption run and the actual flow rate was taken to be the average of these two. The average duration of one adsorption run is 6 hrs. The desorption breakthrough curve is recorded for upto 3 hrs after which the sample is regenerated again as described earlier.

3.4 Results and Discussion

In this section we first discuss the experimental determination of water-4A zeolite adsorption isotherm and then the breakthrough curve measurement.

3.4.1 Equilibrium Sorption Studies

The present study was carried out using commercial 4A zeolite pellets from TOSOH and Uetikon. Isotherm data was generated for water-4A zeolite system at 175 °C and 200 °C. Most of the experimental isotherm data was generated for Uetikon pellets because both Uetikon and TOSOH pellets showed identical adsorption capacity at several experimental points generated at 175 °C.

The tetrahedron arrangement in 4A zeolite crystals gives rise to α and β cages with 4.0 and 2.2 Å openings, respectively. Water has a kinetic diameter of approximately 2.5 Å and can enter both α and β cages. The volume of α and β cages is 775 and 155 Å³, respectively. It is therefore clear that in 4A zeolite there are two different types of adsorption sites for water molecules. Thus, the water-4A zeolite adsorption isotherm must be a dual site adsorption isotherm.

A dual site Freundlich Langmuir isotherm of the form

$$\frac{q_e}{q_s} = f_1 \frac{(k_1 p)^{n_1}}{1 + (k_1 p)^{n_1}} + (1 - f_1) \frac{(k_2 p)^{n_2}}{1 + (k_2 p)^{n_2}} \quad (3-27)$$

is fitted to the experimental data. First term in Eq. 3-27 represents the sorption in β cages and the second term represents the sorption in α cages. Parameter f_1 is the fraction of total sites in β cages. If we assume the number of sites to be proportional to the volume of cages then $f_1 = 0.1667$.

The monolayer saturation capacity of water on 4A zeolite crystals² is 0.27 gm/gm. In commercial adsorbent pellets approximately twenty weight percent binder is used for pelletization. Thus, the saturation capacity of 4A zeolite pellets without hydrothermal treatment will be approximately 0.216 gm/gm. However, hydrothermal treatment during the pelletization process leads to slight decrease in saturation capacity. Ruthven¹ has reported saturation capacity of water on three commercial 4A zeolite molecular sieves. The saturation capacity of these molecular sieves is found to be 0.20, 0.19, and

0.185 gm/gm. Smith⁸⁷ reported the saturation capacity of water on commercial 4A zeolite pellets as 0.20 gm/gm. Thus, the monolayer saturation capacity, q_s , is taken to be 0.20 gm/gm. Other parameters are obtained by fitting Eq. 3-27 to the experimental data using the nonlinear curve fitting subroutine `curvefit` in Matlab. The fitted value of n_2 is 1.50 with root mean square error equal to $3.4e-4$ at 175 °C and $3.7e-4$ at 200 °C. However, for a Langmuir-Freundlich isotherm n_2 should be less than one. Enough experimental data is not available in the high water vapor pressure range to accurately calculate the value of n_2 by fitting. An equally good fit can be obtained by setting $n_2 = 1.0$ with root mean square error equal to $5.0e-4$ at 175 °C and $4.2e-4$ at 200 °C. Values of other fitting parameters are listed in Table 3-2. A comparison of the experimental and fitted data is shown in Figures 3-3 and 3-4. Errors in prediction based upon 95 % confidence interval are also plotted in the figures.

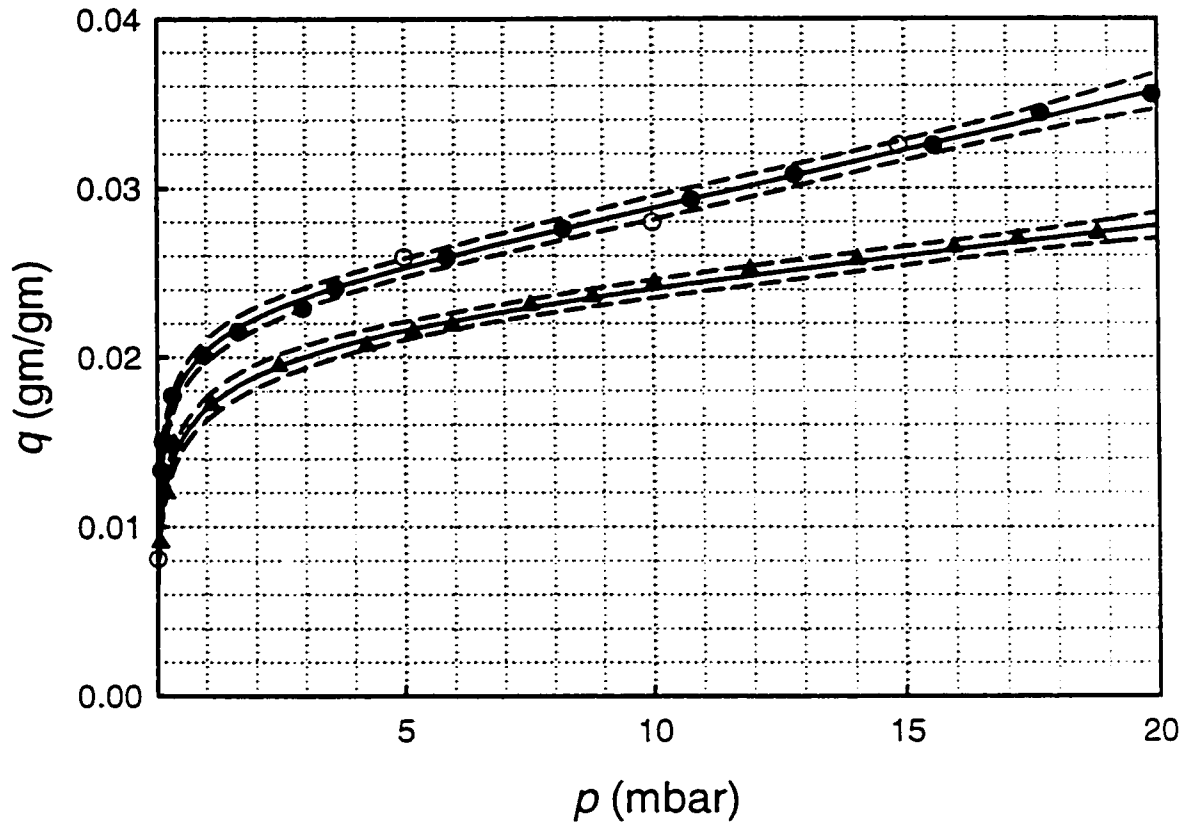


FIGURE 3-3 Experimental (symbols) and fitted (smooth lines) isotherms at 175 °C (●) and 200 °C (▲). Dashed lines are predictions in 95 % confidence interval for the corresponding theoretical isotherm. Open circles correspond to the experimental isotherm points for TOSOH pellets at 175 °C.

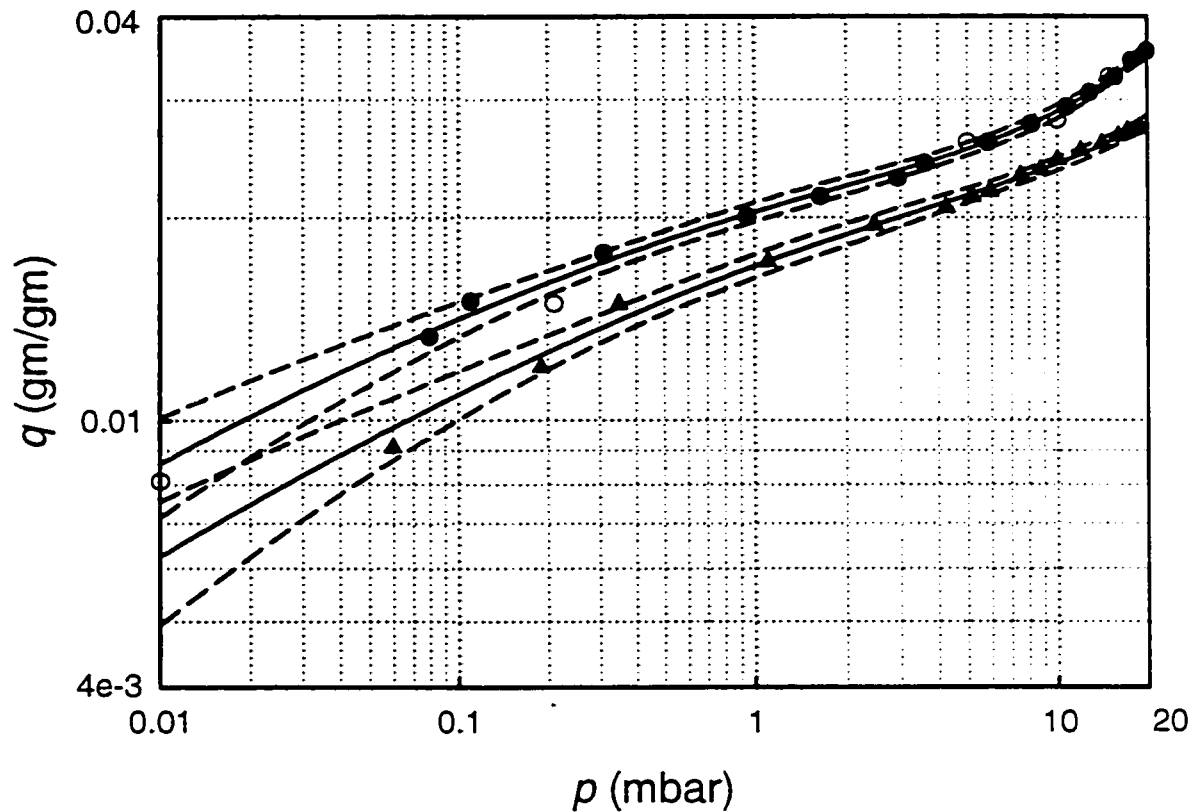


FIGURE 3-4 Experimental (symbols) and fitted (smooth lines) isotherms at 175 °C (●) and 200 °C (▲) on log-log scale. Dashed lines are predictions in 95 % confidence interval for the corresponding theoretical isotherm. Open circles correspond to the experimental isotherm points for TOSOH pellets at 175 °C.

3.4.2 Breakthrough Curve Measurement

Breakthrough curves were measured for both Uetikon and TOSOH pellets at 175 °C and 200 °C. Typical adsorption and desorption breakthrough curves for Uetikon and TOSOH pellets at 175 °C and 200 °C are shown in Figures 3-5 and 3-6.

TABLE 3-2 Isotherm parameters obtained by fitting experimental data for Uetikon pellets to the theoretical isotherm equation.

Parameter	Value
n1	0.2873
n2	1.0
k_1 (175 °C)	3.335 mbar ⁻¹
k_2 (175 °C)	0.0030 mbar ⁻¹
k_1 (200 °C)	0.9150 mbar ⁻¹
k_2 (200 °C)	0.0014 mbar ⁻¹

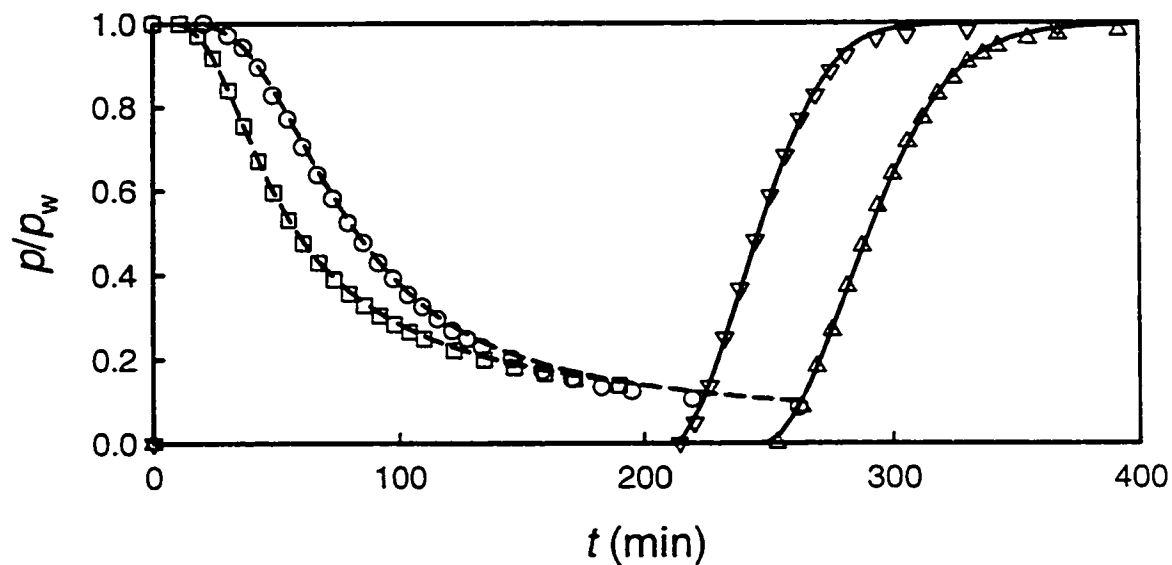


FIGURE 3-5 Adsorption and desorption breakthrough curves for Uetikon pellets at 175 °C and 200 °C. Symbols correspond to the experimental adsorption data at 175 °C (Δ), 200 °C (∇) and desorption data at 175 °C (\circ), and 200 °C (\square). Solid and dashed lines correspond to the fitted adsorption and predicted desorption breakthrough curves respectively.

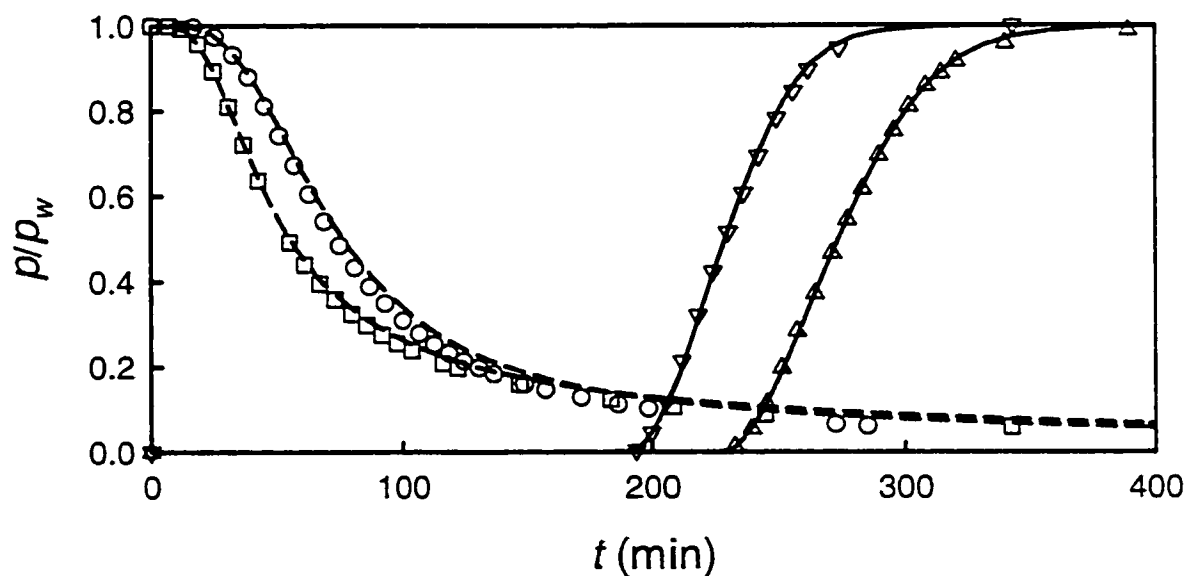


FIGURE 3-6 Adsorption and desorption breakthrough curves for TOSOH pellets at 175 °C and 200 °C. Symbols correspond to the experimental adsorption data at 175 °C (Δ), 200 °C (∇) and desorption data at 175 °C (\circ), and 200 °C (\square). Solid and dashed lines correspond to the fitted adsorption and predicted desorption breakthrough curves respectively.

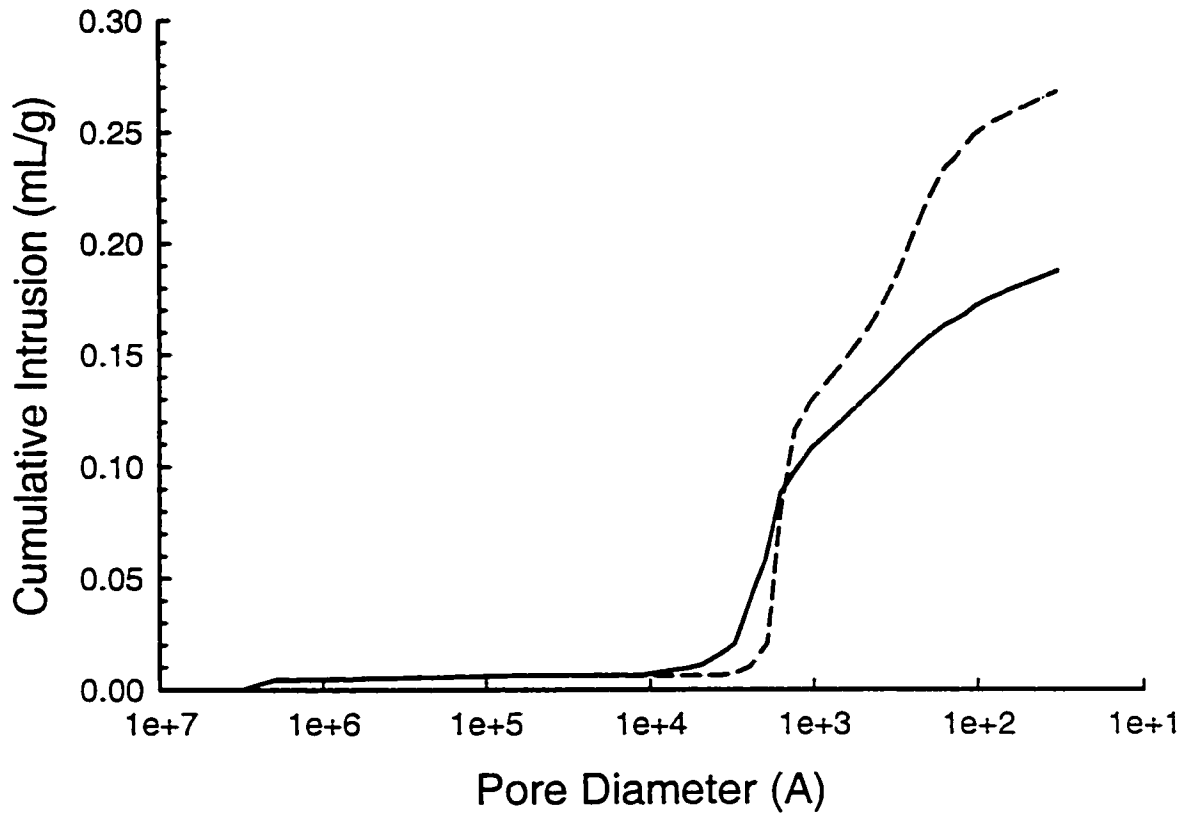


FIGURE 3-7 Cumulative pore size distribution of TOSOH (solid line) and Uetikon (dashed line) pellets.

3.4.2.1 Pore Size Distribution

Mass transfer regime in the macropores can be either purely molecular diffusion or Knudsen diffusion or a combination of both depending upon the macropore pore size distribution of the pellet. Pore size distribution for both TOSOH and Uetikon pellets was determined using the mercury porosimeter. Cumulative pore size distribution for both TOSOH and Uetikon pellets is shown in Figure 3-7. Intrusion data summary is given in Table 3-3.

TABLE 3-3 Intrusion data obtained by mercury porosimetry

Property	TOSOH	Uetikon
Median pore diameter (Å) (volume)	1267	798
Total intrusion volume (mL/g)	0.1876	0.2678
Bulk density (g/mL)	1.4911	1.3344
Skeletal density (g/mL)	2.0703	2.0766
Porosity (%)	27.9773	35.7395

3.4.2.2 Particle Size Distribution

Macropore time constant τ_{mac} is directly proportional to R_p^2 , the particle radius. Particle size distribution for both TOSOH and Uetikon pellets is measured by taking a random sample of 100 pellets each, and measuring the diameter with a micrometer accurate to 0.005 cm. The distribution for original pellets was found to be very wide therefore, a narrower cut from 4.00 to 4.75 mm was obtained by sieving. The particle size distributions for both TOSOH and Uetikon pellets are shown in Figure 3-8. Its clear from the figure that TOSOH pellets have a relatively narrow particle size distribution in comparison to Uetikon pellets. Average particle diameters of TOSOH and Uetikon pellets are 4.23 and 4.25 mm, respectively.

3.4.2.3 Parameter Estimation

The experimental adsorption breakthrough curves obtained as described in the previous section are fitted to the theoretical ones to determine the unknown parameters τ_{pm} , and pellet tortuosity τ . All the other parameters can be calculated a priori. Since, the flow rate

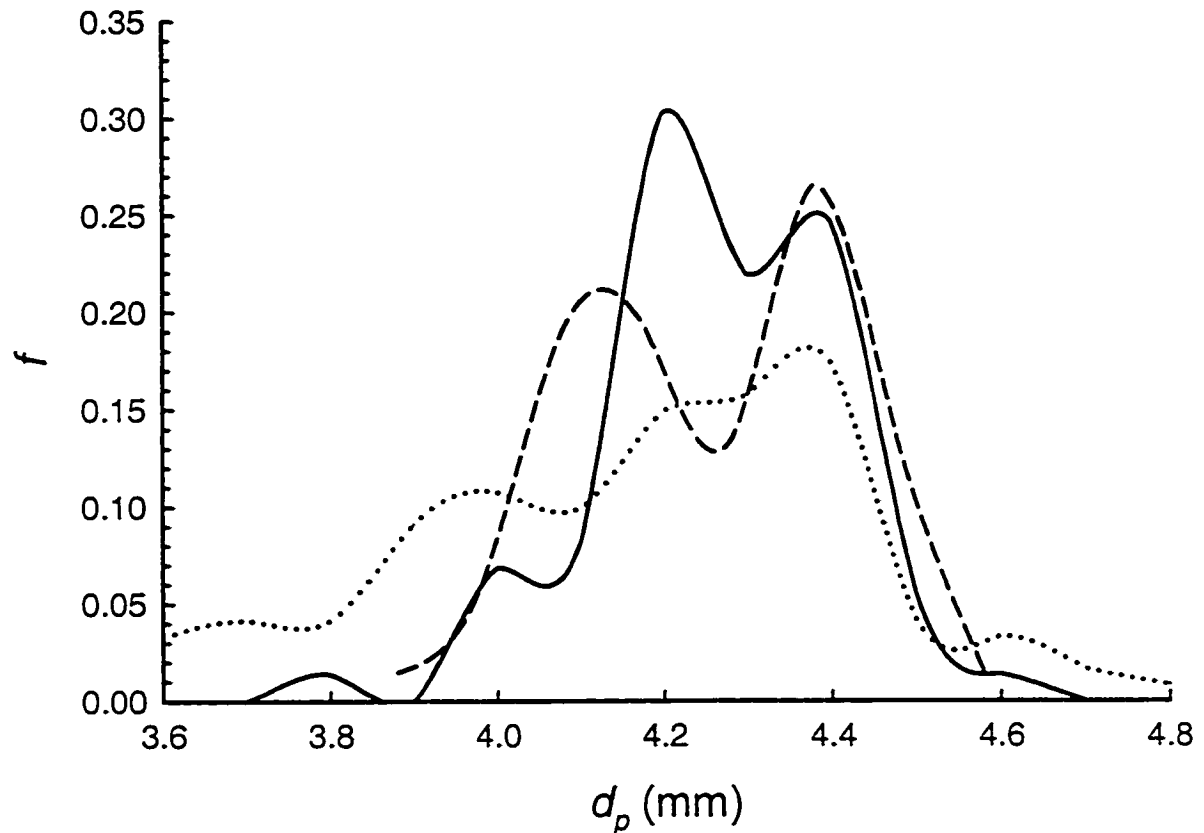


FIGURE 3-8 Particle size distribution of TOSOH (solid line) and Uetikon (dashed line) pellets. f is the number fraction of particles and d_p is the pellet diameter. Dotted line corresponds to particle size distribution of a sample of TOSOH pellets as supplied by the manufacturer. Solid and dashed lines are obtained after sieving the original TOSOH and Uetikon samples.

of carrier gas through the bubbler is very high (120 cc/min) it was suspected that the carrier gas coming from the bubbler will not be saturated. Therefore, the partial pressure of water vapor in the carrier gas needs to be calculated. This is done by simultaneously solving the material balance equation obtained by integrating the experimental breakthrough curve and the equilibrium isotherm equation to solve for the amount of water adsorbed and the corresponding water vapor partial pressure.

Mass of water adsorbed per unit mass of adsorbent in the adsorption column can be calculated as

$$q = \frac{\dot{V}M_w p_w (t_{max} - A)}{RT_a w_a} \quad (3-28)$$

where t_{max} is the time at which outlet partial pressure of water vapor approaches the inlet partial pressure of water vapor and A is the area under the breakthrough curve and can be calculated as

$$A = \int_0^{t_{max}} \frac{P}{P_w} dt \quad (3-29)$$

Equations 3-27 and 3-28 can be solved simultaneously to give q and p_w . However, due to the uncertainties involved in the experimental isotherm only ranges of these two quantities can be estimated. The graphical procedure for estimating range of p_w is shown in Figure 3-9. As shown in the figure, p_w is bounded in the interval [8.2-10.2] in 95 % confidence interval. The exact value of p_w is also determined by fitting the theoretical breakthrough curves to experimental ones.

For fresh Uetikon and TOSOH adsorbent samples τ_{pm} , τ , and p_w are the optimized or fitting parameters and λ , Pe , β_b , β_p , τ_{mac} , and τ_{con} are the fixed or calculated parameters. The values of fitting parameters are obtained by minimizing the average least square error between the theoretical adsorption breakthrough curve and the experimental adsorption curve. Matlab subroutine `fmins` in optimization toolbox has been used for fitting the data. This subroutine uses the Nelder-Mead simplex algorithm to search for a local minimizer in the neighborhood of an initial guess. The average computation time for each fitting run is approximately 7.5 hrs on a Compaq P4 (2 GHz) PC.

3.4.2.4 Effect of Dead Volume

Effect of the dead volume of the system on breakthrough curves was estimated by measuring the system's response to a step change in inlet concentration. The breakthrough curve for an empty adsorption column was obtained. The breakthrough time for the empty adsorption column was less than 15 seconds and the outlet concentration approached the inlet concentration in less than 1 min. Therefore, total response time for an empty adsorption column is negligible in comparison to the response time of adsorption column filled with adsorbent where the breakthrough time is of the order of 3-4 hrs. Thus, the effect of dead volume of the system is neglected in all the breakthrough curve measurement runs.

Values of various fitting parameters for fresh 4A zeolite samples are listed in Table 3-4. All the values are obtained by fitting the experimental adsorption breakthrough curves to the theoretical curves. Only first 95 % of the breakthrough curve is used for fitting to avoid reading off errors and effects of particle size distribution. All the other parameters required to calculate the theoretical breakthrough curves are listed in Table 3-5.

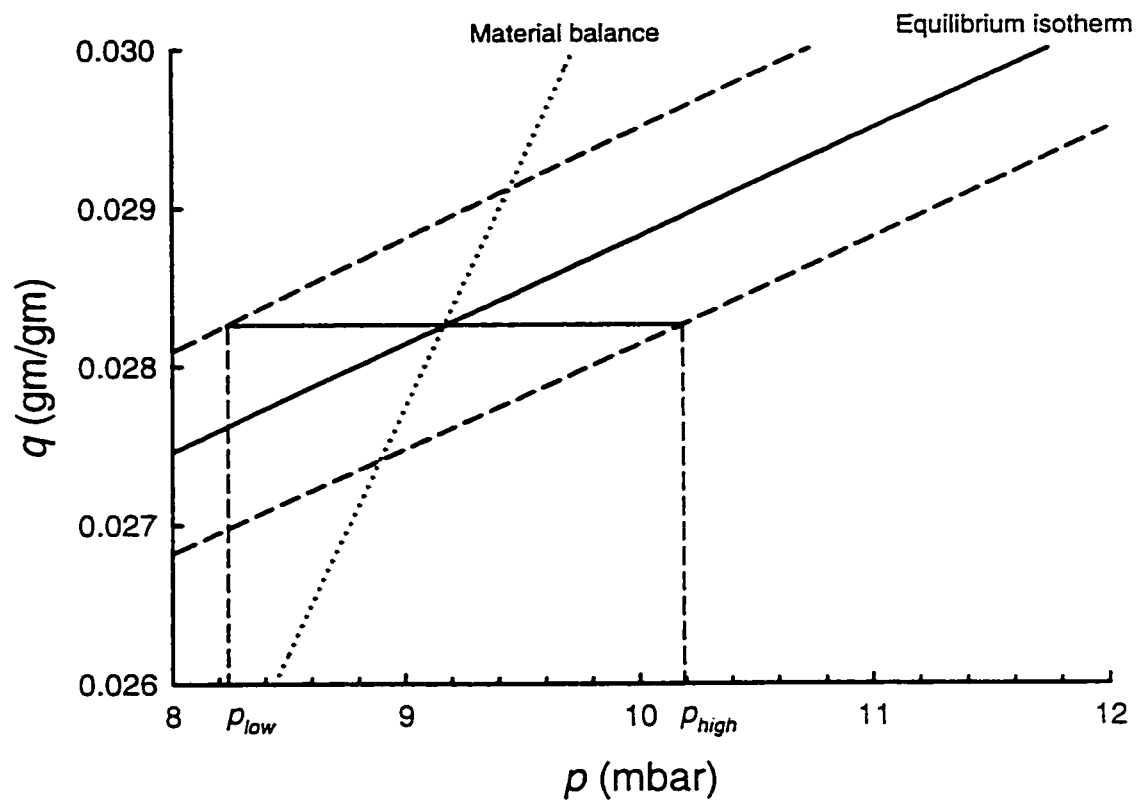


FIGURE 3-9 Graphical procedure for the estimation of p_w . Material balance line is given by Eq. 3-28. Dashed lines correspond to 95 % confidence interval for equilibrium isotherm predictions.

TABLE 3-4 Values of fitting parameters for the fresh 4A zeolite pellets.

Run	Sample	Temperature	τ_{pm} (min)	τ	p_w (mbar)
1	Uetikon	175 °C	8.15	4.06	9.38
2	Uetikon	200 °C	5.27	4.42	9.34
3	TOSOH	175 °C	7.84	4.84	9.95
4	TOSOH	200 °C	6.85	4.90	10.05

TABLE 3-5 Values of parameters used to calculate theoretical breakthrough curves.

Run	λ	Pe	β_b	β_p	τ_{mac} (min)	τ_{con} (min)
1	0.1426	74.80	1.53e-4	4.26e-5	232.00	292.02
2	0.1189	74.80	1.72e-4	4.81e-5	213.40	246.99
3	0.1446	67.12	1.41e-4	3.12e-5	263.07	276.09
4	0.1205	67.12	1.62e-4	3.58e-5	219.62	230.47

A comparison of fitted and experimental breakthrough curves is shown in Figure 3-5 for Uetikon pellets and in Figure 3-6 for TOSOH pellets. It can be seen that the fit for adsorption breakthrough curves is excellent. The value of p_w as shown in Table 3-4 is well within the 95 % confidence limit. The tortuosity of pellet slightly increases with an increase in temperature. This is probably because the kinetic energy of molecules increases with the temperature and the effect of pore size structure is felt more strongly at high molecular velocity. In each case the tortuosity factor is within the range 2-6 as reported in literature¹.

The value of pore mouth time constant, τ_{pm} , is much smaller than both macropore time constant and the convection time constant. Therefore, it is a reasonable assumption to neglect the pore mouth resistance in the fresh 4A zeolite adsorbent pellets. The pore mouth time constant decreases with an increase in temperature because at high temperature more molecules will have sufficient energy to jump across the pore openings.

It can be seen from Table 3-5 that the value of λ or percent saturation is always less than 15 %. At this low coverage large asymmetry between the adsorption and desorption breakthrough curves cannot be explained by a single site adsorption isotherm. Based upon the difference in shapes of adsorption and desorption breakthrough curves we can conclude that the adsorption isotherm is highly favorable for adsorption and thus unfavorable for desorption.

Area above the adsorption breakthrough curve is directly proportional to the mass of

water adsorbed on the adsorbent during the adsorption step. Mass of water removed during the desorption step is proportional to the area underneath the desorption breakthrough curve. Therefore, for the similar experimental conditions the areas above the adsorption breakthrough curve and that underneath the desorption breakthrough curves should be equal. However, in the present study adsorption isotherm is highly unfavorable for desorption leading to a very long tail in desorption breakthrough curves. Therefore, within the recording time for desorption curves, desorption did not approach completion leading to a considerable amount of residual moisture in the adsorption column. This was confirmed by ramping up the temperature from 175 °C (or 200 °C) to 350 °C in steps of 25 °C and recording the peaks at each temperature.

The values of fitted parameters, obtained by fitting the adsorption breakthrough curves, are used to calculate desorption breakthrough curves. It is found that there are large differences between the experimental and theoretical desorption breakthrough curves. However, as the pore mouth time constant is decreased agreement between the experimental and theoretical desorption curves becomes better. A comparison between the experimental and theoretical desorption breakthrough curves is shown in Figures 3-5 and 3-6. The theoretical desorption curves are obtained assuming that there is no pore mouth resistance or $\tau_{pm} \rightarrow 0$. It is found that generally the predictions are good for $p/p_w > 0.20$. Lower part ($p/p_w < 0.20$) of the experimental desorption curve always lies below the theoretical curve. This part of the curve is found to be very insensitive to changes in kinetic parameters like τ_{pm} , τ_{mac} , Pe etc. and sensitive to equilibrium isotherm parameters. Therefore, the differences between the experimental and theoretical

desorption breakthrough curves can be attributed to the errors associated with determination of isotherm parameters.

The adsorption and desorption breakthrough curves are mirror images for a linear isotherm i.e. small values of λ (< 0.15)¹⁰⁻²³. The asymmetry between the adsorption and desorption breakthrough curves increases as the nonlinearity of the adsorption isotherm is increased³⁻⁹. For an irreversible isotherm, which is an extreme case of the nonlinearity for a single site isotherm, the degree of asymmetry between the adsorption and desorption is the largest²⁴. The irreversible isotherm is an idealization for strongly adsorbed species and is widely used for modeling the adsorption of water on 4A zeolite^{4,82}. In the present study a high degree of asymmetry is observed even though the value of λ is always less than 0.15. At this low coverage large asymmetry between the adsorption and desorption breakthrough curves cannot be explained by a single site adsorption isotherm. However, the dual site Freundlich-Langmuir isotherm can satisfactorily explain the observed asymmetry between the adsorption and desorption breakthrough curves.

3.5 Conclusions

Based on the discussion presented in the preceding section following can be concluded

1. water-4A zeolite (TOSOH and Uetikon) adsorption isotherm can be satisfactorily represented by Langmuir-Freundlich dual site adsorption isotherm.
2. The asymmetry between the experimental adsorption and desorption breakthrough curves cannot be explained using a single site adsorption isotherm equation.

3. Theoretical adsorption breakthrough curves can be fitted to the experimental ones to obtain the pore mouth time constant which is very small for the case of fresh 4A zeolite pellets.

4

DEACTIVATION MODELING OF 4A ZEOLITE ADSORBENTS

Thermal swing adsorption is probably the most common system for drying of gases. Since, temperature is a more effective variable than pressure for changing the thermodynamic potential¹, thermal swing processes are generally preferred for strongly adsorbed species such as water on 4A or alumina. However, repeated thermal cycling in presence of moisture can lead to deactivation of the zeolite adsorbent due to dealumination and exposure to elevated temperature in presence of reactive hydrocarbons during the desorption cycle can lead to coke formation in the adsorbent.

There have been a number of experimental studies which demonstrate that the adsorbents tend to deactivate under severe hydrothermal conditions^{1, 58, 60, 61, 62, 63, 64, 65}. These studies are performed using the uptake rate measurement technique. Some of these studies indicate that the pore mouth resistance increases as a result of deactivation while others indicate that the micropore diffusivity decreases with increasing hydrothermal severity. NMR studies on severe hydrothermal dehydration of 5A zeolite give a clear evidence of the development of pore mouth resistance^{66, 67, 68} which increases with increasing severity of hydrothermal treatment⁶⁹. These studies indicate that micropore

diffusivity remains almost a constant. These results are supplemented by X-ray photoelectron spectroscopy studies which reveal a decrease in the Al/Si ratio at the crystal surface resulting in a narrowing of the pore mouth⁷¹.

Available literature on deactivation of adsorbents provides strong evidence in favor of the deactivation due to increase in pore mouth resistance by preferential dealumination of the pore openings. However, almost none of the studies indicate any loss in adsorption capacity as a result of deactivation. No model has been developed to predict the extent of deactivation as a function of hydrothermal conditions or as a function of exposure time.

In the present study experimental deactivation runs are carried out in a batch system for 4A zeolite adsorbents obtained from two manufacturers, viz., TOSOH and Uetikon.

4.1 NMR for Deactivation Studies

NMR techniques have been very widely used for measuring the intracrystalline diffusivities and presence of surface barrier or pore mouth resistance in many zeolitic systems. NMR studies on severe hydrothermal dehydration of 5A zeolite, with methane as the probe molecule, give a clear evidence of the development of a pore mouth resistance^{66, 67, 68}. The magnitude of the pore mouth resistance increases with increasing severity of hydrothermal treatment whereas the micropore diffusivity remains almost a constant⁶⁹. This effect has been confirmed using several different probe molecules⁷⁰. The NMR results are supplemented by X-ray photoelectron spectroscopy studies which reveal a decrease in the Al/Si ratio at the crystal surface resulting in a narrowing of the pore mouth⁷¹.

The mass transfer properties of a commercial 5A adsorbent, used in a petroleum refinery, have been investigated, as a function of the time on stream, using the NMR technique^{69, 74}. The results indicate a continuous increase in pore mouth resistance with very little change in micropore diffusivity. It seems clear that the slow buildup of carbonaceous deposits leads to the observed increase in pore mouth resistance.

All the studies discussed above deal with the hydrocarbons and use custom built NMR apparatus. Recently, a study has been reported in which diffusion of water has been studied in NaCaA zeolite samples with varying Ca content⁸⁸. In the present study, an attempt has been made to study the diffusion of water in 4A zeolite using NMR technique. Various samples of water adsorbed on 4A zeolite had been prepared at low water loadings. However, no signal could be detected using the standard NMR apparatus available in the chemistry department. It was postulated that this is due to formation of a highly immobilized structure of water in the 4A zeolite micropores. Kärger et. al.⁷⁰ have used a home built NMR equipment (FEGRIS) for the deactivation studies thus, the use of NMR technique to measure the pore mouth resistance would require the use of a custom built NMR apparatus.

4.2 Nuclear Microscopy for Dealumination Studies

The 3 MV Tandatron accelerator at King Fahd University of Petroleum & Minerals, Dhahran has been used extensively for the applications of sensitive and non-destructive nuclear techniques in a wide variety of materials including petrochemical catalysts. This technique can be used in a wide variety of applications involving fresh and spent

catalysts. The technique is found to be useful in determining agglomeration or sintering of active metals on the catalyst supports as well as trace element impurities. Such data are not obtainable by conventional techniques.

Nuclear analytical techniques are among the few highly sensitive techniques which allow simultaneous determination of elemental concentrations and their distribution profiles at parts per million levels in a sample non-destructively. In particular, Proton Induced X-ray Emission (PIXE) technique has been used in a wide variety of fields for rapid, multielement analysis. In this technique, energetic protons from an accelerator are allowed to strike a sample which then produce characteristic X-rays from the elements present in the sample. By measuring the energies and the intensities of these characteristic X-rays, one can identify and quantify the concentrations of the elements producing the X-rays. The Micro-PIXE technique, as it is called when the PIXE technique is used with a focussed proton beam of micrometer dimension, allows scanning of a sample with micrometer spatial resolution to check for uniformity of elemental distribution profiles.

The micro-PIXE analytical technique is available in the Tandetron accelerator laboratory at the Center for Applied Physical Sciences (formerly Energy Research Lab) of the Research Institute, King Fahd University of Petroleum & Minerals, Dhahran (KFUPM). This nuclear technique has been successfully applied in a wide variety of fields such as materials science⁸⁹, superconductivity⁹⁰, geology⁹¹ and in catalyst analysis⁹²,⁹³,⁹⁴,⁹⁵,⁹⁶. In particular, nuclear microscopy can be used to quantify the aluminum concentration and its distribution in 4A zeolite samples. Therefore, this technique is a

direct way of determining whether the deactivation of 4A zeolite samples is due to preferential dealumination of pore mouths. However, unfortunately the Tandetron accelerator in CAPS/RI is currently out of order and due to time constraints these studies could not be performed. However, the deactivated samples have been retained and labeled for future investigations when the Tandetron accelerator is operable.

4.3 Experimental Apparatus

Deactivation runs are carried out by exposing a regenerated 4A zeolite sample to a known concentration of water vapor and temperature for a known duration of time. The constant volume apparatus (presented in Figure 3-1) is slightly modified for regenerating and saturating the zeolite sample to a known moisture concentration. In the present study a twenty centimeter long column is used as against seven centimeter column used for isotherm measurement in chapter three.

The schematic diagram of the experimental apparatus used for deactivation studies is shown in Figure 4-1. A twenty centimeter long and 1.07 cm diameter sample tube made of stainless steel is sealed at its ends with the aid of two valves as shown in the figure. The tube is placed inside a furnace with a temperature controller. The valves and other fittings which were protruding out of the furnace were well insulated. A new sample tube with new fittings and valves was used for each run.

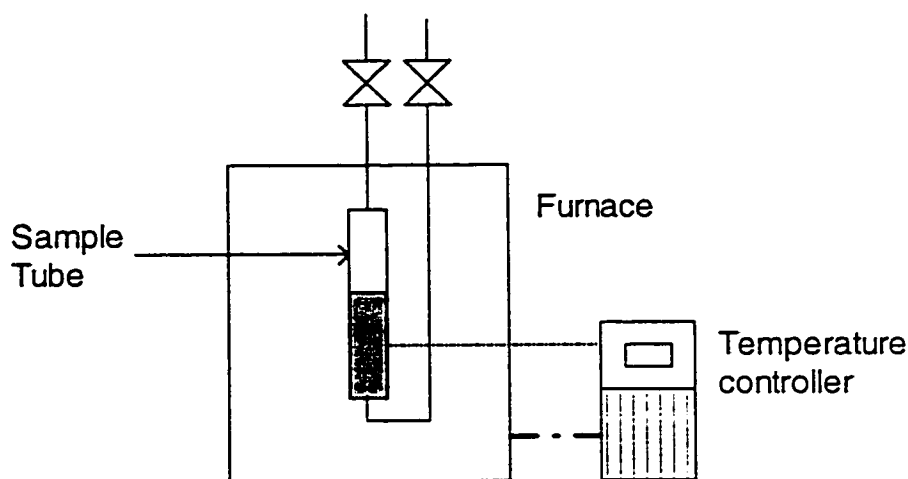


FIGURE 4-1 Schematic diagram of the apparatus used for deactivating the zeolite samples.

4.4 Experimental Procedure

Approximately ten grams of fresh 4A zeolite sample was placed inside a column, the column was then connected to constant volume apparatus and slowly evacuated to a vacuum better than 10^{-6} mbar. The sample temperature was then slowly raised from ambient to 350 °C in approximately 2 hrs. The sample was allowed to regenerate at this temperature for about twelve hours at the end of which a constant base line was obtained on the recorder. At the end of regeneration, the sample was brought to the desired temperature and saturated to a known pressure of water vapor by appropriately setting the desired pressure value 21 mbar on the pressure controller and adding the water from the distilled water flask. Two temperature settings, viz. 100 °C and 200 °C were used to give two moisture concentration levels. The saturation step takes upto 10 hrs after which the column is sealed and transferred to the deactivation apparatus. The column was brought to the desired deactivation temperature and allowed to deactivate for a known duration. Two deactivation temperature settings, viz. 350 °C and 400 °C have been used. The exact

duration of each deactivation run was recorded. Three deactivated samples each for Uetikon and TOSOH 4A zeolite pellets were prepared at each of the deactivation temperature and moisture concentration levels.

The deactivated samples were analyzed by measuring the adsorption and desorption breakthrough curves at 175 °C and 200 °C. The isothermality in the breakthrough curve measurement experiments was confirmed as described in chapter 3. A six letter alphanumeric coding of the form $A_1A_2A_3A_4A_5A_6$ was assigned to each of the breakthrough curves to uniquely identify the run conditions. The meaning of each of the letters is explained in Table 4-1.

TABLE 4-1 Six letter coding system for the experimental breakthrough curves.

Letter	Run Parameter	Parameter Value	Value
A ₁	Deactivation temperature	350 °C	L
		400 °C	H
A ₂	Moisture concentration level	Low (0.05 gm/gm)	L
		High (0.16 gm/gm)	H
A ₃	Pellet manufacturer	Uetikon	U
		TOSOH	T
A ₄	Duration of deactivation	Fresh	F
		approximately 100 hrs	1
		approximately 200 hrs	2
		approximately 300 hrs	3
A ₅	Breakthrough curve temperature	175 °C	L
		200 °C	H
A ₆	Breakthrough curve type	Adsorption	A
		Desorption	D

4.5 Results and Discussion

Adsorption and desorption breakthrough curves for all the deactivated Uetikon and TOSOH 4A zeolite samples are plotted in Figures 4-2 through 4-17. All the plots are grouped according to the pellet manufacturer, deactivation conditions and breakthrough curve temperature as discussed in the previous section. For example, experimental and theoretical breakthrough curves obtained at 175 °C and 200 °C for Uetikon pellets deactivated at high moisture concentration and 400 °C are plotted in Figures 4-2 and 4-3, respectively. It can be seen from the figures that in general, the adsorption breakthrough curves tend to become more dispersive leading to an early breakthrough with an increasing deactivation time. The desorption breakthrough curves do not change as a result of deactivation indicating that the deactivation does not have a significant effect on desorption. It can be seen by comparing Figures 4-2 and 4-3 that both adsorption and desorption breakthrough curves show an early breakthrough as a result of decrease in sorption capacity at high temperature.

The partial pressure of water vapor in the carrier gas fluctuated by approximately five percent variation from the average value. These pressure variations may contribute to the spread in both adsorption and desorption breakthrough curves. Therefore, the exact cause of observed differences needs to be established by fitting the experimental breakthrough curves to theoretical ones to calculate the kinetic parameters. However, some general observations can be made which are discussed in the following paragraphs.

The breakthrough curves at 175 °C and 200 °C for Uetikon pellets deactivated at

400 °C and low moisture concentration are plotted in Figures 4-4 and 4-5, respectively. It can be seen by comparing the Figures 4-2 and 4-4 that the spread of adsorption breakthrough curves is narrower in Figure 4-4 indicating a relatively less degree of deactivation at these deactivation conditions. Similar conclusion can be drawn by comparing the Figures 4-3 and 4-5. It can also be seen that the dispersive behavior also changes as the samples are deactivated.

The breakthrough curves at 175 °C and 200 °C for Uetikon pellets deactivated at 350 °C and high moisture concentration are plotted in Figures 4-6 and 4-7, respectively. It can be seen by comparing Figures 4-2, 4-4, and 4-6 that the spread of desorption breakthrough curves is widest in Figure 4-6 indicating that the effect of water vapor partial pressure variations are highly significant for this case. Besides deactivation, these water vapor partial pressure fluctuations also contribute to spread in adsorption breakthrough curves observed in these figures. It can be concluded that the spread in adsorption breakthrough curves in Figure 4-6 is greater than the spread in Figure 4-4. This indicates that high moisture concentration is relatively more significant parameter than the temperature for deactivation.

The breakthrough curves at 175 °C and 200 °C for Uetikon pellets deactivated at 350 °C and low moisture concentration are plotted in Figures 4-8 and 4-9, respectively. It can be seen that among Figures 4-2, 4-4, 4-6, and 4-8 the spread of adsorption breakthrough curves is the narrowest in Figure 4-8 indicating that the combination of low deactivation temperature with a low moisture concentration leads to a low degree of deactivation.

The adsorption and desorption breakthrough curves for fresh and deactivated TOSOH zeolite samples are plotted in Figures 4-10 through 4-17. It can be seen that in general the adsorption breakthrough curves are more dispersive for deactivated sample than that for the fresh sample. A comparison of adsorption breakthrough curves plotted in Figures 4-10, 4-12, 4-14, and 4-16 reveals that the spread in adsorption breakthrough curves decreases in the order of Figures 4-10 > 4-14 > 4-12 > 4-17. This indicates that a combination of high deactivation temperature and a high moisture concentration leads to the highest degree of deactivation and a combination of low deactivation temperature and a low moisture concentration leads to the lowest degree of deactivation. Among the two intermediate deactivation conditions one with the high moisture concentration (Figure 4-14) leads to a higher degree of deactivation. Similar conclusions can be drawn by comparing the breakthrough curves at 200 °C plotted in Figures 4-11, 4-13, 4-15, 4-17. These conclusions are consistent with observations made for Uetikon pellets. Furthermore, a comparison of plots obtained for Uetikon pellets and those obtained for TOSOH pellet indicate that at the same deactivation conditions the spread in adsorption breakthrough curves for TOSOH pellets is more than that for Uetikon pellets indicating a faster rate of deactivation for TOSOH pellets.

The methodology used for fitting the experimental breakthrough curves to theoretical ones is described in the previous chapter. It is assumed that tortuosity, τ , is not affected as a result of deactivation and is therefore taken to be same as that of a fresh 4A zeolite sample listed in Table 3-4. We also assume that the adsorption isotherm does not change as a result of deactivation.

There are only two fitting parameters, viz. pore mouth time constant, τ_{pm} , and the partial pressure of water vapor, p_w . These parameters are obtained by fitting the experimental adsorption breakthrough curves. Values of fitting parameters for various runs are listed in Table 4-2. Since, the value of inlet water vapor pressure p_w is well within the 95 % confidence limits described in chapter 3, we conclude that the adsorption capacity has not changed as a result of deactivation. In general, agreement between the experimental and theoretical adsorption breakthrough curves is excellent. The desorption breakthrough curves could be accurately predicted with $\tau_{pm} \rightarrow 0$ indicating that the pore mouth resistance is not significant during desorption. A comparison of experimental and fitted adsorption and predicted desorption curves is shown in Figures 4-2 through 4-17.

TABLE 4-2 Values of fitting parameters obtained by fitting the experimental adsorption curves to theoretical ones.

Run	A ₅			
	L		H	
	τ_{pm} (min)	p_w (mbar)	τ_{pm} (min)	p_w (mbar)
HHUFA ₅ A	8.15	9.38	5.27	9.34
HHU1A ₅ A	18.39	9.61	15.27	9.36
HHU2A ₅ A	26.45	9.54	15.29	9.66
HHU3A ₅ A	22.75	9.38	15.06	9.60
LHU1A ₅ A	17.44	9.45	12.37	9.28
LHU2A ₅ A	18.35	10.17	12.12	10.08
LHU3A ₅ A	17.57	10.19	13.99	9.8
HLU1A ₅ A	11.20	10.03	7.46	9.62
HLU2A ₅ A	13.67	9.47	8.95	10.04
HLU3A ₅ A	12.69	10.10	8.38	9.77
LLU1A ₅ A	9.36	9.47	6.11	9.31
LLU2A ₅ A	9.97	9.51	6.41	9.45
LLU3A ₅ A	10.08	9.57	6.57	9.50
HHTFA ₅ A	8.06	9.58	7.22	9.42
HHT1A ₅ A	26.44	9.68	22.34	9.54
HHT2A ₅ A	31.00	9.66	26.57	9.48
HHT3A ₅ A	33.46	9.63	36.31	9.55
LHT1A ₅ A	22.71	9.49	18.57	9.31
LHT2A ₅ A	31.40	9.46	24.72	9.62
LHT3A ₅ A	30.28	9.68	25.22	9.54
HLT1A ₅ A	19.63	9.39	15.40	9.60
HLT2A ₅ A	22.11	9.67	16.78	9.68
HLT3A ₅ A	26.44	9.37	20.87	9.67
LLT1A ₅ A	13.79	9.66	12.20	9.48
LLT2A ₅ A	18.40	9.67	16.34	9.48
LLT3A ₅ A	17.98	9.63	15.51	9.55

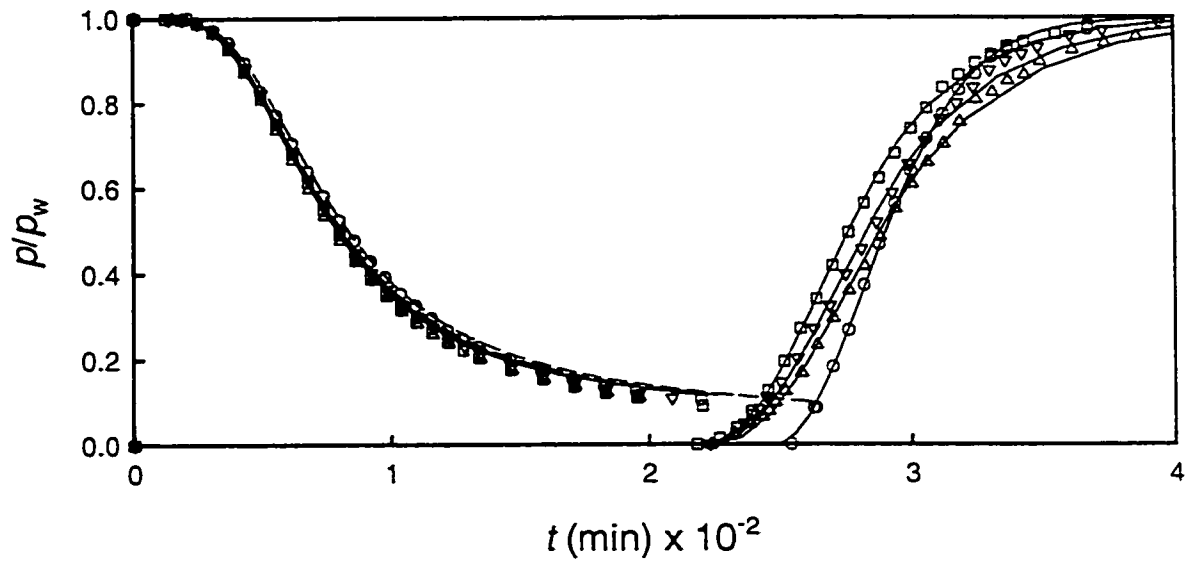


FIGURE 4-2 Experimental (symbols) and fitted adsorption (solid line) and desorption (dashed line) breakthrough curves for HHUFL (○), HHU1L (□), HHU2L (△), and HHU3L (▽).

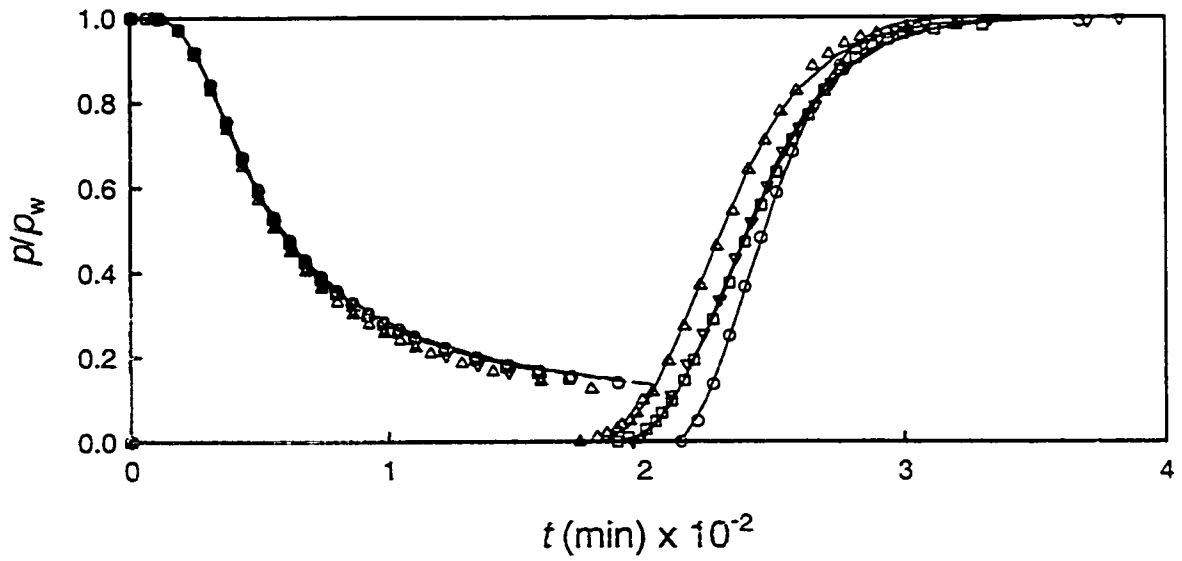


FIGURE 4-3 Experimental (symbols) and fitted adsorption (solid line) and desorption (dashed line) breakthrough curves for HHUFH (○), HHU1H (□), HHU2H (△), and HHU3H (▽).

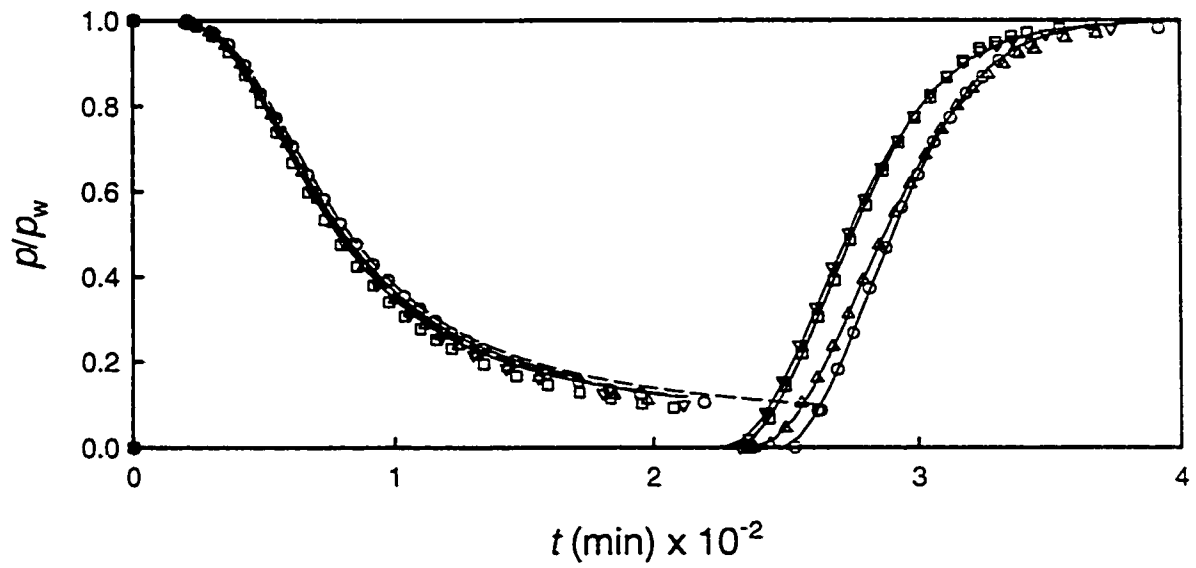


FIGURE 4-4 Experimental (symbols) and fitted adsorption (solid line) and desorption (dashed line) breakthrough curves for HLUFL (O), HLU1L (□), HLU2L (Δ), and HLU3L (▽).

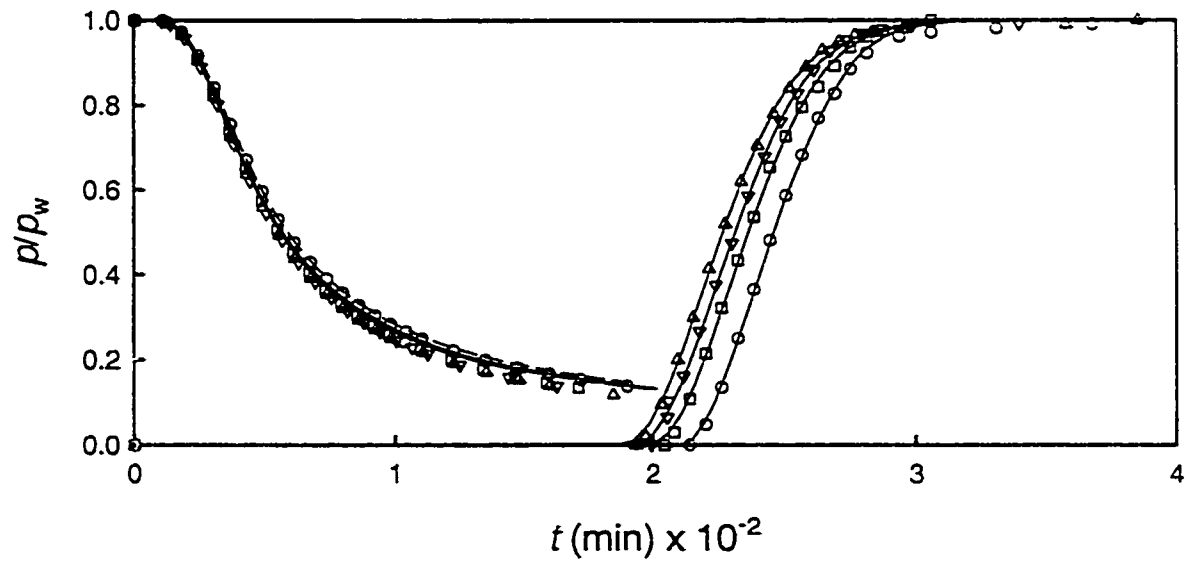


FIGURE 4-5 Experimental (symbols) and fitted adsorption (solid line) and desorption (dashed line) breakthrough curves for HLUFH (O), HLU1H (□), HLU2H (Δ), and HLU3H (▽).

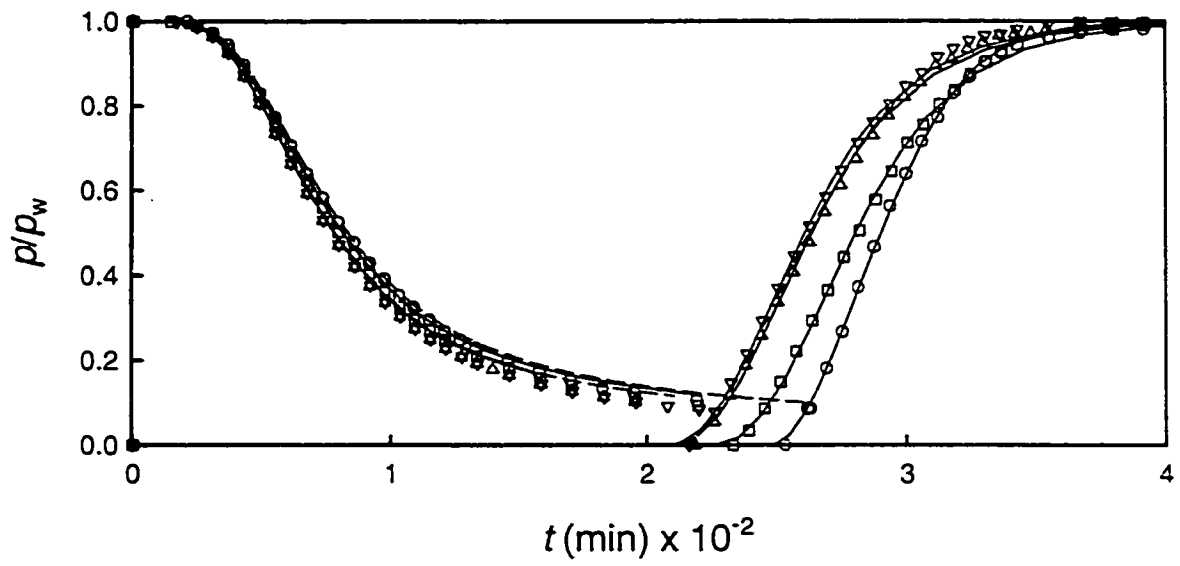


FIGURE 4-6 Experimental (symbols) and fitted adsorption (solid line) and desorption (dashed line) breakthrough curves for LHUFL (○), LHU1L (□), LHU2L (△), and LHU3L (▽).

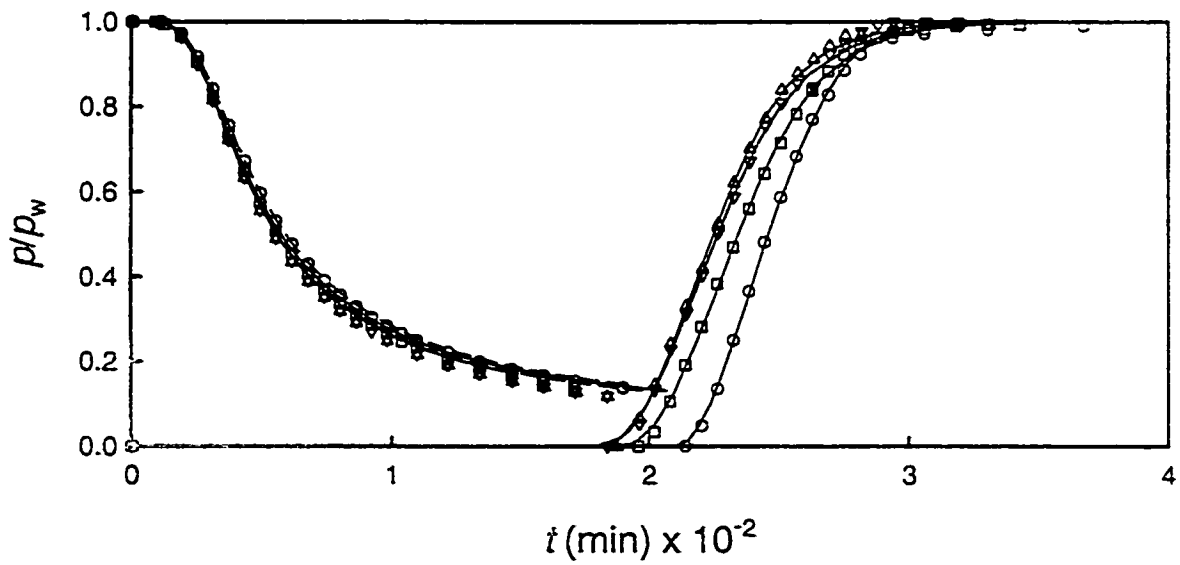


FIGURE 4-7 Experimental (symbols) and fitted adsorption (solid line) and desorption (dashed line) breakthrough curves for LHUFH (○), LHU1H (□), LHU2H (△), and LHU3H (▽).

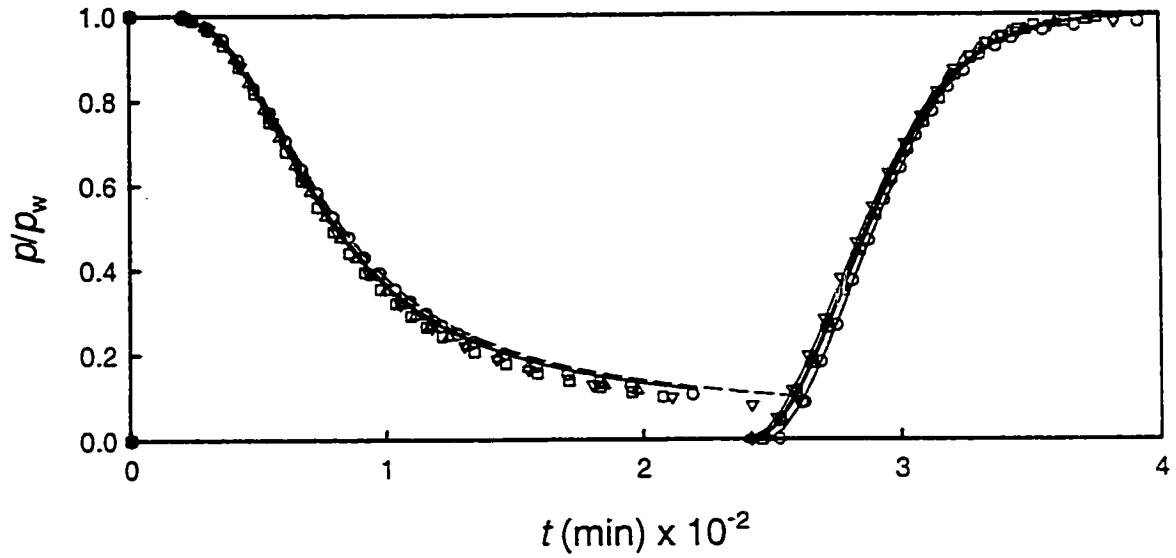


FIGURE 4-8 Experimental (symbols) and fitted adsorption (solid line) and desorption (dashed line) breakthrough curves for LLUFL (○), LLU1L (□), LLU2L (△), and LLU3L (▽).

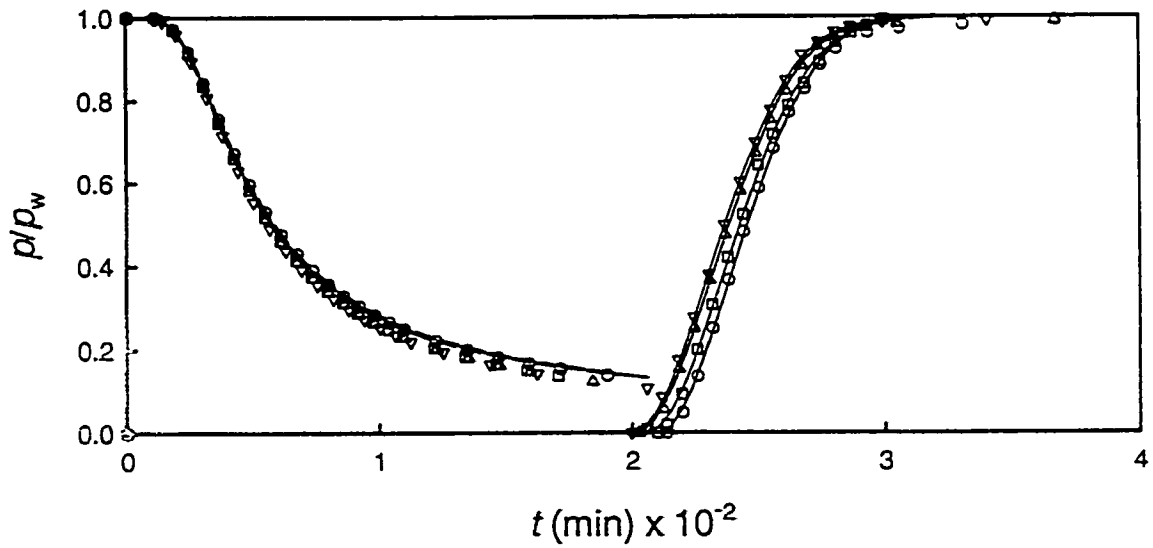


FIGURE 4-9 Experimental (symbols) and fitted adsorption (solid line) and desorption (dashed line) breakthrough curves for LLUFH (○), LLU1H (□), LLU2H (△), and LLU3H (▽).

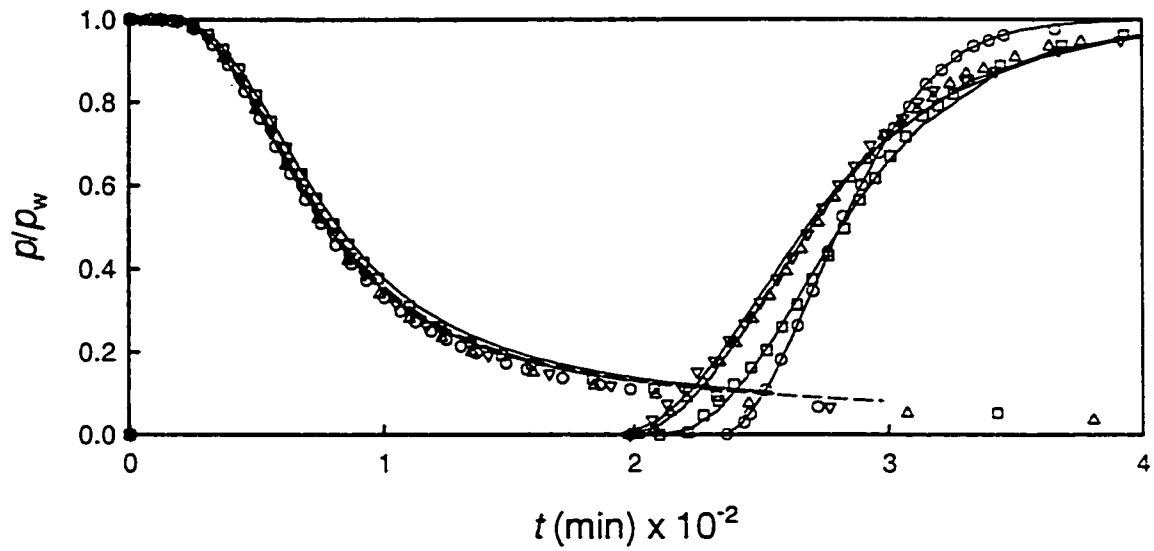


FIGURE 4-10 Experimental (symbols) and fitted adsorption (solid line) and desorption (dashed line) breakthrough curves for HHTFL (○), HHT1L (□), HHT2L (△), and HHT3L (▽).

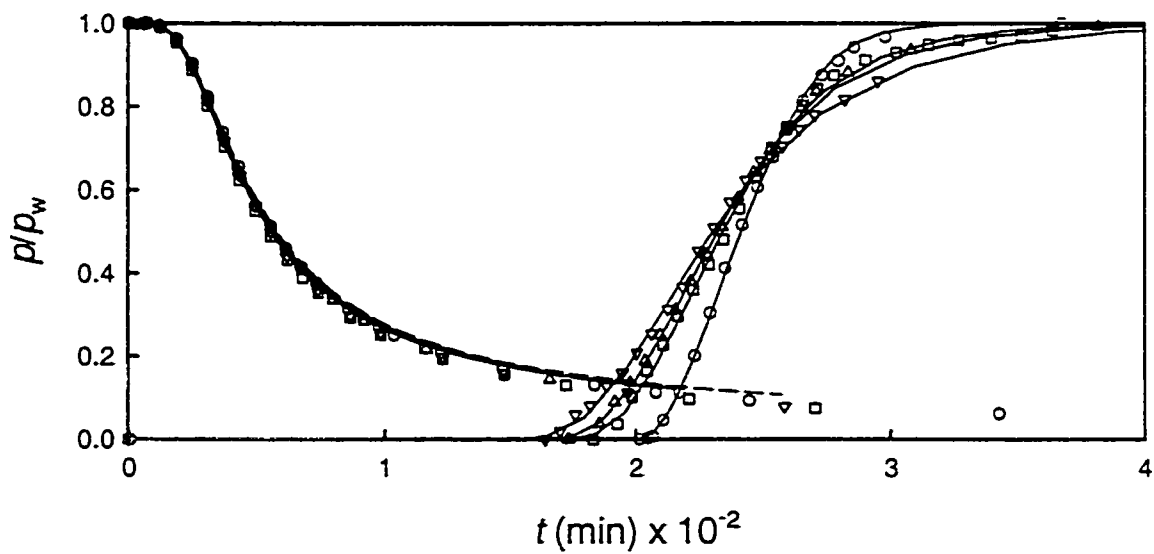


FIGURE 4-11 Experimental (symbols) and fitted adsorption (solid line) and desorption (dashed line) breakthrough curves for HHTFH (○), HHT1H (□), HHT2H (△), and HHT3H (▽).

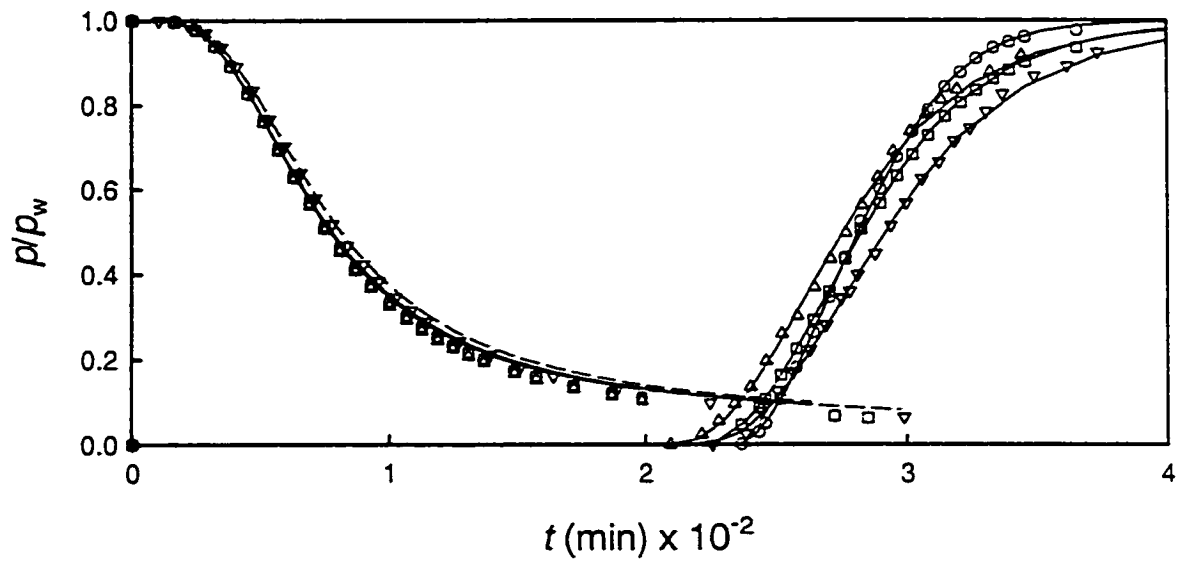


FIGURE 4-12 Experimental (symbols) and fitted adsorption (solid line) and desorption (dashed line) breakthrough curves for HLTFL (○), HLT1L (□), HLT2L (△), and HLT3L (▽).

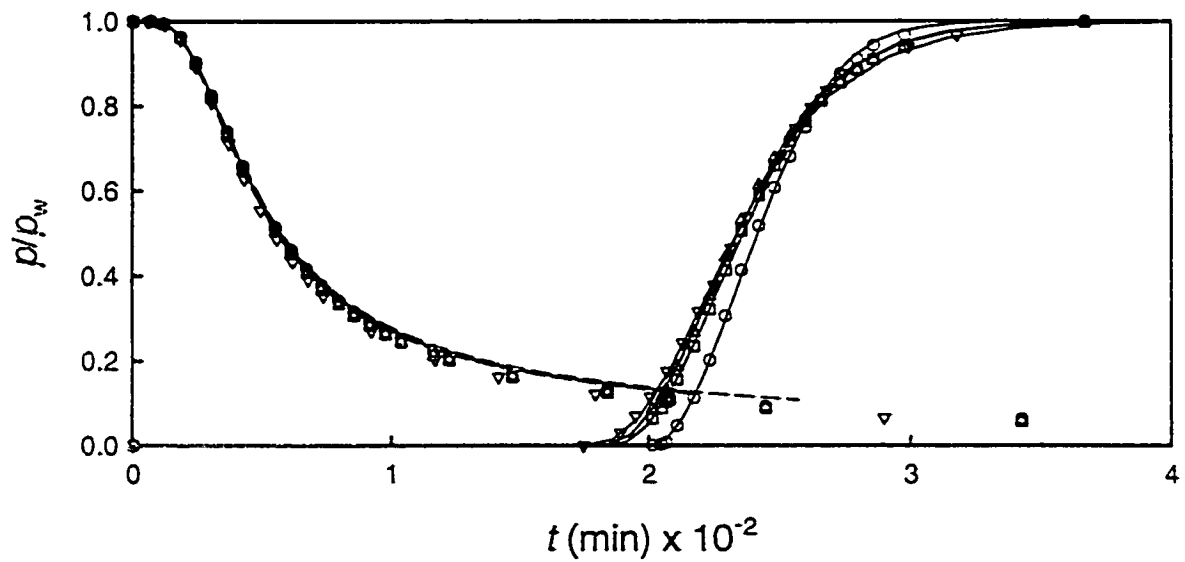


FIGURE 4-13 Experimental (symbols) and fitted adsorption (solid line) and desorption (dashed line) breakthrough curves for HLTfH (○), HLT1H (□), HLT2H (△), and HLT3H (▽).

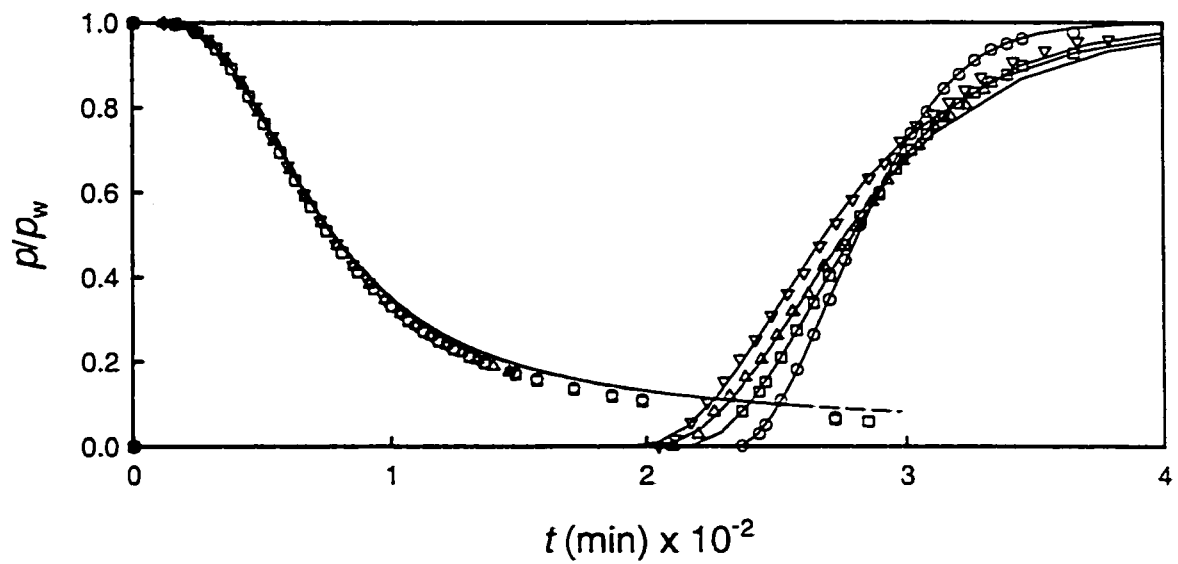


FIGURE 4-14 Experimental (symbols) and fitted adsorption (solid line) and desorption (dashed line) breakthrough curves for LHTFL (○), LHT1L (□), LHT2L (△), and LHT3L (▽).

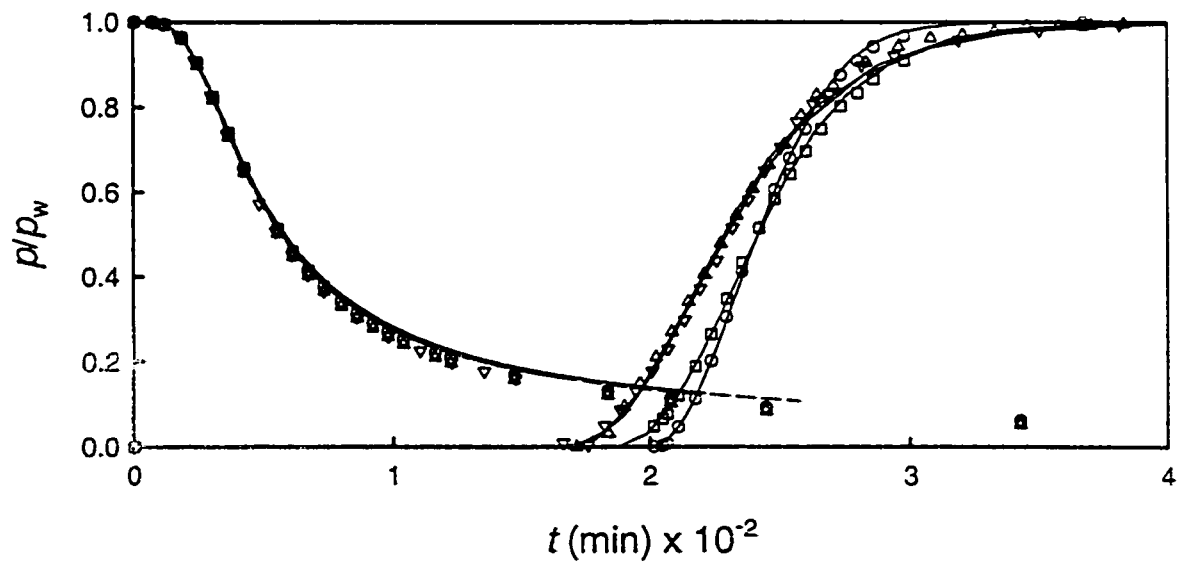


FIGURE 4-15 Experimental (symbols) and fitted adsorption (solid line) and desorption (dashed line) breakthrough curves for LHTFH (○), LHT1H (□), LHT2H (△), and LHT3H (▽).

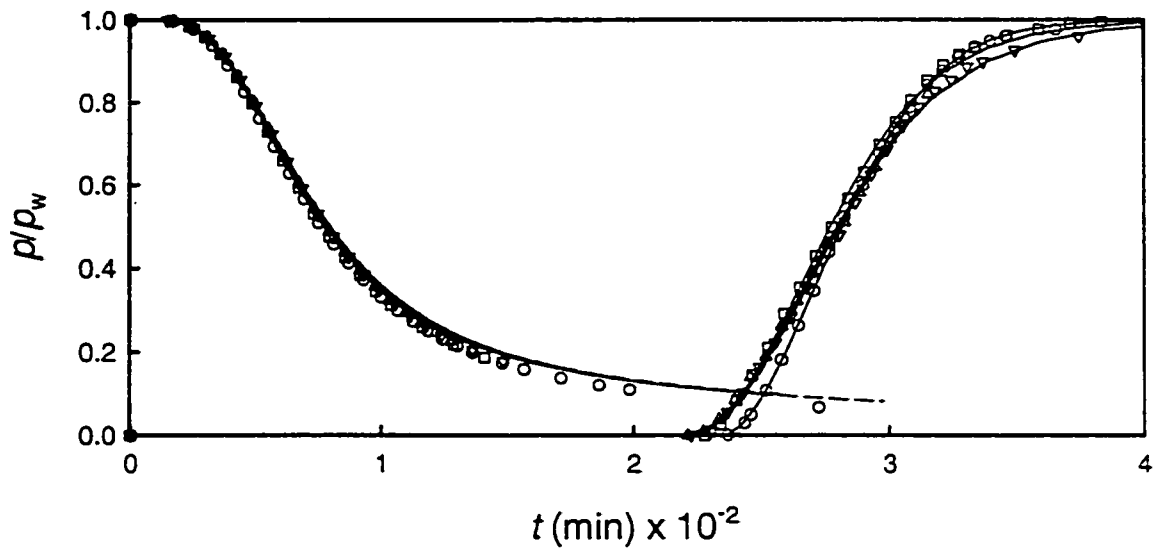


FIGURE 4-16 Experimental (symbols) and fitted adsorption (solid line) and desorption (dashed line) breakthrough curves for LLTFL (○), LLT1L (□), LLT2L (△), and LLT3L (▽).

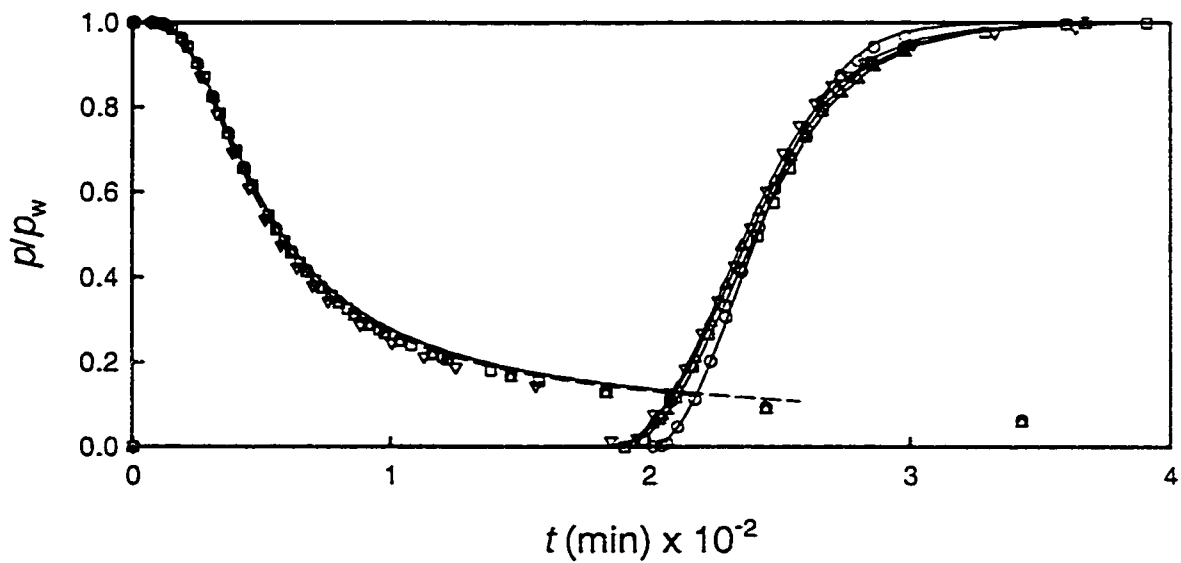


FIGURE 4-17 Experimental (symbols) and fitted adsorption (solid line) and desorption (dashed line) breakthrough curves for LLTFH (○), LLT1H (□), LLT2H (△), and LLT3H (▽).

The mass transfer coefficient for jump across the pore mouth openings, k_s , is proportional to $1/\tau_{pm}$, thus

$$\frac{k_s}{k_{s0}} = \frac{\tau_{pm0}}{\tau_{pm}} \quad (4-1)$$

where k_{s0} and τ_{pm0} are pore mouth mass transfer coefficients and pore mouth time constants, respectively, for fresh 4A zeolite samples. The ratio of pore mouth time constants is plotted as a function of deactivation time in Figures 4-18 through 4-21. It can be seen from Figure 4-18 obtained for Uetikon pellets at 175 °C that k_s/k_{s0} sharply decreases with deactivation time and finally approaches a constant equilibrium value. Further, it can be seen that the maximum decrease in pore mouth time constant is observed for the deactivation conditions corresponding to the most severe hydrothermal conditions (HH) and least decrease is observed for the least severe hydrothermal conditions (LL). It can be further seen that among the two intermediate hydrothermal conditions (HL and LH) one corresponding to the higher moisture concentration (LH) causes greater decrease in k_s/k_{s0} . These conclusions are consistent with the observations made earlier in this section. Similar trend is observed at 200 °C for Uetikon pellets and for TOSOH pellets at both 175 °C and 200 °C. A comparison of trends observed for Uetikon and TOSOH pellets reveals that TOSOH pellets deactivate faster than the Uetikon pellets.

4.5.1 Deactivation Mechanism

As mentioned earlier in this chapter the deactivation of 4A zeolite crystal is probably due to preferential dealumination of micropore pore openings. We therefore, propose that the deactivation takes place by preferential removal of framework aluminum from micropore pore openings in presence of adsorbed water. A possible mechanism of deactivation can be given as



where Z_a is the fresh or active zeolite, W is the water in adsorbed phase, Z_d is the deactivated zeolite, and Al is non-framework aluminum resulting from the dealumination of 4A zeolite. The rate expression for deactivation reaction 4-2 can be given as

$$\frac{dC_{za}}{dt} = -k_f q^n \left(C_{za} - \frac{C_{zd}}{K} \right) \quad (4-3)$$

where C 's are the concentrations of species given by the subscripts, q is the concentration of water in adsorbed phase, k_f is the forward reaction rate constant, and K is the concentration equilibrium constant. It is well known that for nonideal mixtures concentration equilibrium constant can be a function of concentration besides temperature. In a closed batch system, as used in the present study, the total zeolite content C_z is constant. Therefore, we have

$$C_z = C_{za} + C_{zd} \quad (4-4)$$

At equilibrium Eq. 4-3 becomes

$$C_{za}^e = \frac{C_{zd}^e}{K} \quad (4-5)$$

where C_{za}^e is the active zeolite concentration, and C_{zd}^e is the deactivated zeolite concentration at equilibrium. Substituting Eq. 4-5 in Eq. 4-4, we get

$$C_{zd} = C_{za}^e (1 + K) - C_{za} \quad (4-6)$$

Substituting Eq. 4-6 in Eq. 4-3, we get

$$\frac{dC_{za}}{dt} = -k_f \frac{1+K}{K} q^n (C_{za} - C_{za}^e) \quad (4-7)$$

If the pore mouths are completely blocked in deactivated portion of the zeolite then the overall pore mouth mass transfer coefficient k_s will be proportional to the concentration of active zeolite, C_{za} or

$$\frac{k_s}{k_{s0}} = \frac{C_{za}}{C_z} \quad (4-8)$$

where k_{s0} is the pore mouth mass transfer coefficient at time $t = 0$ or for the fresh zeolite sample. Thus, Eq. 4-7 can be written in terms of k_s as

$$\frac{dk_s}{dt} = -k_f \frac{1+K}{K} q^n (k_s - k_{sf}) \quad (4-9)$$

where k_{sf} is the final equilibrium value of pore mouth mass transfer coefficient k_s and can

be a function of deactivation temperature and moisture concentration. Forward reaction rate constant k_f is assumed to have the usual Arrhenius type dependence upon temperature, thus $k_f = k_f^* \exp(-E_f/RT)$. Using Eqs. 4-4, 4-5, and 4-8 k_{sf} can be written as

$$\frac{k_{sf}}{k_{so}} = \frac{1}{1+K} \quad (4-10)$$

Integrating Eq. 4-9 at constant temperature and water concentration, we get

$$\frac{k_s}{k_{so}} = \left(1 - \frac{k_{sf}}{k_{so}}\right) \exp\left(-\frac{t}{\tau_d}\right) + \frac{k_{sf}}{k_{so}} \quad (4-11)$$

where $\tau_d = 1/\left(k_f \frac{1+K}{K} q^n\right)$, is the deactivation time constant. The values of τ_d and k_{sf}/k_{so} are obtained by fitting the experimental data plotted in Figures 4-18 through 4-21. The values of deactivation time constant and limiting pore mouth mass transfer coefficient obtained by fitting the experimental data to model Eq. 4-11 are listed in Table 4-3. The corresponding deactivation curves are plotted and compared with the experimental data in Figures 4-18 through 4-21.

TABLE 4-3 Deactivation time constant and ratio of limiting pore mouth mass transfer coefficient obtained by fitting the experimental data to model equation.

Deactivation Conditions	Pellet Manufacturer	175 (°C)		200 (°C)	
		τ_d (hr)	k_{sf}/k_{so}	τ_d (hr)	k_{sf}/k_{so}
HH	Uetikon	54.02	0.33	2.59	0.35
LH	Uetikon	26.58	0.45	31.28	0.40
HL	Uetikon	82.60	0.61	76.02	0.60
LL	Uetikon	96.74	0.80	92.70	0.80
HH	TOSOH	40.92	0.25	50.61	0.23
LH	TOSOH	48.87	0.26	52.34	0.28
HL	TOSOH	49.38	0.33	55.15	0.38
LL	TOSOH	102.01	0.41	98.90	0.43

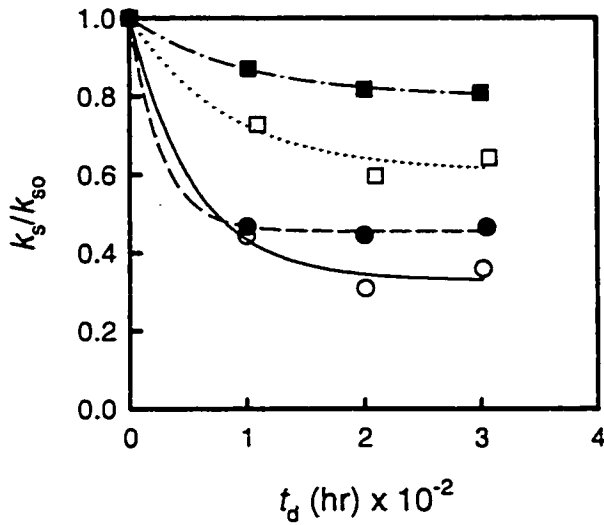


FIGURE 4-18 Ratio of pore mouth mass transfer coefficients for Uetikon pellets obtained at 175 °C and plotted as a function of deactivation time. Deactivation conditions: HH (○), LH (●), HL (□), LL (■). Smooth lines are fitted deactivation curves.

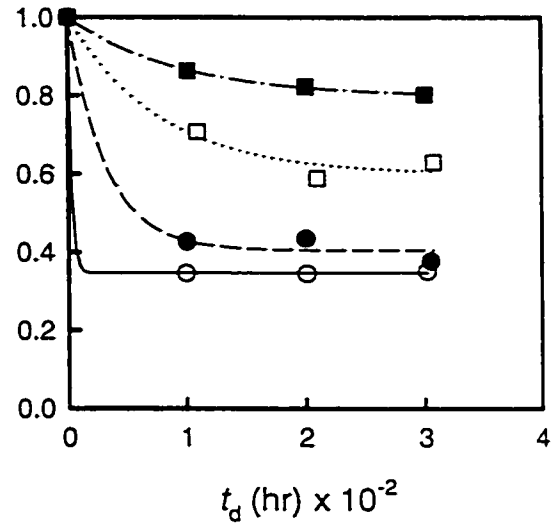


FIGURE 4-19 Ratio of pore mouth mass transfer coefficients for Uetikon pellets obtained at 200 °C and plotted as a function of deactivation time. Deactivation conditions: HH (○), LH (●), HL (□), LL (■). Smooth lines are fitted deactivation curves.

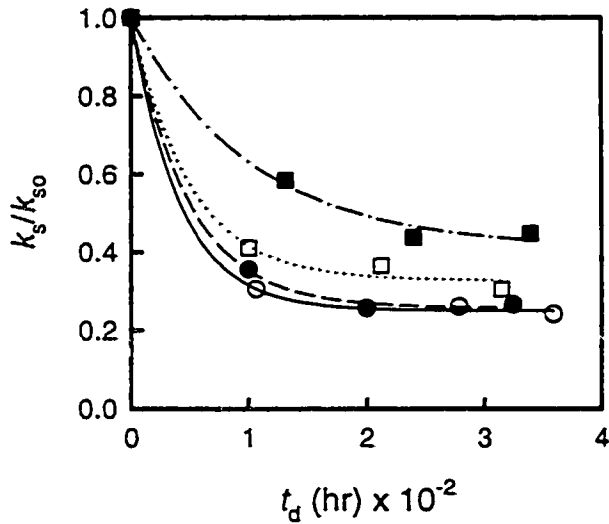


FIGURE 4-20 Ratio of pore mouth mass transfer coefficients for TOSOH pellets obtained at 175 °C and plotted as a function of deactivation time. Deactivation conditions: HH (○), LH (●), HL (□), LL (■). Smooth lines are fitted deactivation curves.

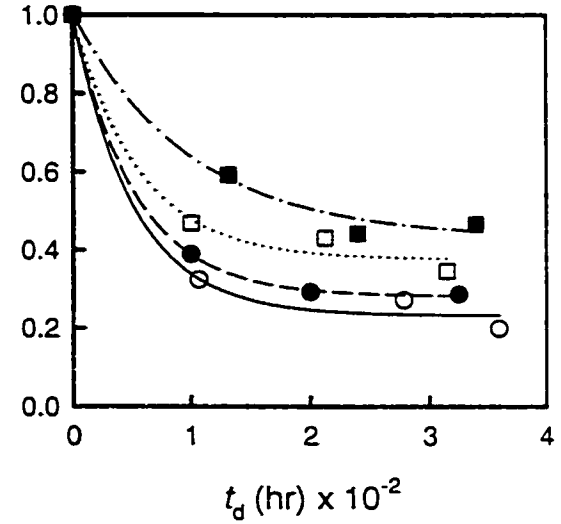


FIGURE 4-21 Ratio of pore mouth mass transfer coefficients for TOSOH pellets obtained at 200 °C and plotted as a function of deactivation time. Deactivation conditions: HH (○), LH (●), HL (□), LL (■). Smooth lines are fitted deactivation curves.

As mentioned earlier in this chapter, experimental breakthrough data has been generated using a batch system. It is well established in catalysis literature that continuous steaming of zeolite catalysts like X, and Y zeolites under severe hydrothermal conditions leads to dealumination of these zeolites and this phenomenon is widely used to control the acidity of zeolite catalysts⁹⁷. Therefore, if we assume that the deactivation of 4A zeolite is also due to dealumination then in a batch system fluid phase aluminum concentration will increase as a result of deactivation. Furthermore, if the deactivation or dealumination reaction is reversible then the equilibrium will be established probably before the value of k_s becomes very small. The fitted values of k_{sf}/k_{so} are much greater than zero and probably indicate that the dealumination reaction is reversible. In a continuous system where fluid phase aluminum concentration remains negligible the reaction will not be limited by equilibrium and driven to completion leading to complete pore blockage.

Jump across the micropore pore mouth is well known to be an activated process and can be appropriately expressed by Arrhenius equation as:

$$k_s = k_s^* \exp\left(-\frac{E_s}{RT}\right) \quad (4-12)$$

where k_s^* is a pre-exponential factor and E_s is the activation energy for jump across the pore mouths. Rewriting Eq. 4-12 in terms of pore mouth time constant τ_{pm} , we get

$$\tau_{pm} = \tau_{pm}^* \exp\left(\frac{E_s}{RT}\right) \quad (4-13)$$

where τ_{pm}^* corresponds to the pre-exponential factor. The activation energy E_s can be calculated by knowing the pore mouth time constant at two temperatures. The effect of deactivation on activation energies of Uetikon and TOSOH pellets is shown in Figures 4-22 and 4-23. It can be seen from Figure 4-22 that the uncertainties in calculating the activation energy are relatively large for deactivation conditions HH and LH and those for deactivation conditions HL and LL are much smaller. However, possibly the best trend is that the activation energy remains constant at all the four deactivation conditions and that the average $E_s/R = 3261$ K with standard deviation of 795 K for Uetikon pellets. The activation energies for TOSOH pellets are plotted in Figure 4-23 and show large uncertainties similar to the Uetikon pellets. However, the activation energies for TOSOH pellets are much smaller than those for Uetikon pellets. The best trend seems to be that the activation energy remains a constant at all the four deactivation conditions. The average $E_s/R = 1467$ K with standard deviation of 470 K for TOSOH pellets. The difference between the activation energy of jump for Uetikon and TOSOH pellets could be due to different binders used for palletization which could be kaolin clay or metal powder or a combination these two. This difference could also be due to the hydrothermal deactivation of Uetikon pellets during the pelletization process.

Kondis and Dranoff⁵⁸ studied the effect of steaming by comparing the kinetic behavior of pure 4A crystals with that of Linde 4A zeolite pellets. They used ethane as the sorbate and characterized the mass transfer by micropore diffusion control mechanism using an apparent ethane diffusivity. It is found that the activation energy for ethane diffusivity did not appear to change with deactivation and that the ratio of pre-

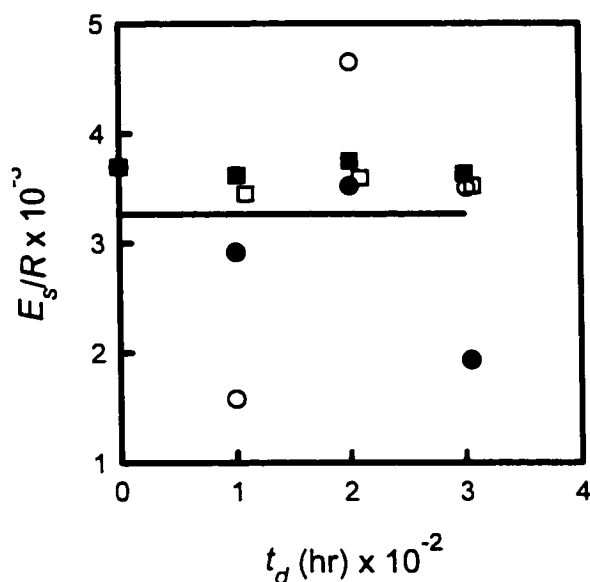


FIGURE 4-22 Effect of deactivation on activation energy for jump across pore mouths of Uetikon pellets. Deactivation conditions: HH (○), LH (●), HL (□), LL (■). Solid line is the average activation energy.

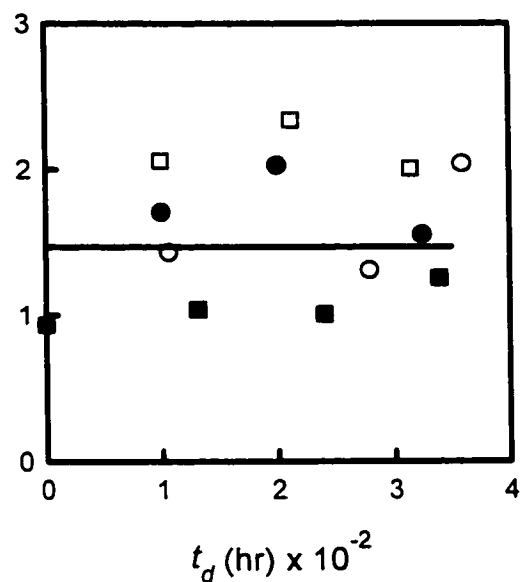


FIGURE 4-23 Effect of deactivation on activation energy for jump across pore mouths of TOSOH pellets. Deactivation conditions: HH (○), LH (●), HL (□), LL (■). Solid line is the average activation energy.

exponential factor of steamed zeolite to pure crystals is 0.091.

Since, the activation energy of jump across the pore mouth openings remain a constant at all the deactivation conditions investigated in this work, the pore mouth time constant, τ_{pm} , must increase as a result of increase in τ_{pm}^* or decrease in k_v^* . The pre-exponential factor k_v^* is associated with the entropy change associated with the jump. Thus, a decrease in k_v^* probably indicates an increase in entropy change which may be due to loss of crystallinity at the pore mouth leading to a higher degree of randomness.

Kärger et. al.⁷⁰ did not observe a higher activation energy for diffusion of various hydrocarbon molecules in fresh and deactivated zeolite samples. The authors measured pore mouth resistance for many hydrocarbons varying in chain length and molecular size.

The authors explained the increase in pore mouth resistance by a deposition of non-framework aluminum in the vicinity of the crystallite surface. It was observed that the large and small molecules were affected to a similar amount by the steaming. However, based on their hypothesis, the deposition of aluminum at the pore mouth will lead to pore mouth blockage which will affect the larger molecules more than the smaller ones. Thus, the results obtained by the authors are in contrast to the observations made in the present study. Thus, the present study indicates that the deactivation is due to dealumination of pore mouth leading to loss of crystallinity at the pore mouths rather than the blockage of pore mouth.

The overlap of desorption curves for fresh and deactivated samples probably indicate that during desorption molecules desorb directly from the adsorption sites and diffuse into the fluid phase. However, during adsorption the molecules are probably in a meta-adsorbed state at the pore mouth and then get adsorbed at the adsorption sites in the α and β cages. There are less sites available for meta-adsorption due to loss of crystallinity, resulting from deactivation, at the pore mouth leading to a slow rate of adsorption due to deactivation.

Expression for k_{sf} given by Eq. 4-10 can be written as

$$\frac{k_{sf}}{k_{so}} = \frac{1}{1 + K^* \exp\left(-\frac{\Delta H_D}{RT}\right) q^m} \quad (4-14)$$

where K^* , ΔH_D , and m are fitting parameters. q^m term in Eq. 4-14 accounts for the

dependence of concentration equilibrium constant K on concentration for non-ideal mixtures. Since, the activation energy for jump across the pore mouth does not change as a result of deactivation τ_d and k_{sf}/k_{so} must be independent of breakthrough curve measurement temperature. The values of k_{sf}/k_{so} are taken to be the average of those calculated at 175 °C and 200 °C for a given pair of deactivation temperature and moisture concentration. The values of fitting parameters both for Uetikon and TOSOH pellets obtained by least square fitting are listed in Table 4-4.

TABLE 4-4 Values of fitting parameters for limiting pore mouth mass transfer coefficient.

Parameter	Uetikon	TOSOH
K^*	7.544×10^4	126.5
m	1.19	0.53
$\Delta H_D/R$ (K)	5.54×10^3	1.81×10^3

TABLE 4-5 Values of fitting parameters for deactivation time.

Parameter	Uetikon	TOSOH
k_f^* (hr ⁻¹)	1.81×10^{10}	13.07
n	2.63	0.52
E_f/R (K)	1.39×10^4	3.74×10^3

The expression for τ_d is expanded in the form

$$\tau_d = \frac{1}{k_f^* \exp\left(-\frac{E_f}{RT}\right) \frac{1+K}{K} q^n} \quad (4-15)$$

where k_f^* , E_f and n are the fitting parameters. The values of these two parameters listed in Table 4-3 indicate that, except for Uetikon pellets at deactivation conditions HH, both τ_d and k_{sf}/k_{so} are same at 175 °C and 200 °C. The value of τ_d measured at 200 °C for Uetikon pellets at deactivation conditions HH seems more reasonable as it falls in general trend of increasing τ_d with increasing severity of deactivation conditions. In other cases

the values of τ_d are taken to be the average of those calculated at 175 °C and 200 °C for a given pair of deactivation temperature and moisture concentration. The values of fitting parameters both for Uetikon and TOSOH pellets obtained by least square fitting are listed in Table 4-5.

The large difference in k_f^* for Uetikon and TOSOH pellets is probably due to interaction between k_f^* and E_f/R well known in catalysis literature. Small errors involved in measurement of activation energy can lead to large differences in the value of pre-exponential factor. The calculated value of k_f for Uetikon pellets is much larger at all temperatures, indicating that the forward deactivation reaction is more rapid for Uetikon pellets than for TOSOH pellets. The forward deactivation reaction is more sensitive to moisture concentration for TOSOH pellets in comparison to Uetikon pellets. The overall effect of the temperature and moisture concentration is that at a given temperature and moisture concentration the forward deactivation reaction is much faster for Uetikon pellets in comparison to the TOSOH pellets. The overall rate of deactivation also depends upon the reverse reaction determined by the equilibrium constant K .

It can be shown from the values listed in Table 4-4 that for a given moisture concentration and at low temperatures, value of equilibrium constant K for Uetikon pellets is small in comparison to the TOSOH pellets. The equilibrium constant for Uetikon pellets increases more rapidly than that for TOSOH pellets. Therefore, at high temperatures K is larger for Uetikon pellets. The temperature at which K for both Uetikon and TOSOH pellets becomes equal, shifts to higher values with decreasing moisture

concentration. The equilibrium constant K for TOSOH pellets is more sensitive to moisture concentration than that for Uetikon pellets.

Thus, it can be seen that though the forward deactivation reaction is much faster for Uetikon pellets than the Tosoh pellets, low degree of deactivation is observed for Uetikon pellets due to a low equilibrium constant K at the investigated deactivation conditions. However, for a fixed moisture concentration an increase in temperature will lead to a rapid decrease in equilibrium constant for Uetikon pellets. Therefore, beyond a certain temperature both forward reaction rate and equilibrium constant will lead to a higher degree of deactivation for Uetikon pellets than the TOSOH pellets. At moisture concentration approaching the complete monolayer coverage this temperature could be as low as 675 K. In continuous systems where the reverse reaction is not present degree of deactivation is solely determined by the forward reaction. In such systems Uetikon pellets will deactivate much faster and to a higher degree than the TOSOH pellets.

4.6 Conclusions

Based on the discussion in the previous section we conclude the following

1. Both Uetikon and TOSOH pellets get deactivated at the experimental hydrothermal conditions used in this work.
2. A simple deactivation mechanism has been proposed and the deactivation rate equation derived based upon the proposed deactivation mechanism fits the experimental deactivation data.

3. Under the investigated deactivation conditions TOSOH pellets deactivate to a higher degree than Uetikon pellets. This behavior will be altered at higher deactivation temperature where Uetikon pellets will deactivate much faster and to a higher degree.
4. Activation energy of jump across the pore mouth does not change as a result of deactivation, however, the pre-exponential factor decreases as a result of deactivation indicating a possible loss of crystallinity at the pore mouth.
5. Water molecules adsorb into the 4A zeolite cages from a meta-adsorbed state at the zeolite crystal surface.

5

CONCLUSIONS AND RECOMMENDATIONS

5.1 Conclusions

The deactivation of 4A zeolite pellets in presence of severe hydrothermal conditions has been studied in the light of the experimental data generated in this study. The deactivation data is obtained for 4A zeolite pellets obtained from two manufacturers, viz. Uetikon and TOSOH. The deactivated 4A zeolite samples have been prepared at two temperature settings viz. 350 °C and 400 °C and two moisture concentration levels viz. 0.05 gm/gm and 0.16 gm/gm. The deactivated samples are analyzed by measuring the breakthrough curves of these samples at 175 °C and 200 °C and fitting the experimental breakthrough curves to theoretical ones to obtain the pore mouth time constant.

Water-4A zeolite adsorption isotherm is experimentally determined at 175 °C and 200 °C in the low partial pressure range of water vapor. The experimental data cannot be fitted to Langmuir isotherm equation, though it could satisfactorily be fitted to a dual site Freundlich-Langmuir isotherm. Fitting of experimental and theoretical breakthrough curves is carried out based upon the dual site Freundlich-Langmuir isotherm. The asymmetry between the adsorption and desorption breakthrough curves even at the low water loadings (less than 15 % of the saturation loading) investigated in this study are

satisfactorily accounted for using the dual site Freundlich-Langmuir isotherm.

A simple deactivation mechanism of 4A zeolite pellets has been proposed and the corresponding rate equation involving the deactivation temperature and moisture concentration is derived. The experimental deactivation data is fitted to the derived rate equation. Analysis of experimental data reveals that the deactivation is probably caused by loss of crystallinity due to preferential dealumination of the micropore pore openings. It is found that at all the deactivation conditions Uetikon pellets perform better than the TOSOH pellets.

The rate equation derived in this study can be of considerable practical value as it can be used to predict the degree of deactivation of 4A zeolite pellets in an existing adsorption column. It can also help in optimizing the run conditions in a way to maximize the adsorbent life.

5.2 Recommendations

In order to obtain further insight in the mechanism of hydrothermal deactivation of 4A zeolite pellets it is absolutely necessary to have a very accurate and direct measurement of pore mouth time constant and the aluminum concentration at the micropore pore openings. Some techniques like NMR and nuclear microscopy are available but due to practical constraints could not be used in the present study. However, it is desirable that the deactivated samples be analyzed using these techniques when they become operable.

Since, the present study is restricted to studying the deactivation in a batch system,

the degree of deactivation is limited by the equilibrium. These equilibrium limitations can be overcome by use of a continuous system in which high pressure steam flows through a bed packed with the 4A zeolite adsorbent. It is assumed in the present study that the adsorption isotherm does not change as a result of deactivation and the experimental data seems to be consistent with this assumption. However, in a continuous system where degree of deactivation could be very high this assumption may not be valid as the dealumination will not be limited to the pore openings alone. Therefore, further experimentation is required to produce very accurate deactivation data in order to model the deactivation phenomenon more realistically.

In industry, the dehydration of process streams is carried out in a cyclic manner therefore, it will be of interest to generate predictive breakthrough curves for such cyclic systems.

APPENDIX A

NUMERICAL CALCULATION OF BREAKTHROUGH CURVES

Model equations 3-11 through 3-18 developed in chapter three are solved numerically using the method of lines. The details of numerical method are presented in this appendix.

The fluid phase concentration transient terms, $\beta_b \partial c_b^* / \partial t^*$ in equation 3-11 and $\beta_p \partial c_m^* / \partial t^*$ in equation 3-12, are negligible in comparison to sorbed phase concentration transient terms. Let us assume that there are $(M + 1)$ finite difference points in axial direction of the bed, numbered sequentially from $z = 0$ to $z = L$, and $(N + 1)$ points in the radial direction of the pellet, numbered sequentially from $R = 0$ to $R = R_p$, at each of the finite difference points in the bed. The boundary condition 3-18 is automatically taken care of by letting the $(N + 1)^{\text{th}}$ point lying on the pellet surface be same as the corresponding point in the bed. Therefore, there are a total $(M + 1) \times (N + 1)$ finite difference points in the bed.

Let C be a $(M + 1) \times (N + 1)$ element vector whose elements are the fluid phase concentrations in the pellet at each of the finite difference points in the bed. Similarly, Q

is a $(M + 1) \times (N + 1)$ element vector whose elements are the sorbed phase concentrations in the pellet at each of the finite difference points in the bed. We use a second order accurate finite difference approximation for each of the spatial gradient terms in the model equations. Considering the boundary condition 3-15, the term on the left hand side is written as

$$\begin{aligned} -\frac{1}{Pe} \frac{\partial c_b^*}{\partial z^*} (z^* = 0, t^*) &\approx -\frac{1}{Pe} \frac{C_{z(N+1)} - C_{-(N+1)}}{2\Delta z} \\ &= -\frac{M}{2Pe} (C_{z(N+1)} - C_{-(N+1)}) \end{aligned} \quad (A-1)$$

where $\Delta z = 1/M$ is the increment in axial direction of the bed, $C_{z(N+1)}$ is the concentration at $z^* = \Delta z$, and $C_{-(N+1)}$ is concentration at a fictitious point at the inlet of the bed corresponding to $z^* = -\Delta z$. Equating right and left hand side of boundary condition 3-15, we get

$$C_{-(N+1)} = C_{z(N+1)} + \frac{2Pe}{M} (c_o^* - C_{(N+1)}) \quad (A-2)$$

where c_o^* is either 1 or 0 for adsorption or desorption, respectively. Similarly, boundary condition 3-16 is written as

$$C_{(M+2)(N+1)} = C_{M(N+1)} \quad (A-3)$$

where $C_{M(N+1)}$ is the concentration at $z^* = 1 - \Delta z$, and $C_{(M+2)(N+1)}$ is the concentration at a fictitious point $z^* = 1 + \Delta z$. Boundary condition 3-17 is written as

$$C_{(i-1)(N+1)+2} = C0_i \quad (\text{A-4})$$

where $C_{(i-1)(N+1)+2}$ is the concentration at $R^* = \Delta R^* = 1/N$ inside the pellet, $i = 1 \dots M + 1$, and $C0$ is a vector of concentrations at fictitious points $R^* = -\Delta R^*$. Eq. 3-13 can be written as

$$\frac{dQ}{dt} = \alpha_{mac-pm} (Qe - Q) \quad (\text{A-5})$$

where Qe is a vector of the sorbed phase concentration in equilibrium with the local fluid phase concentration C .

Eq. 3-12 can be simplified to give

$$\frac{\partial q^*}{\partial t^*} = \begin{cases} 3 \frac{\partial^2 c_m^*}{\partial R^{*2}} & R^* \rightarrow 0 \\ \frac{\partial^2 c_m^*}{\partial R^{*2}} + \frac{2}{R^*} \frac{\partial c_m^*}{\partial R^*} & R^* > 0 \end{cases} \quad (\text{A-6})$$

or in finite difference formulation

$$\frac{dQ_{(i-1)(N+1)+j}}{dt} = \begin{cases} 6N^2 (C_{(i-1)(N+1)+2} - C_{(i-1)(N+1)+1}) & j = 1 \\ N^2 \left(1 + \frac{1}{j-1} \right) C_{(i-1)(N+1)+j+1} - 2N^2 C_{(i-1)(N+1)+j} & j = 2 \dots N \\ + N^2 \left(1 - \frac{1}{j-1} \right) C_{(i-1)(N+1)+j-1} & \end{cases} \quad (\text{A-7})$$

where $i = 1 \dots M + 1$. Combining Eq. A-5 with Eq. A-7, we get

$$\alpha_{mac-pm} (Q_{e_{(i-1)\chi_{N+1}+j}} - Q_{(i-1)\chi_{N+1}+j}) = \begin{cases} 6N^2 (C_{(i-1)\chi_{N+1}+2} - C_{(i-1)\chi_{N+1}+1}) & j = 1 \\ N^2 \left(1 + \frac{1}{j-1}\right) C_{(i-1)\chi_{N+1}+j+1} \\ - 2N^2 C_{(i-1)\chi_{N+1}+j} & j = 2 \dots N \\ + N^2 \left(1 - \frac{1}{j-1}\right) C_{(i-1)\chi_{N+1}+j-1} \end{cases} \quad (A-8)$$

In order to write the finite difference formulation of Eq. 3-11 we need to write the finite difference formulation of $\partial \bar{q}^* / \partial r^*$ using trapezoidal rule as follows

$$\frac{1}{3} \left(\frac{\partial \bar{q}^*}{\partial r^*} \right)_i = \frac{1}{N^3} \left((1)^2 \frac{dQ_{(i-1)\chi_{N+1}+2}}{dt} \dots + (N-1)^2 \frac{dQ_{(i-1)\chi_{N+1}+N}}{dt} \right) + \frac{1}{2N} \frac{dQ_{i(N-1)}}{dt} \quad (A-9)$$

where $i = 1 \dots M + 1$. All the terms except the last one in Eq. A-9 can be calculated using Eq. A-7, and the last term can be calculated using Eq. A-5. Substituting the values and making some mathematical rearrangements, we get

$$\frac{1}{3} \left(\frac{\partial \bar{q}^*}{\partial r^*} \right)_i = (N-1) (C_{i(N+1)} - C_{i(N+1)-1}) + \frac{1}{2N} (Q_{e_{i(N-1)}} - Q_{i(N-1)}) \quad (A-10)$$

Substituting Eq. A-10 in Eq. 3-11, to get

$$\begin{aligned}
& C_{(i+1)\chi(N+1)} \left(\frac{M\alpha_{mac-con}}{2} - \frac{M^2\alpha_{mac-con}}{Pe} \right) + C_{i(N+1)} \left(\frac{2M^2\alpha_{mac-con}}{Pe} + 3(N-1) \right) \\
& + C_{(i-1)\chi(N+1)} \left(-\frac{M\alpha_{mac-con}}{2} - \frac{M^2\alpha_{mac-con}}{Pe} \right) \tag{A-11} \\
& - 3(N-1)C_{i(N+1)-1} + \frac{3}{2N}(Q_{e_{i(N+1)}} - Q_{i(N+1)}) = 0
\end{aligned}$$

where $i = 1 \dots M + 1$. For a known \mathbf{Q} , algebraic equations A-8 and A-11 can be solved to get vector \mathbf{C} . The time derivatives can then be calculated using Eq. A-5.

Equations A-8 and A-11 are solved in matlab using a highly optimized iterative subroutine originally written in C language and compiled into a matlab mex (.dll) file. The time integration is then carried out using matlab subroutine ode45.

APPENDIX B

LIST OF FILES ON CD

Following is the list of files on the cd.

TABLE B-1 List of all the files on the cd.

File name	File Type	Description
uetikondata.m	Matlab	Experimental isotherm data and program to fit it to dual site freundlich-langmuir isotherm
freulang.m	Matlab	Function file to be used with uetikondata.m
fdualbedpmmacd.m	Matlab	Function file for calculation of time derivatives of concentration in the adsorption column. Use ode45 to calculate the breakthrough curve.
newsetconc.dll	Matlab executable	A file to be used internally by fdualbedpmmacd.m. This file has a very efficient algorithm to calculate the time derivatives of concentrations in the adsorption column.
getconc.m	Matlab	This file is setup to be automatically used by ode45 while solving for bed concentration using fdualbedpmmacd.m
fdparamfit.m	Matlab	This file has code for fitting the theoretical adsorption breakthrough curve data to experimental one.
breakthrough curve data.xls	Excel	This file lists both experimental and fitted breakthrough curve data for all the samples.

LIST OF SYMBOLS

A		area under the breakthrough curve (min)
A_b		fraction of crystal surface that is blocked
c		sorbate concentration in fluid stream (gm/cc)
c_o		bulk phase concentration (chapter 1); sorbate concentration in fluid stream entering adsorption column (chapter 3) (gm/cc)
c_o^*	$c_o / \max(c_i, c_o)$	dimensionless sorbate concentration in fluid stream entering adsorption column
c_b		sorbate concentration in fluid phase (gm/cc)
c_b^*	$c_b / \max(c_i, c_o)$	dimensionless sorbate concentration in fluid phase
c_i		initial sorbate concentration in fluid phase (gm/cc)
c_i^*	$c_i / \max(c_i, c_o)$	dimensionless initial sorbate concentration in fluid phase
c_m		sorbate concentration in macropores (gm/cc)
c_m^*	$c_m / \max(c_i, c_o)$	dimensionless sorbate concentration in macropores
C_f		heat capacity of fluid phase (cal/gm °C)
C_z		total zeolite concentration (gm/cc)
$C_{za} (C_{za}^e)$		concentration of active zeolite phase (at equilibrium) (gm/cc)
$C_{zd} (C_{zd}^e)$		concentration of deactivated zeolite phase (at equilibrium) (gm/cc)
D		macropore diffusivity (chapter 1) (cm ² /sec)
D_o		intrinsic diffusivity (cm ² /sec)
D_c		micropore diffusivity (cm ² /sec)
D_K		Knudsen diffusivity (cm ² /sec)

D_L		axial dispersion coefficient (cm ² /sec)
D_m		molecular diffusivity (cm ² /sec)
D_p		effective macropore diffusivity (cm ² /sec)
E_f		activation energy for forward deactivation reaction (J/mol)
E_s		Activation energy for jump across pore mouth (J/mol)
f_i	$155/(155 + 775) = 0.1667$	volume fraction of adsorption sites in β cage
$-\Delta H$		heat of adsorption (J/mol)
$-\Delta H_d$		heat of deactivation (J/mol)
k		Boltzmann constant
k_1, k_2		Freundlich Langmuir isotherm fitting parameters (mbar ⁻¹)
$k_f (k_f^\circ)$		forward deactivation reaction rate constant (pre-exponential factor)
$k_s (k_{sf}, k_{so}, k_s^\circ)$		mass transfer coefficient for diffusion across pore opening (equilibrium value, for fresh zeolite, pre-exponential factor) ($\mu\text{m}/\text{sec}$)
K		Henry's constant (chapter 1); (cc/gm) Equilibrium constant (chapter 4) (dimensionless)
K°		Pre-exponential factor for K (chapter 4)
L		length of cylindrical crystal (chapter 2) (cm) adsorbent bed length (chapter 3) (cm)
m_i		total mass of water adsorbed on the adsorbent after i steps. (gm)
m_t		mass of adsorbate adsorbed at time t (gm)
m_∞		mass of adsorbate adsorbed at time $t = \infty$ (gm)
$M (M_i, M_w)$		molecular weight (of species i , of water)
n		order of deactivation reaction with respect to the adsorbed water

n_1, n_2		Freundlich Langmuir isotherm fitting parameters
n_p		number of blocked patches of equal area on the crystal surface
Pe	vL/D_L	axial Peclet number for column (dimensionless)
P		total pressure in atm
$p (p_w)$		partial pressure of water vapor (at the adsorption column inlet) (mbar)
$q (q_o, q_i, q_e, q_s)$		sorbate concentration (final, initial, at crystal surface or in equilibrium with the fluid phase, at monolayer (chapter 3) saturation) (gm/cc)
q_{sat}		sorbate concentration at monolayer saturation (chapter 2) (gm/cc)
q^*	$q/\max(q_i, q_o)$ $(q - q_i)/(q_s - q_i)$	dimensionless sorbate concentration (chapter 3) (chapter 2)
q_1^*, q_2^*		dimensionless sorbed phase concentration in exposed sector of the crystal, in blocked sector of the crystal
\bar{q}	$3/R_p^3 \int_0^{R_p} qR^2 dR$	sorbate concentration averaged over a single pellet (gm/cc)
r		radial coordinate in the crystal (chapter 2) (μm); mean pore radius (chapter 3) (\AA)
r_c		radius of zeolite crystal (μm)
r^*	r/r_c	dimensionless radial coordinate
r_s		radius of a solid cylindrical section ($r_s \leq r_c$) (cm)
R		radial coordinate in adsorbent pellet (cm); universal gas constant (J/mol K)
R^*	R/R_p	dimensionless radial coordinate in adsorbent pellet
R_p		radius of adsorbent pellet (cm)
$T (T_a)$		absolute temperature (ambient) in Kelvin
t		time (min)

t_{max}		time at which p/p_w approaches one (min)
t^*	t/τ_{mac} tD_o/r_c^2	dimensionless time (chapter 3) (chapter 2)
T_o		bulk temperature (K)
$u (u_1, u_2)$		transformation variable for concentration (in exposed sector of the crystal, in blocked sector of the crystal) (dimensionless)
\dot{V}		volumetric flow rate of carrier gas at STP (cc/min)
V_{cell}		volume of volumetric cell (cc)
V_s		volume of sample tube (cc)
v		interstitial fluid velocity (m/sec)
w_a		weight of adsorbent (gm)
z		axial coordinate (m)
z^*	z/L	dimensionless axial coordinate

GREEK LETTERS

$\alpha_{mac-con}$	τ_{mac}/τ_{con}	ratio of macropore to convection time constants (dimensionless)
α_{mac-pm}	τ_{mac}/τ_{pm}	ratio of macropore to pore mouth resistance time constants (dimensionless)
β_b	$\epsilon_b \max(c_i, c_o)/(1 - \epsilon_b) \max(q_o, q_i)$	ratio of bed capacity to adsorbent capacity (dimensionless)
β_p	$\epsilon_p \max(c_i, c_o)/(1 - \epsilon_p) \max(q_o, q_i)$	ratio of pellet capacity to adsorbent capacity (dimensionless)
ϵ	$\sqrt{\epsilon_1 \epsilon_2}$	Lennard Jones force constant
$\epsilon (\epsilon_b, \epsilon_p)$		porosity (bed, pellet) (dimensionless)
$\lambda (\lambda_i, \lambda_s)$	q/q_{sat}	relative saturation (initial, at the surface) (dimensionless)
θ		polar coordinate (Radian)
θ^*	$\theta/2\pi$	normalized polar coordinate (dimensionless)

θ_1^*	$2n_p/(1-A_b)\theta^*$	normalized polar coordinate in exposed sector of the crystal (varies between 0 and 1) (dimensionless)
θ_2^*	$(2n_p/A_b)\theta^* + 1 - 1/A_b$	normalized polar coordinate in blocked sector of the crystal (varies between 0 and 1) (dimensionless)
σ_{12}	$(\sigma_1 + \sigma_2)/2$	average Lennard Jones collision diameter for species 1 and 2 (Å)
σ_i		Lennard Jones collision diameter for species i (Å)
τ		pellet tortuosity (dimensionless)
τ_d		deactivation time constant (hr)
τ_{con}	$L/(\beta_b v)$	convection time constant (min)
τ_{mac}	$R_p^2/(\beta_p D_p)$	macropore time constant (min)
$\tau_{pm} (\tau_{pmo}, \tau_{pm}^*)$	$r_c/(3k_s)$	time constant for diffusion across micropore pore mouth (fresh zeolite. pre-exponential factor) (min)
Ω		a function of ε/kT

REFERENCES

1. D. M. Ruthven, *Principles of Adsorption and Adsorption Processes*, John Wiley & Sons, New York, 1984.
2. D. W. Breck, *Zeolite Molecular Sieves*, Wiley, New York, 1974.
3. C. R. Antonson, and J. S. Dranoff, Nonlinear Equilibrium and Particle Shape Effects in Intraparticle Diffusion Controlled Adsorption. *AIChE Symp. Ser.*, **65**(96), 20-26 (1969).
4. W. S. Kyte, Nonlinear Adsorption in Fixed Beds. Freundlich Isotherm. *Chem. Eng. Sci.*, **28**(10), 1853-1856 (1973).
5. D. R. Garg, and D. M. Ruthven, Theoretical Prediction of Breakthrough Curves for Molecular Sieve Adsorption Columns - I Asymptotic Solutions. *Chem. Eng. Sci.*, **28**, 791-798 (1973).
6. D. R. Garg, and D. M. Ruthven, Theoretical Prediction of Breakthrough Curves for Molecular Sieve Adsorption Columns - II General Isotherm Solution for Micropore Diffusion Control. *Chem. Eng. Sci.*, **28**, 799-805 (1973).
7. D. R. Garg, and D. M. Ruthven, The Performance of Molecular Sieve Adsorption Columns: Systems with Micropore Diffusion Control. *Chem. Eng. Sci.*, **29**, 571-581 (1974).
8. J. W. Carter, and H. Husain, Carbon Dioxide Adsorption in Fixed beds of Molecular Sieves. *Trans. I. Chem. Eng.*, **50**(1), 69-75 (1972).
9. D. R. Garg, and D. M. Ruthven, The Performance of Molecular Sieve Adsorption Columns: Systems with Macropore Diffusion Control. *Chem. Eng. Sci.*, **29**, 1961-1967 (1974).
10. D. DeVault, The Theory of Chromatography. *J. Am. Chem. Soc.*, **65**, 532-540 (1943).
11. A. Anzelius, Über Erwärmung Vermittels Durchströmender Medien. *Z. Angew. Math. Mech.*, **6**, 291-294 (1926).
12. J. E. Walter, Multiple Adsorption from Solutions. *J. Chem. Phys.*, **13**(6), 229-234 (1945).
13. J. E. Walter, Rate Dependent Chromatographic Adsorption. *J. Chem. Phys.*, **13**(8), 332-336 (1945).
14. C. C. Furnas, Heat Transfer from a Gas stream to a Bed of Broken Solids. *Trans. Am.*

- Inst. Chem. Eng.*, **24**, 142-193 (1930).
15. W. Nusselt, *Tech. Mech. Thermodynam.*, **1**, 417 (1930).
 16. A. Klinkenberg, Heat Transfer in Cross-Flow Heat Exchangers and Packed Beds : Evaluation of Equations for Penetration of Heat or Solutes. *Ind. Eng. Chem.*, **46**(11), 2285-2289 (1954).
 17. L. Lapidus, and N. R. Amundson, Mathematics of Adsorption in Beds. VI. The Effect of Longitudinal Diffusion in Ion Exchange and Chromatographic Columns. *J. Phys. Chem.*, **56**, 984-988 (1952).
 18. O. Levenspiel, and K. B. Bischoff, *Advances in Chemical Engineering*, Vol. 4, Academic Press, New York, 1963.
 19. J. B. Rosen, Kinetics of a Fixed Bed System for Solid Diffusion into Spherical Particles. *J. Chem. Phys.*, **20**(3), 387-394 (1952).
 20. J. B. Rosen, General Numerical Solution for Solid Diffusion in Fixed Beds. *Ind. Eng. Chem.*, **46**(8), 1590-1594 (1954).
 21. A. Rasmuson, and I. Neretnieks, Exact Solution of a Model for Diffusion in Particles and Longitudinal Dispersion in Packed Beds. *AIChE J.*, **26**, 686-690 (1980).
 22. K. Kawazoe, and Y. Takeuchi, Mass Transfer in Adsorption on Bidisperse Porous Materials. Macro- and Micropore series Diffusion Model. *J. Chem. Eng. Japan*, **7**(6), 431-437 (1974).
 23. A. Rasmuson, Time Domain Solution of a Model for Transport Processes in Bidisperse Structured Catalysts. *Chem. Eng. Sci.*, **37**(5), 787-788 (1982).
 24. G. Bohart, and E. Adams, Some Aspects of the Behavior of Charcoal with respect to Chlorine. *J. Am. Chem. Soc.*, **42**, 523-544 (1920).
 25. R. S. Cooper, Slow Particle Diffusion in Ion Exchange Columns. *Ind. Eng. Chem. Fund.*, **4**(3), 308-313 (1965).
 26. R. S. Cooper, and D. A. Liberman, Fixed-bed Adsorption Kinetics with Pore Diffusion Control. *Ind. Eng. Chem. Fund.*, **9**(4), 620-623 (1970).
 27. T. W. Weber, and R. K. Chakravorty, Pore and Solid Diffusion Models for Fixed-bed Adsorbers. *AIChE J.*, **20**(2), 228-238 (1974).
 28. F. W. Leavitt, Nonisothermal-Isothermal Adsorption in large Fixed Beds. *Chem. Eng. Prog.*, **58**(8), 54-59 (1962).
 29. N. R. Amundson, R. Aris, and R. Swanson, On Simple Exchange Waves in Fixed

- Beds. *Proc. Roy. Soc. London*, **286A**, 129-139 (1965).
30. C. Y. Pan, and D. Basmadjian, An Analysis of Adiabatic Sorption of Single Solutes in Fixed Beds: Pure Thermal Wave Formation and its Practical Implications. *Chem. Eng. Sci.*, **25**, 1653-1654 (1970).
 31. C. Y. Pan, and D. Basmadjian, An Analysis of Adiabatic Sorption of Single Solutes in Fixed Beds: Equilibrium Theory. *Chem. Eng. Sci.*, **26**, 45-57 (1971).
 32. J. W. Carter, Numerical Method for Prediction of Adiabatic Adsorption in Fixed Beds. *Trans. I. Chem. Eng.*, **44**(6), T253-T259 (1966).
 33. J. W. Carter, and D. J. Barrett, Comparative study for Fixed Bed Adsorption of Water Vapor by Activated Alumina, Silica Gel, and Molecular Sieve Adsorbents. *Trans. I. Chem. Eng.*, **51**(2), 75-81 (1973).
 34. J. W. Carter, Isothermal and Adiabatic Adsorption in Fixed Beds. *Trans. I. Chem. Eng.*, **46**(7), T213-T222 (1968).
 35. O. A. Meyer, and T. W. Weber, Nonisothermal Adsorption in Fixed Beds. *AIChE J.*, **13**(3), 457-465 (1967).
 36. R. G. Lee, and T. W. Weber, Interpretation of Methane Adsorption on Activated Carbon by Nonisothermal and Isothermal Calculations. *Can. J. Chem. Eng.*, **47**, 60-65 (Feb 1969).
 37. P. Ozil, and L. Bonnetain, Theoretical Prediction of Temperature Profiles in an Adsorbent Fixed-bed. *Chem. Eng. Sci.*, **33**, 1233-1237 (1978).
 38. H. Yoshida, and D. M. Ruthven, Dynamic Behavior of an Adiabatic Adsorption Column. I. Analytic solution for Irreversible Adsorption. *Chem. Eng. Sci.*, **38**(6), 877-884 (1983).
 39. D. O. Cooney, Numerical Investigation of Adiabatic Fixed-Bed Adsorption. *Ind. Eng. Chem. Process Des. Develop.*, **13**(4), 368-373 (1974).
 40. K. Ikeda, Performance of the Nonisothermal Fixed Bed Adsorption Column with Nonlinear Isotherms. *Chem. Eng. Sci.*, **34**(7), 941-949 (1979).
 41. L. Marcussen, Comparison of Experimental and Predicted Breakthrough Curves for Adiabatic Adsorption in Fixed Bed. *Chem. Eng. Sci.*, **37**(2), 299-309 (1982).
 42. N. S. Raghavan, T. W. Duncan, and D. M. Ruthven, Numerical Simulation of an Adiabatic Reactor Packed with a Deactivating Catalyst. *Chem. Eng. J.*, **26**(3), 223-229 (1983).

43. D. M. Ruthven, and S. Brandani, Measurement of Diffusion in Porous Solids by ZLC Methods in *Recent Advances in Gas Separation by Microporous Ceramic Membranes*, N. K. Kanellopoulos ed., Elsevier, Amsterdam, (2000).
44. S. Brandani, Analytical Solution for ZLC Desorption Curves with Bi-Porous Adsorbent Particle. *Chem. Eng. Sci.*, **51**(12), 3283-3288 (1996).
45. S. Brandani, Z. Zu, and D. M. Ruthven, Transport Diffusion and Self Diffusion of Benzene in NaX and CaX Zeolite Crystals Studied by ZLC Tracer Methods. *Microporous Materials*, **7**, 323-331 (1996).
46. A. C. S. Jose, and A. E. Rodrigues, Analysis of ZLC Technique for Diffusivity Measurement in Bidisperse Porous Adsorbent Pellets. *Gas Sep. Purif.*, **10**(4), 207-224 (1996).
47. S. Brandani, Effects of Nonlinear Equilibrium on Zero Length Column Experiments. *Chem. Eng. Sci.*, **53**(15), 2719-2798 (Dec 1998).
48. S. Brandani, C. Cavalcante, A. Guimaraes, D. M. Ruthven, Heat Effects in ZLC Experiments Analytical. *Adsorption*, **4**, 275-285 (1998).
49. W. L. Duncan, and K. P. Moller, A Zero Length Criterion for ZLC Chromatography. *Chem. Eng. Sci.*, **55**, 5415-5420 (2000).
50. D. M. Ruthven, and P. Stapleton, Measurement of Liquid Phase Counter Diffusion in Zeolite Crystals by the ZLC Method. *Chem. Eng. Sci.*, **48**, 89-98 (1993).
51. M. Eic, M. Goddard, and D. M. Ruthven, Diffusion of Benzene in NaX and Natural Faujasite. *Zeolites*, **8**, 327-331 (1988).
52. M. Eic, and D. M. Ruthven, A New Experimental Technique for Measurement of Intracrystalline Diffusivities. *Zeolites*, **8**, 40 (1989).
53. A. C. S. Jose, and A. E. Rodrigues, Sorption and Diffusion of n-Pentane in Pellets of 5A Zeolite. *Ind. Eng. Chem. Res.*, **36**, 493-500 (1997).
54. L. C. Celio Jr, S. Brandani, and D. M. Ruthven, Evaluation of the Main Diffusion Path in Zeolites from ZLC Desorption Curves. *Zeolites*, **18**, 282-285 (1997).
55. A. G. Carlos, G. Carlos, A. E. Rodrigues, Adsorption of Propane and Propylene in Pellets and Crystals of 5A Zeolites. *Ind. Eng. Chem. Res.*, **41**, 85-92 (2002).
56. S. Brandani, M. Jama, and D. M. Ruthven, Diffusion and Self-Diffusion of Benzene and p-Xylene in Silicalite. *Microporous Materials*, **35**, 283-300 (2000).
57. S. Brandani, M. Jama, and D. M. Ruthven, Counter-Diffusion of p-Xylene/o-Xylene

- in Silicalite Studied by Zero Length Column Technique. *Ind. Eng. Chem. Res.*, **39**, 821-828 (2000).
58. E. F. Kondis, and J. S. Dranoff, Kinetics of Isothermal Sorption of Ethane on 4A Molecular Sieve Pellets. *Ind. Eng. Chem. Process Des. Develop.*, **10**(1), 108-114 (1971).
59. J. Kärger, and D. M. Ruthven, *Diffusion in Zeolites*, John Wiley & Sons, New York, 1991.
60. M. Bülow, P. Struve, and L. V. C. Rees, Investigation of the Gaseous Phase Diffusion and Liquid Phase Self-diffusion of n-decane on NaCa-A Zeolites. *Zeolites*, **5**(2), 113-117 (1985).
61. M. Bülow, P. Struve, and S. Pikus, Influence of Hydrothermal Pretreatment on Zeolitic Diffusivity detected by Comparative Sorption Kinetics and Small-Angle X-ray Scattering Investigations. *Zeolites*, **2**(4), 267-270 (1982).
62. E. F. Kondis, and J. S. Dranoff, Kinetics of Ethane Sorption on 4A Molecular Sieve Crystal Powder and Pellets. *Adv. Chem.*, **102**(Molecular Sieve Zeolites-II), 171-183 (1971).
63. D. M. Ruthven, and R. I. Derrah, Diffusion of Monoatomic and Diatomic Gases in 4A and 5A Zeolites. *J. Chem. Soc. Faraday Trans. I*, **71**(10), 2031-2044 (1975).
64. D. M. Ruthven, R. I. Derrah, and K. F. Loughlin, Diffusion of Light Hydrocarbons in 5A Zeolite. *Can. J. Chem.*, **51**, 3514-3519 (1973).
65. I. H. Doetsch, D. M. Ruthven, and K. F. Loughlin, Sorption and Diffusion of n-Heptane in 5A Zeolite. *Can. J. Chem.*, **52**, 2717-2724 (1974).
66. J. Kärger, A Study of Fast Tracer Desorption in Molecular Sieve Crystals. *AIChE J.*, **28**(3), 417-423 (1982).
67. J. Kärger, W. Heink, H. Pfeifer, M. Rauscher, and J. Hoffman, NMR Evidence of the Existence of Surface Barriers on Zeolite Crystallites. *Zeolites*, **2**(4), 275-278 (1982).
68. J. Kärger, H. Pfeifer, M. Rauscher, and M. Bülow, Comparative NMR and Uptake Studies of Molecular Transport of Ethane in 5A Zeolites after different Sample Pretreatment. *Z. Phys. Chem. (Leipzig)*, **262**(3), 567-576 (1981).
69. J. Kärger, H. Pfeifer, R. Richter, H. Furtig, W. Roscher, and R. Seidel, NMR study of Mass Transfer in Granulated Molecular Sieves. *AIChE J.*, **34**, 1185-1189 (1988).
70. J. Kärger, H Pfeifer, F. Stallmach, M. Bülow, P. Struve, R. Entner, H. Spindler, and R. Seidel, Influence of Molecular Shape on Probing Mass Transfer Resistances on

Zeolites. *AIChE J.*, **36**(10), 1500-1504 (Oct 1990).

71. J. Kärger, H. Pfeifer, R. Seidel, B. Staudte, and T. Gross, Investigation of Surface Barriers on NaCaA Type Zeolites by Combined Application of the NMR Tracer Desorption Method and X-Ray Photoelectron Spectroscopy. *Zeolites*, **7**(4), 282-284 (1987).
72. R. Seidel, and B. Staudte, Deterioration of CaNaA-type Zeolites by Hydrothermal treatment and Under the Conditions of Hydrocarbon Separation Processes. *Zeolites*, **13**, 348-356 (Jun 1993).
73. V. Bourdin, A. Germanus, P. Grenier, and J. Kärger, Application of the Thermal Frequency Response Method and of Pulsed Field Gradient NMR to Study Water Diffusion in Zeolite NaX. *Adsorption*, **2**, 205-216 (1996).
74. J. Kärger, and H. Pfeifer, NMR Self-diffusion Studies in Zeolite Science and Technology. *Zeolites*, **7**(2), 90-107 (1987).
75. H. Paoli, A. Méthivier, H. Jobic, C. Krause, H. Pfeifer, F. Stallmach, and J. Kärger, Comparative QENS and PFG NMR Diffusion Studies of Water in Zeolite NaCaA. *Microporous and Mesoporous Materials*, **55**(2), 147-158 (Sep 2002).
76. B. G. Anderson, F. J. M. M. de Gauw, N. J. Noordhoek, L. J. van IJendoorn, R. A. van Santen, and M. J. A. de Voigt, Mass Transfer of Alkanes in Zeolite Packed-Bed Reactors Studied with Positron Emission Profiling (PEP). 1. Experiments. *Ind. Eng. Chem. Res.*, **37**(3), 815-824 (1998).
77. N. J. Noordhoek, L. J. van IJendoorn, B. G. Anderson, F. J. M. M. de Gauw, R. A. van Santen, and M. J. A. de Voigt, Mass Transfer of Alkanes in Zeolite Packed-Bed Reactors Studied with Positron Emission Profiling. 2. Modeling. *Ind. Eng. Chem. Res.*, **37**(3), 825-833 (1998).
78. M. Misk, M. Guisnet, and S. Jullian, Formation of Coke from Propene over 5A Adsorbents - Influence of the Binder on Coke Composition, Location and Removal. *Microporous and Mesoporous Materials*, **40**, 197-204 (2000).
79. H. W. Habgood, The Kinetics of Molecular Sieve Action. Sorption of Nitrogen-Methane by Linde Molecular Sieve 4A. *Can. J. Chem.*, **36**, 1384-1397 (1958).
80. V. J. Villadsen, and M. L. Michelsen, *Solution of differential equations by polynomial approximation*, Prentice-Hall, Englewood Cliffs, New Jersey, 1978.
81. M. Abramowitz, and I. A. Stegun, *US NBS Applied Mathematics Series*, Vol. 55, , 1970.
82. A. K. Jain, and A. K. Gupta, Adsorptive Drying of Isopropyl Alcohol on 4A

- Molecular Sieves: Equilibrium and Kinetic Studies. *Sep. Sci. Tech.*, **29**(11), 1461-1472 (1994).
83. J. O. Hirschfelder, C. F. Curtiss, and R. B. Bird, *Molecular Theory of Gases and Liquids*, Wiley, New York, 1954.
84. E. H. Kennard, *Kinetic Theory of Gases*, McGraw-Hill, New York, 1938.
85. G. Langer, A. Roethe, K-P. Roethe, and D. Gelbin, *Int. J. Heat and Mass Trans.*, **21**, 751 (1978).
86. R. Aris, and N. R. Amundson, *AIChE J.*, **3**, 280 (1957).
87. D. L. Smith, Optimize solid bed adsorption systems. *Hydrocarbon Processing*, **75**(5), 129-132 (May 1996).
88. H. Paoli, A. Méthivier, H. Jobic, C. Krause, H. Pfeifer, F. Stallmach, and J. Kärger, Comparative QENS and PFG NMR Diffusion Studies of Water in Zeolite NaCaA. *Microporous and Mesoporous Materials*, **55**(2), 147-158 (Sep 2002).
89. M. Ahmed, M. A. Al-Ohali, M. Garwan, S. Narasimhan, and K. Al-Soufi, Analysis of Water Trees in Underground High Voltage Cables using the KFUPM Micro-PIXE Facility. *IEEE Transactions on Dielectric and Electrical Insulation*, **6**, 95-99 (1999).
90. M. Ahmed, M. Faiz, M. A. Al-Ohali, and O. Fageeha, Depth Profiling of a Thin YBCO Single Crystal using Micro-PIXE Technique. *Nuclear Instruments and Methods*, **B132**, 507-511 (1997).
91. N. I. Khandaker, M. Ahmed, M. Hariri, M. Al-Ohali, M. A. Garwan, and K. Khan, Microanalytical Investigations of Gold-bearing Rocks from An-Najadi Region in Saudi Arabia. *Nuclear Instruments and Methods*, **B130**, 654-659 (1997).
92. M. Ahmed, J. Nickel, A. Hallak, R. Abdel-Aal, A. Coban, H. Al-Juwair, and M. Aldaous, The KFUPM Scanning Nuclear Microprobe Facility. *Nuclear Instruments and Methods*, **B82**, 584-588 (1993).
93. M. Ahmed, A. Rahman, J. Nickel, and M. A. Garwan, Measurement of Nickel Distribution over Supported Nickel Oxide Catalysts. *Nuclear Instruments and Methods*, **B103**, 233-236 (1995).
94. M. Atiqullah, M. Ahmed, M. N. Akhtar, S. Ahmed, H. Hamid, J. H. Khan. and K. Alam, Micro-PIXE Study of Selected Heterogenized Zirconocene Catalysts. *Journal of Radioanalytical and Nuclear Chemistry*, **240**(3), 893-896 (1999).
95. A. Rahman, M. Mohamed, M. Ahmed, and A. M. Aitani, Characterization of Chromia/Alumina Catalysts by X-ray Photoelectron Spectroscopy (XPS), Proton

Induced X-ray Emission (PIXE) and Thermogravimetric (TG) Analysis. *Applied Catalysis*, **121**, 203-216 (1995).

96. A. Rahman, and M. Ahmed, Dehydrogenation of Propane over Chromia/Alumina: A Comparative Characterization Study of Fresh and Spent Catalysts. *Studies in Surface Science and Catalysis*, **100**, 419-426 (1996).

97. C. N. Satterfield, *Heterogeneous Catalysis in Industrial Practice*, Vol. 2, McGraw-Hill International Editions, 1993.

VITA

Name	Ifadat Ali Khan
Date & Place of Birth	03-Mar-1972, Nainital (India)
Nationality	Indian
Religion	Islam
Marital Status	Married
Educational qualifications	B. Tech. in Chemical Engineering from Indian Institute of Technology, Delhi, India (1990-94). M. E. in Chemical Engineering from Indian Institute of Science, Bangalore, India (1994-96). Ph. D. in Chemical Engineering from King Fahd University of Petroleum & Minerals, Dhahran. Saudi Arabia (1997-todate).